The Dissertation Committee for Matthew Wayne Lluis Certifies that this is the approved version of the following dissertation:

Crystal Structures of Dimethylarginine Dimethylaminohydrolase-1 (DDAH-1) from *Homo Sapiens* Bound to the Inhibitors N^5-(1-iminopentyl)-L-ornithine and Ebselen
and
Functional Studies of the Translin●Trax Complex from *Mus Musculus*

Committee:

Jon D. Robertus, Supervisor

Kenneth A. Johnson

George Georgiou

Scott W. Stevens

Walter L. Fast

Crystal Structures of Dimethylarginine Dimethylaminohydrolase-1 (DDAH-1) from *Homo Sapiens* Bound to the Inhibitors N^5-(1-iminopentyl)-L-ornithine and Ebselen
and
Functional Studies of the Translin●Trax Complex from *Mus Musculus*

by

Matthew Wayne Lluis, B.S.

Dissertation

Presented to the Faculty of the Graduate School of

The University of Texas at Austin

in Partial Fulfillment

of the Requirements

for the Degree of

Doctor of Philosophy

The University of Texas at Austin

December 2009

Dedication

To Robert, Sylvia F., Robert J., Audrey E., and Jeffrey B.

Acknowledgements

Thanks to the Robertus Lab: Dr. Robertus for the great degrees of freedom and patience in the workplace (it's too bad those conversations on cosmic inflation, dark matter, and the spacetime continuum were not more frequent), Dr. Arthur F. Monzingo for the great degrees of help with data collection, processing, and especially crystal looping, Huda S. ("The Sudaner") Suliman (not Suleman), Warren X. Hoe (The man of Troy), and Joshua C. Russel for their help, encouragement, friendship, and participation in conversations on the USC two-deep, religion, middle eastern culture, drop D tuning, retro air jordans, and life as we know (and will know) it, along with other assorted and not so related topics, Yan Bai and Shuangluo Xia, and the most recent additions: Devinder Ubhi, Karl Jasheway, and Beth Watt. I would also like to thank graduate students from other labs for their help: Clint Leysath, Venu Bhaskara, Simrit Dhaliwal, and Michael Dennis, and my friends outside of UT Campus and Austin: Anelis ('Lis) M. Vazquez (Mi otro hermana…por vida) for her genuine friendship, Jesell Lopez for genuinely being herself (don't ever change, girl…we'll meet again), Christopher Caravello and Sal Scardino for being authentic, my other B.R.O.E.S., Michael Hunter (I don't think we are ever going to top 9th grade geometry class), BP for Repo Man, Joe from Lord's Boxing Gym, my S.D.M.F.s worldwide, Casey Sanders for the early days (I'll never forget '93, brother), Luis Pinzon and Ling Feng Schuchert for the latter days

(I’m never going to forget ’02 and ’03 either), and Johnny Chang for all the days in between (’95 and ’96, those were some good days, guy…those were definitely some good days) and those days still to come…no matter how far off they may be, Sneauxball for bringing me down to the Irish Channel (“How you doin’, sweetheart!”), Alex at LBTR in NOLA (“Can I get another water?”), Justyna and Diana in Barcelona, the girl on that train in Lisbon for sending me a message (Eu ainda não entendi isto…mas eu sei que significou algo), Hannah “Barbera” from BD’s, Leroy Kevin Webb (my all-time favorite teammate), Clive Francis, Paul Werner (best class ever), Mr. Saltzgaver, Mrs. Stewart, Coach Billy Turner, Jason C. for that day at the greenbelt (like GW crossing the Delaware), Joe and Marco for that one at Hamilton Pool, Jeff Baker for turning the corner (’99 was a weird time, kid), Pablo R., A.J. Hoffman, Kevin Willis and Charles Oakley, Anthony Poindexter, Arthur Dabney (especially), the two best blood relatives I have: Victor Hugo Lluis and Cousin Kris (with a “K”) for their wisdom, limitless knowledge, and intricate personalities, my extended family: Aunt Aida, Aunt Sonja, Aunt Tita, Cousin Et, and Ellen Leahy amongst many others, Mike Reeder and Marc Heard from HPG for their encouragement, Dr. Edward Turos and Dr. Jesse Binford, and the Kings of Metal for being born for a reason and living legendary (cause they’re going to be ageless, timeless, ageless and timeless…for fkn’ ever). Finally, I would like to send my deepest thanks to the two people I owe the most to, my Mother and Father. From them I inherited a good last name and the reputation that goes with it. I hope that when this life is over…it can be said that I made my own contribution to that.

Crystal Structures of Dimethylarginine Dimethylaminohydrolase-1 (DDAH-1) from *Homo Sapiens* Bound to the Inhibitors N^5-(1-iminopentyl)-L-ornithine and Ebselen
and
Functional Studies of the Translin●Trax Complex from *Mus Musculus*

Publication No._____________

Matthew Wayne Lluis, Ph.D.
The University of Texas at Austin, 2009

Supervisor: Jon D. Robertus

Nitric oxide (NO) is reactive, radical gas that is involved in a myriad of cellular signaling pathways including the regulation of blood flow and immunodefense. NO is produced from the oxidation of L-arginine to L-citrulline by nitric oxide synthase (NOS). The activity of NOS and by default, the production of NO, is regulated by the arginine derivatives N^{ω},N^{ω}-dimethyl-L-arginine (ADMA) and N^{ω}-monomethyl-L-arginine (NMMA) which arise from the proteolytic degradation of post translationally methylated proteins. The cellular concentrations of ADMA and NMMA are regulated by the enzyme dimethylarginine dimethylaminohydrolase (DDAH), which catabolizes these compounds to L-citrulline and dimethylamine or methyl amine, respectively. Because over and under production of NO has been implicated in several pathophysiological states, compounds that control NO production by inhibiting NOS or DDAH may prove useful as treatments.

In this study, the crystal structures of human DDAH-1 with the inhibitors N^5-(1-iminopentyl)-L-ornithine (L-IPnO) and ebselen were solved to 2.9 and 2.0 Å resolution, respectively. L-IPnO was observed to inhibit DDAH-1 in essentially the same manner as another amidino-containing inhibitor: docking to the enzyme via hydrogen bond and ion pair interactions and forming a covalent adduct with the active site cysteine. Ebselen was also observed to covalently attach to the active site cysteine, however, the docking mechanism was absent of hydrogen bond and ion pair interactions. The work presented here contributes to the design of compounds that may effectively regulate the production of NO for therapeutic purposes.

Translin is a highly conserved mammalian RNA and DNA binding protein known to be involved in DNA recombination and repair, RNA trafficking in neurons, and post-transcriptional regulation of gene expression in male germ cells. Although crystal structures of the mouse and human orthologs of translin have been solved, they do not provide details on the structure-function relationship of the protein. Studies have identified a partner protein for translin, translin associated factor x (trax), which is believed to have a crucial role in assisting translin with its cellular functions. It is believed that trax regulates translin's affinity for certain RNA and DNA sequences. In this work the binding affinities of translin and the translin●trax complex were investigated. It was observed that translin preferentially binds to G-rich RNA sequences, most likely recognizing a secondary structure intrinsic to these sequences, whereas translin●trax preferentially binds G-rich DNA sequences. The results from these experiments provide insight into the cellular functions of translin and trax and their respective roles in mRNA trafficking.

Table of Contents

List of Tables

List of Figures

Chapter 1: Introduction

Nitric Oxide

Nitric oxide (NO) is a reactive, radical gas used by vertebrates for cellular processes including neurotransmission, immunodefense, and regulating blood vessel dilation [1, 2]. NO is a highly labile compound that can diffuse freely across the cellular membrane, making it an ideal transient signaling molecule [1, 3]. NO is synthesized by the oxidation of arginine's guanidino nitrogen by the enzyme nitric oxide synthase (NOS), which uses NADPH and O_2 to produce NO and L-citrulline in a 1:1 ratio (Figure1.1) [1].

In mammals, nitric oxide is produced by three nitric oxide synthase isozymes: neuronal NOS (nNOS), inducible NOS (iNOS), and endothelial NOS (eNOS) [4, 5]. nNOS produces NO in the nervous tissue for cellular signaling between neurons [4, 5]. Phagocytes are equipped with iNOS for the purpose of NO production as an immune response [4, 5]. eNOS produces NO in the vascular system in order to control blood flow [4, 5]. Considering the fact that it is a signaling molecule for cellular processes as disparate as mediation of blood flow and immunodefense, it comes as no surprise that the biochemistry of NO is versatile and complex [1, 2, 5]. NO exists as a free radical and nitrogen can exist in several oxidation states including +1 in the nitroxyl ion NO^-, +2 in the nitric oxide free radical $NO^\cdot$ and the nitrosium ion NO^+, +3 in the nitrite ion NO_2^-, and +5 in the nitrate ion NO_3^- [5]. These chemical properties grant NO the ability to react with metals, thiols, and oxides, allowing it to activate or inhibit proteins directly or indirectly, and also modify nucleic acids, lipids, and sugars [5].

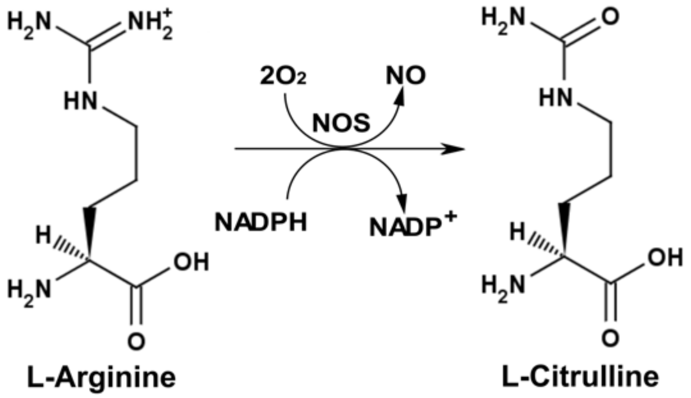

Figure 1.1: Synthesis of NO. Nitric oxide synthase catalyzes the oxidation of L-arginine to produce L-citrulline and NO [3].

As an example, guanylyl cyclase is a physiological target that is activated indirectly by NO. NO binding to the Fe^{+2} of the heme group of the enzyme induces a conformational change that activates the enzyme leading to an increase in the cellular concentration of cyclic GMP [5]. Alternatively, NO has also been shown to react with the Fe-S cluster of aconitase, leading to the inhibition of that enzyme [5]. Because NO reactivity is so versatile and is at least in some way tied to the redox state of the cell, NO levels can affect many signaling pathways (Figure 1.2) and as a result can have both protective and detrimental effects [5].

Interestingly, under- and overproduction of NO has been linked to various diseases and disorders, with overproduction causing conditions such as septic shock and rheumatoid arthritis, and low NO levels being associated with hypertension and renal failure among other pathogenic states [3, 5, 6]. Additionally, previous studies have shown varying levels of NO production to produce contradictory results, such as inhibiting cancer growth at high cellular levels but *facilitating* cancer growth at levels 10-100-fold lower, both inducing *and* preventing apoptosis, and add to *or* defend against damage after stroke [7-14]. Due to it's dichotomous biochemistry, NO has been figuratively described in the literature as a "double-edged sword". Because of its direct or indirect involvement in the diseases and disorders previously mentioned and the complexity of controlling its production, regulation of NO production is a very active research field.

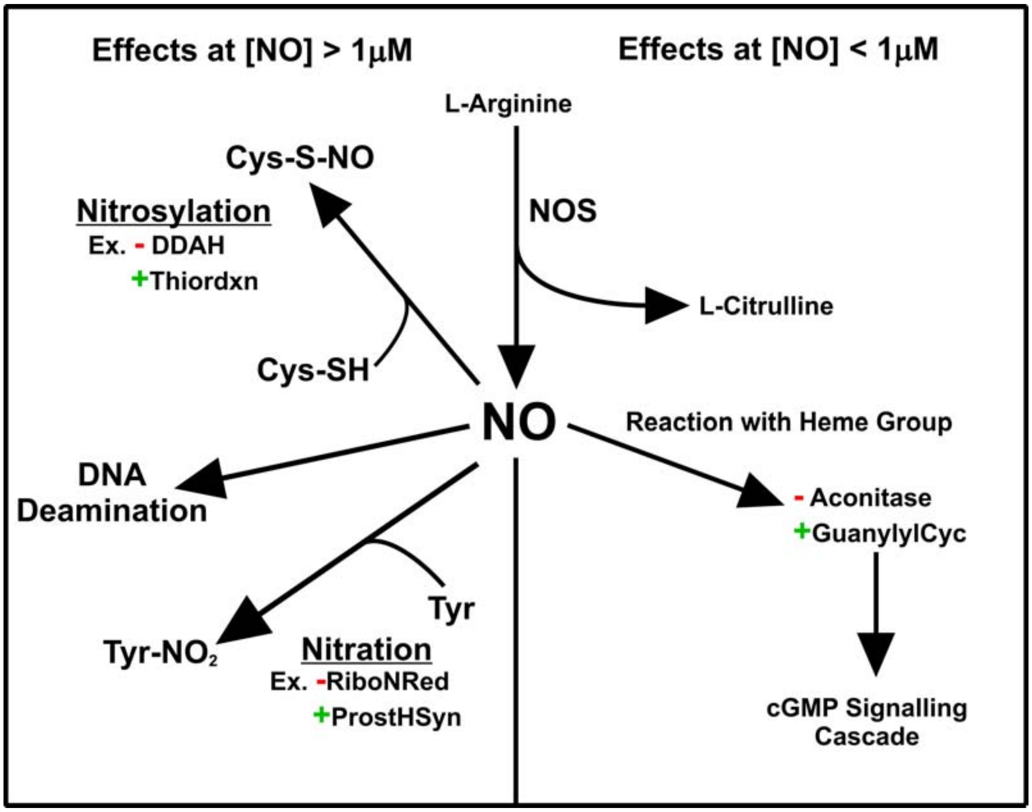

Figure 1.2: The effects of NO at high and low cellular concentration. At high concentrations (greater than 1µM), NO can nitrosylate the γS of active site cysteines of enzymes like thioredoxin (Thiordxn) and dimethylarginine dimethylaminohydrolase (DDAH), which can result in both activation (thioredoxin) and inhibition (DDAH) of these enzymes. High concentrations of NO also leads to the deamination of cytosine to thymidine, and nitration of tyrosine residues in enzymes like ribonucleotide reductase (RiboNRed, resulting in inhibition) and prostaglandin H synthase (ProstHSyn, resulting in activation). At low concentrations (less than 1µM) NO can react with Fe containing heme groups of enzymes that can result in inhibition (aconitase) or activation (guanylyl cyclase (GuanylylCyc). This figure was adapted from [1].

Nitric Oxide Synthases

To reiterate, in mammals, three isozymes of Nitric Oxide Synthase exist: nNOS, iNOS, and eNOS. These isoforms share 51-57% homology between them and all three exist as homodimeric proteins with each subunit 125 – 160 kDa in size and consisting of two domains [4]. The ~500 residue N-terminal oxygenase domain contains the dimer interface and catalyzes the 5 electron oxidation of L-arginine to produce NO and L-citrulline [4]. The ~600 residue C-terminal reductase domain provides the electrons for the reaction [4]. Since NO is so widely used for inducing physiological responses in wide ranging tissues, regulation of NOS activity is complex. For the eNOS and nNOS isoforms the primary mode of regulation is activation by Ca^{+2}-calmodulin binding to a region encompassing the first 30 amino acids of the protein's C-terminal domain [4]. Alternatively, iNOS is not activated by Ca^{+2}-calmodulin and it is primarily activated by transcriptional induction [4]. Additionally, it is also known that the activities of the three mammalian NOS isoforms are regulated in some way by phosphorylation and other protein-protein interactions [4].

However, a key part of NOS regulation, and by default regulation of the production of NO involves endogenous methyl arginine derivatives. Specifically, asymmetric N^{ω},N^{ω}-dimethyl-L-arginine (ADMA) and N^{ω}-monomethyl-L-arginine (NMMA) have proven to be endogenous inhibitors of all three isoforms of NOSs in mammals [15] (Figure 1.3). Methylarginines originate from the proteolytic degradation of proteins whose arginine residues were post-translationally methylated by protein arginine methyl transferases (PRMTs) [15]. Recent research has flagged ADMA as a biomarker of cardiovascular disease. High ADMA levels have been linked to serious cardiovascular conditions including hypercholesterolemia, atherosclerosis, high-blood pressure, and chronic heart failure [16, 17]. Additionally, elevated ADMA levels have also been linked to chronic renal failure and diabetes mellitus [18]. In a healthy individual, about 10% of the ADMA pool is eliminated by excretion via the kidneys [19].

The balance of the ADMA pool is eliminated via a catabolic pathway in which the enzyme dimethylarginine dimethylaminohydrolase (DDAH) degrades ADMA into L-citrulline and dimethyl amine [15, 20, 21] (Figure 1.4 and Figure 1.5). DDAH also regulates the pool of NMMA in the plasma, breaking this methyl arginine down into L-citrulline and methyl amine [21] (Figures 1.4 and 1.5).

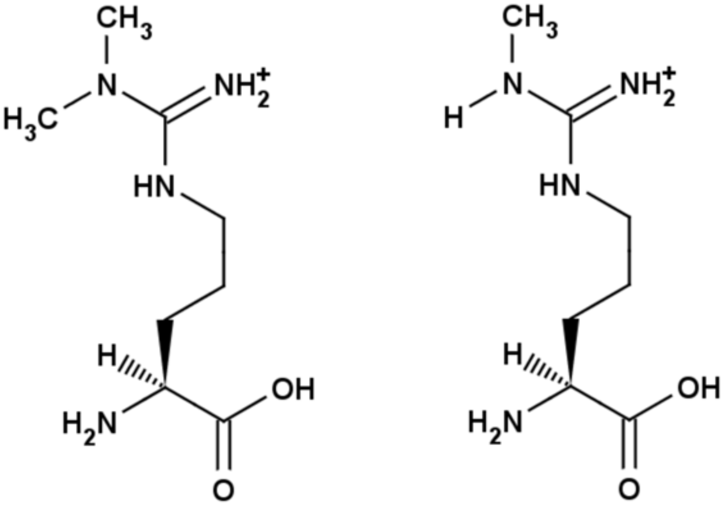

ADMA **NMMA**

Figure 1.3: The structures of asymmetric N^{ω},N^{ω}-dimethyl-L-arginine (ADMA) and N^{ω}-monomethyl-L-arginine (NMMA). These methyl arginine derivates are endogenous inhibitors of all three mammalian isoforms of NOS and originate from the proteolytic degradation of proteins which contain methylated arginine residues.

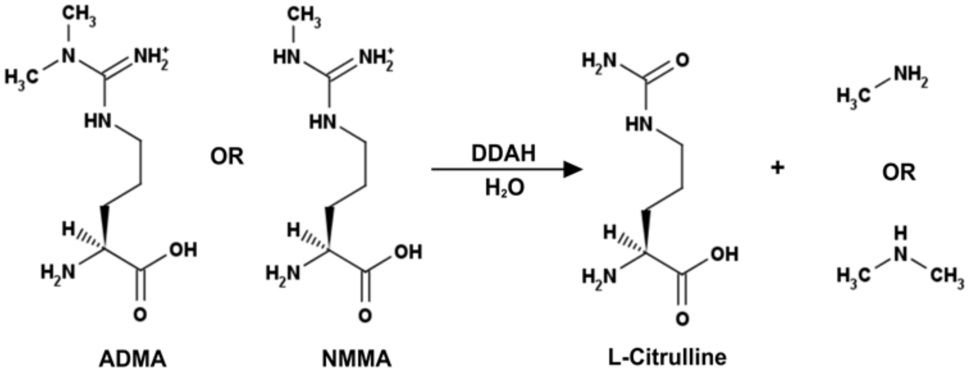

Figure 1.4: Hydrolysis of ADMA and NMMA. DDAH converts ADMA or NMMA to L-citrulline and dimethyl amine or methyl amine, respectively. DDAH catalyzes this conversion without any known cofactors. In a healthy individual, only 10% of the ADMA pool is eliminated by renal excretion, the remainder is removed by the DDAH pathway [19].

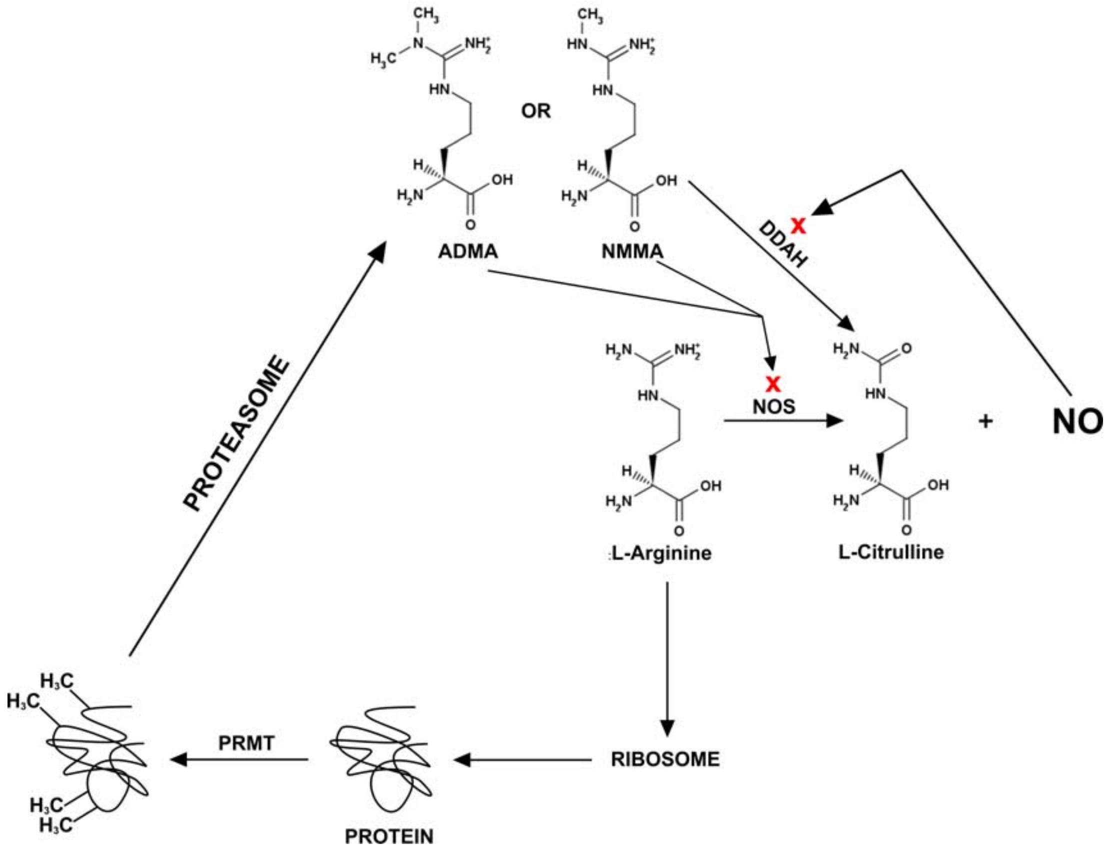

Figure 1.5: The roles of DDAH, ADMA, and NMMA in the regulation of NO production. Nitric oxide synthase (NOS) catalyzes the oxidation of L-arginine to yield nitric oxide (NO) and L-citrulline. The methyl arginine derivatives ADMA and NMMA, which originate from the proteolytic breakdown of methylated proteins, are endogenous inhibitors of NOS. Dimethylarginine dimethylaminohydrolase (DDAH) catabolizes ADMA and NMMA, and is itself inhibited by NO in a feedback mechanism. This figure was adapted from [5].

DDAH Structures and Mechanism

As described above, NO levels are partly regulated by asymmetric methylarginines, and asymmetric methylarginines are catabolized by DDAH. Mammals use two isoforms of dimethylarginine dimethylaminohydrolase (DDAH), DDAH-1 and DDAH-2, to regulate the plasma levels of ADMA and NMMA [22, 23]. DDAH-1 is the predominant DDAH isozyme in neuronal tissues where nNOS is enriched, whereas DDAH-2 predominates in the endothelial tissues where it is co-expressed with eNOS [22, 23]. DDAH hydrolyzes ADMA or NMMA to L-citrulline and dimethylamine or methylamine, respectively, without any known cofactors. Interestingly, mammalian DDAH-1 and DDAH-2, by sequence similarity, are not homologous to other mammalian enzymes involved in arginine metabolism. Furthermore, DDAH enzymes have been identified in certain microbes as components of conserved arginine catabolizing operons, an unexpected observation considering that these microbes do not produce methylated arginine derivatives [24, 25].

Murray-Rust et al solved the first DDAH structure from the bacterium *Pseudomonas aeruginosa* (*Pa*). The 2.37Å structure of the apoenzyme crystallized as a dimer. The overall topology of the *Pa* DDAH monomer is that of a barrel built from five ββαβ repeats with the active site lying in a negatively charged pocket at the center of the barrel (Figure 1.6) [26]. Additional structures of *Pa* DDAH complexed with both ADMA and L-citrulline gave detailed insight into the dynamics and interactions involved in substrate docking.

It was observed that residues 14-25, which are disordered in the unliganded DDAH structure, form a flexible loop that closes over the active site channel when substrate is bound [26] (Figure 1.7). This ‘cover’ is ‘latched’ by a direct hydrogen bond contact between the main chain carbonyl of Leu18 and the α-amino group of the substrate. At the active site, DDAH employs a system of hydrogen bonds to immobilize the ADMA substrate (Figure 1.8).

Figure 1.6: Structure of *Pa* DDAH. A cartoon structure figure of *Pa* DDAH showing the propeller formed by the five ββαβ repeats of the enzyme. This view is looking into the active site pocket. α-helices are shown as red cylinders and β sheets are shown as blue arrows.

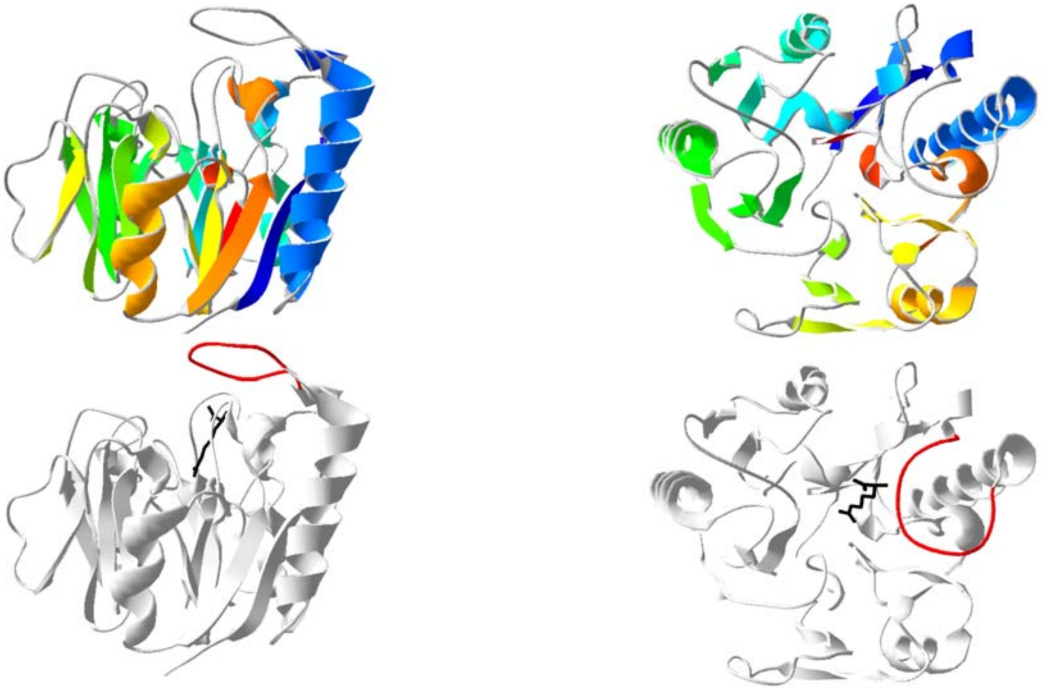

Figure 1.7: (Top) A ribbon diagram of *Pa* DDAH shown from orthogonal views; the view on the right is looking down the pseudo 5-fold axis into the active site pocket. The color scheme is blue (N-terminus) to green to red (C-terminus). (Bottom) A loop formed by residues 14-25 (shown in red) closes down over the active site when L-citrulline (black) is bound. The main chain carbonyl of L18, which hydrogen bonds to the α-amino group of L-citrulline, latches the loop over the active site.

In addition to the Leu18 hydrogen bond, the α-amino and carboxylate groups of ADMA are also held in place by the carbonyl of Ile243 and the side chains of Arg132, Arg85, and Asp60, whereas the aliphatic portion of the molecule is flanked by the side chains of Phe63 and Leu161, shielding these methylene groups from the charged side chains occupying the active site [26] (Figure 1.8). The guanidium portion of both ADMA and L-citrulline is anchored at the active site by the side chains of Asp66, which forms an ionic pair with HNε and HNω', and Glu65, which forms an ionic pair with HNω'.

The observation that the guanidium moieties of both the substrate, ADMA, and the product, L-citrulline, are bound in this manner suggests that the substrate is immobilized during catalysis. Furthermore, these specific interactions clearly illustrate DDAH's specificity for ADMA and NMMA, but not symmetric dimethyl-L-arginine (SDMA) (Figures 1.9 and 1.10). Because one of the two ω amine groups in both ADMA and NMMA are not methylated, these NH_2 groups can occupy the negatively charged hole formed by Glu66 and Asp65. In contrast to this, SDMA, which has both of its ω amine groups methylated, cannot be accommodated at the active site since it's docking would require the fitting of a $HN-CH_3$ group in a negatively charged space where a H_2N group is intended to fit, resulting in steric and electrostatic strain.

A crystal structure of human apo-DDAH-1 (hDDAH-1) was recently solved in our laboratory to 2.0Å resolution. Human DDAH-1 crystallized in the primitive monoclinic space group $P2_1$ with two monomers in the asymmetric unit [27]. The first 7 residues of the N-terminus and the last 2 residues of the C-terminus are presumed to be disordered and hence, are not visible in the electron density maps [27]. The rms distance of equivalent Cα atoms of the non-crystallographic dimer was 0.16Å, indicating that the two molecules of the asymmetric unit are virtually identical; the most significant difference between them is in the loop formed by residues 168-171 [27].

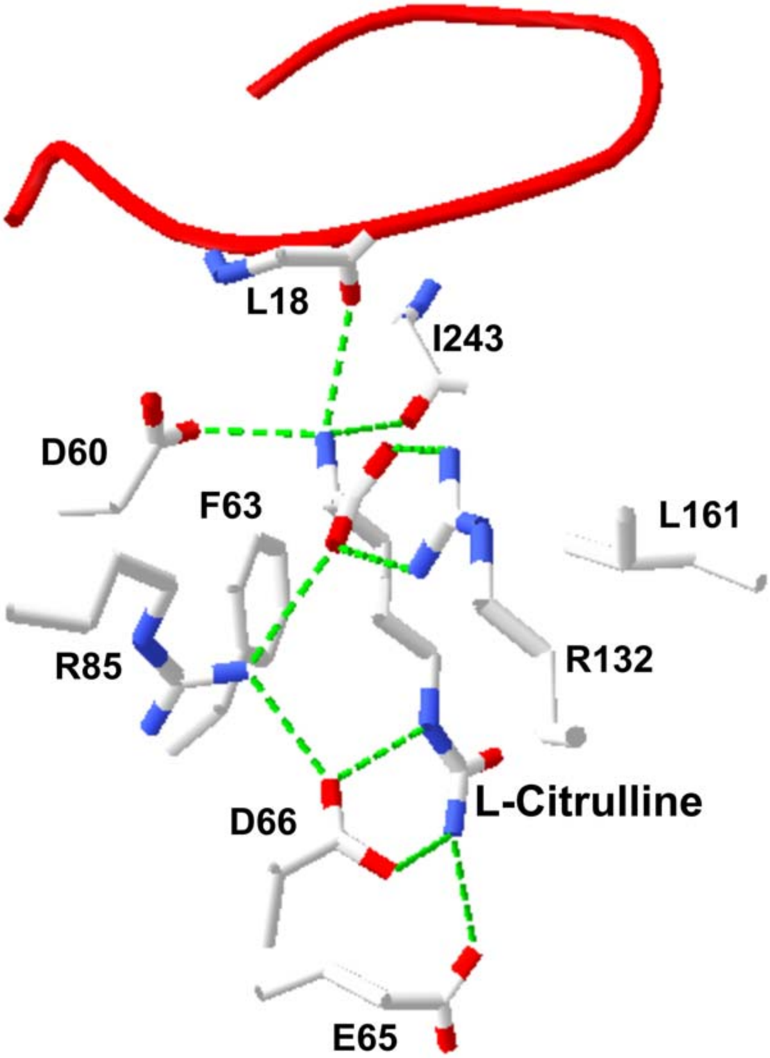

Figure 1.8: The hydrogen bonding network of the active site of *Pa* DDAH. The amino acid moiety is immobilized by hydrogen bonds to the side chain of D60 and the main chain carbonyls of L18 and I243, along with an ion pair to the side chains of R85 and R132. The HNε and HNω groups are anchored by hydrogen bonds to the side chains of D66 and E65. The β and γ methylene groups are flanked by F65 and L161, and the loop formed by residues 14-25 (red) closes over the active site.

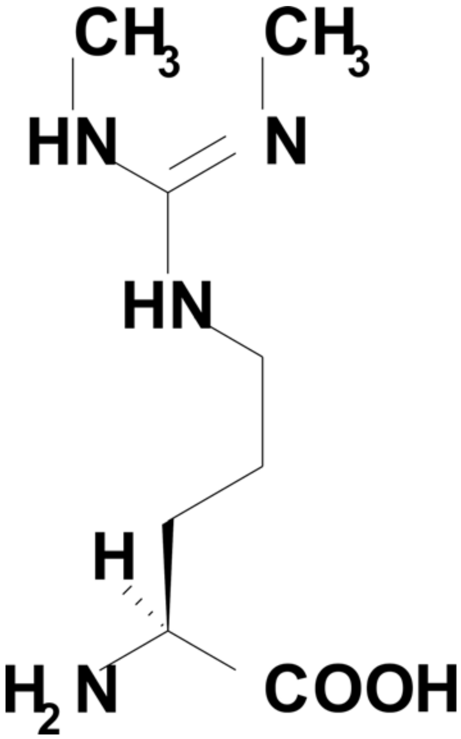

Figure 1.9: The structure of symmetric dimethyl-L-arginine (SDMA). This compound cannot by hydrolyzed by DDAH, and is cleared by the renal system without further metabolism [5].

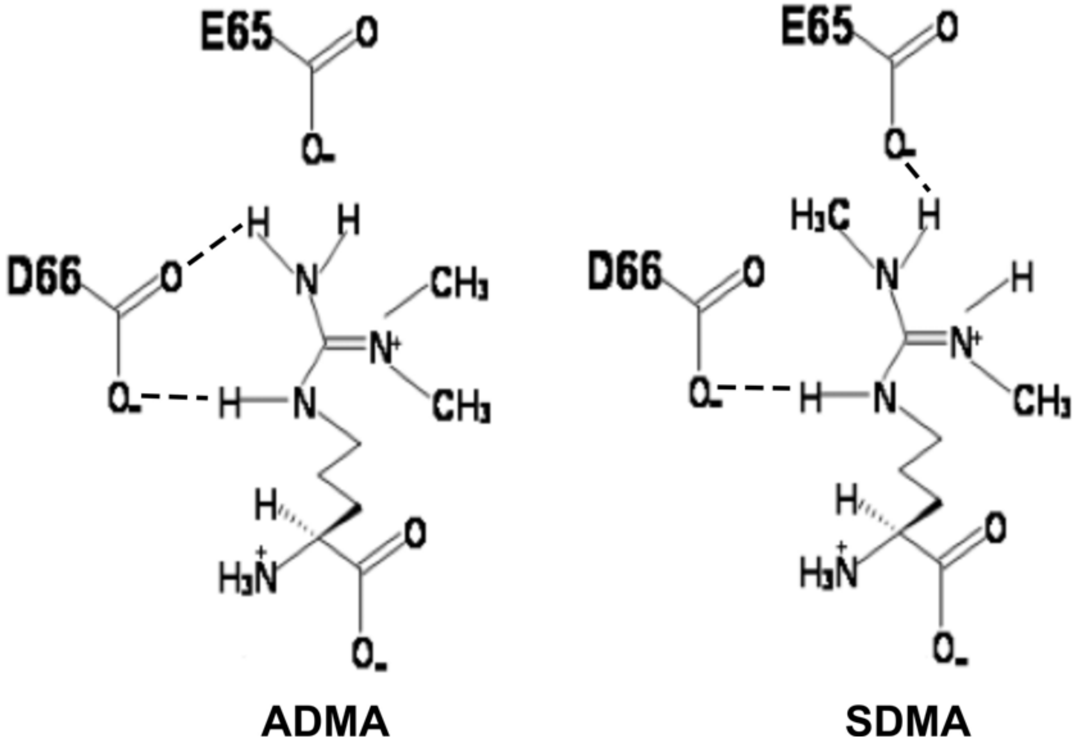

ADMA **SDMA**

Figure 1.10: Recognition of ADMA substrate by DDAH. The anionic hole created by the side chains of E65 and D66 is the mechanism by which DDAH discriminates between the substrates ADMA and NMMA and the non-hydrolyzable compound SDMA [26].

The overall fold of hDDAH-1 was akin to the *Pa* structure, a barrel structure built from five ββαβ repeats arranged around a pseudo five fold axis (Figure 1.11 and 1.12). A human DDAH-1●L-citrulline complex revealed that the methyl arginine substrate docks at the active site by a similar mechanism to the one seen with *Pa* DDAH [28] (Figure 1.13). In a similar mechanism to that seen with *Pa* DDAH, residues 25-38 form a loop structure that acts as a "lid" to close over the active site, with the main chain carbonyl group of residue L29, which is equivalent to L18 in *Pa* DDAH, acting as the "latch" (Figure 1.13). The α-amino group of the substrate is anchored down by hydrogen bonding to the carboxylate side chain of Asp72, along with bonds to the main chain carbonyl groups of L29 and V267. (Figure 1.13) The α-carboxylate group is held in place by an ion pair with the side chain of R144, while the aliphatic portion of the substrate is shielded from charged residues by the side chain of F75 (Figure 1.13). As would be expected from the *Pa* structure, the hDDAH●L-citrulline complex showed that the carboxylate side chain of D78 participates in immobilizing the guanidinium moiety of the substrate (Figure 1.13).

The core structure of *Pa* DDAH was found to be analogous to two other arginine modifying enzymes, arginine:glycine amidinotransferase and L-arginine:inosamine-phosphate amidinotransferase, and these three structures are representative of a superfamily of arginine modifying enzymes [26]. Based on the correlation between these enzymes, it was proposed that the active site residues Cys249, His162, and Glu114 constitute a catalytic triad that DDAH uses for catalysis [26]. These residues correspond to Cys273, His172, and Asp126 in human DDAH-1. A mechanism was proposed for DDAH that initiates with the carbon of ADMA being nucleophilicly attacked by the γS atom of Cys249, which had been activated by a preformed ion pair between Cys249 and His162 [26]. The tetrahedral intermediate is then hydrolyzed to form L-citrulline and dimethylamine. This mechanism is illustrated in Figure 1.14.

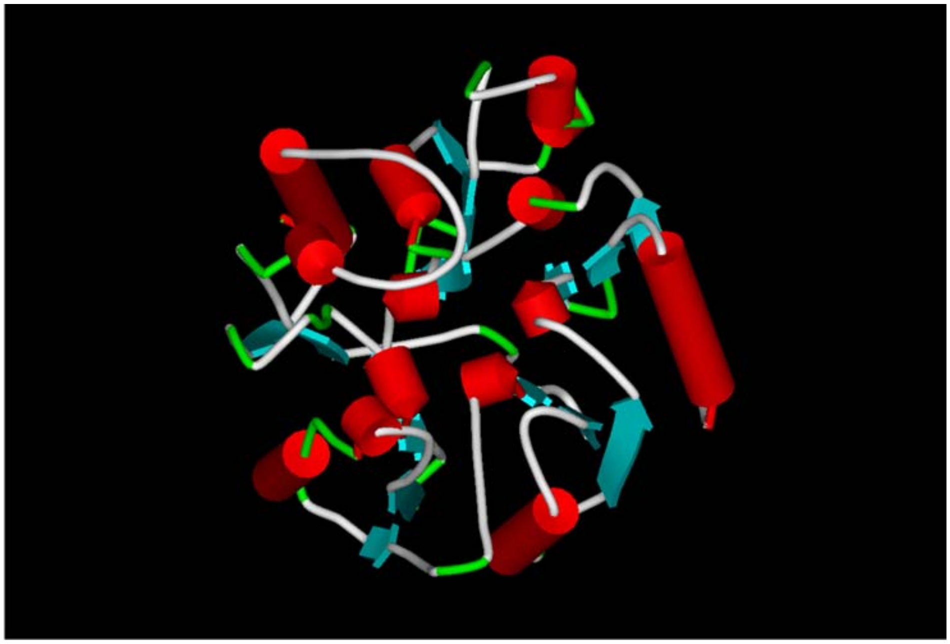

Figure 1.11: Structure of human DDAH. A cartoon structure figure of hDDAH-1 showing the propeller formed by the five ββαβ repeats of the enzyme. This view is looking down the pseudo 5-fold axis into the active site pocket. α-helices are shown as red cylinders and β sheets are shown as blue arrows.

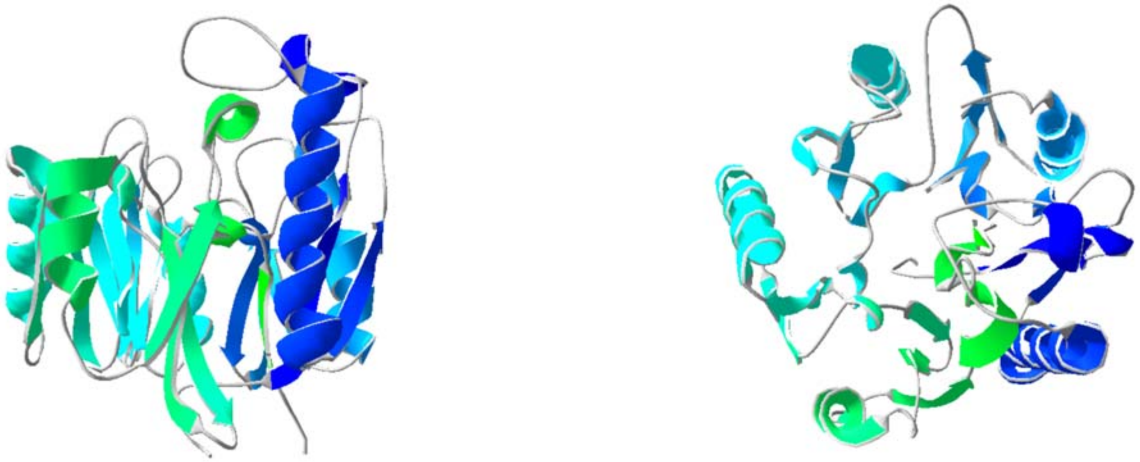

Figure 1.12: A ribbon diagram of hDDAH-1 from orthogonal views. The view on the right is looking into the active site pocket. The color scheme is blue (N-terminus) to green (C-terminus).

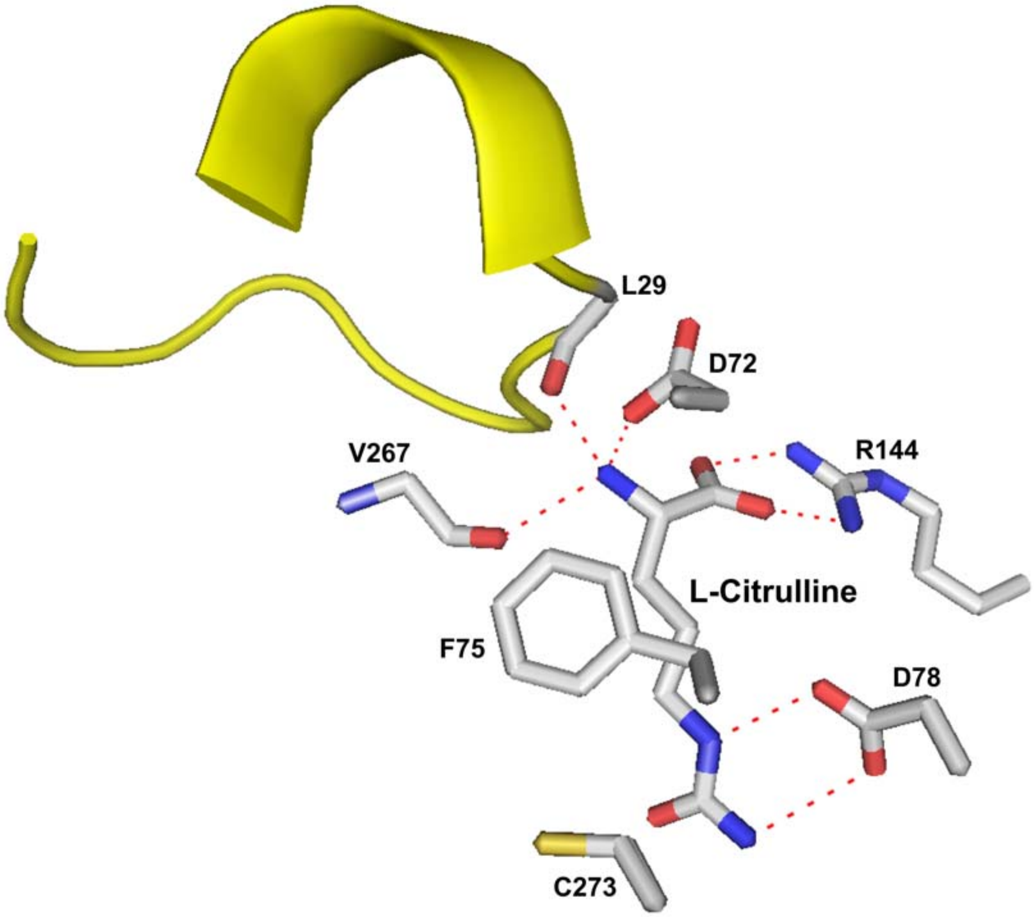

Figure 1.13: The hydrogen bonding network at the active site of hDDAH-1. The α-amine group of L-citrulline is hydrogen bonded to the main chain carbonyls of L29 and V267, in addition to the side chain of D72. F75 stacks against the β and γ methylene groups. The guanidinium moiety is covalently bound by the γS of C273 and the carboxylate side chain of D78. The loop consisting of amino acids 25-38 (yellow) closes down over the active site.

Enzymatic studies by Stone et al confirmed that Cys249 is the active site nucleophile and that the mechanism proceeds through an S-alkylthiouronium intermediate, consistent with the mechanism proposed for other members of this superfamily (Figure 1.14) [29]. Furthermore, another study by this laboratory demonstrated that the role of His162 is not to activate the nucleophilicity of the γS of Cys249, but to act as a proton donor and acceptor at different stages of the reaction mechanism (Figure 1.14) [30].

Incubation of a H162G *Pa* DDAH mutant with S-methyl-L-thiocitrulline (SMTC) resulted in the formation of a stable S-alkylthiouronium-DDAH adduct that does not hydrolyze [30]. Additionally, incubation of the mutant enzyme with N^{ω},N^{ω}-dimethyl-L-arginine did not result in the formation of a covalent intermediate [30]. Since protonation of the leaving group would be required for SMTC but not for ADMA, these observations indicated that His162 does not participate in a preformed ion pair with Cys249, but instead is responsible for protonating the leaving group in the first step of the reaction. It also activates the water nucleophile that will hydrolyze the S-alkylthiouronium intermediate in the second step of the reaction [30]. This observation seems to be in agreement with the crystal structure since His162 is positioned a relatively distant 6Å from Cys249, and the substrate actually docks in between these two residues [30] (Figure 1.15). Therefore, the observed data suggested a substrate-assisted mechanism where the active site nucleophile, the γS of Cys249, is deprotonated and subsequently activated by the binding of a positively charged substrate, and the active site His162 has dual role in protonating the substrate’s leaving group and activating a water molecule for hydrolysis [30] (Figure 1.14).

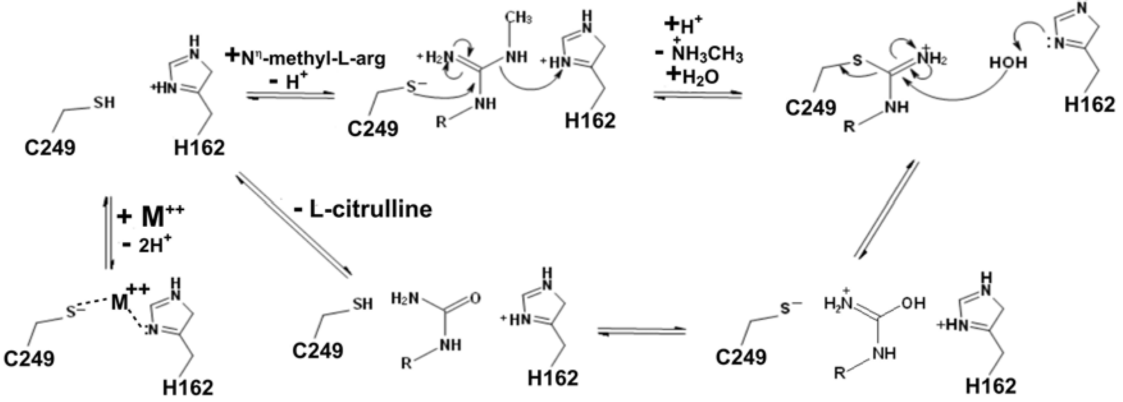

Figure 1.14: The mechanism of the hydrolysis reaction catalyzed by DDAH. Once ADMA or NMMA has docked, the reaction initiates with the nucleophilic attack by the γS of C249 on the ζC of the substrate to produce an S-alkylthiouronium intermediate. Dimethylamine or methyl amine serves as the leaving group. A water molecule is then activated by H162 to hydrolyze the covalently bound intermediate, producing L-citrulline. This figure was adapted from [30].

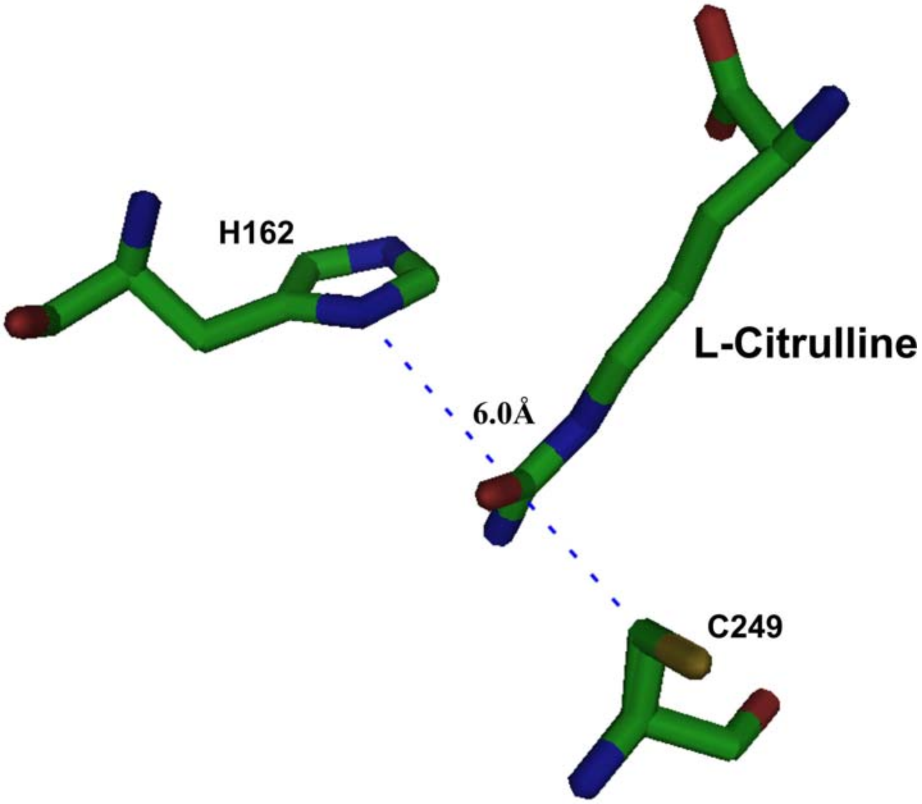

Figure 1.15: Positioning of H162 and C249 in *Pa* DDAH. In the *Pa* DDAH structure the side chain of His162 is positioned ~6.0Å away from C249, with the ligand docking between these two residues, making it unlikely that the two side chains participate in a preformed ion pair.

DDAH Regulation and Inhibition

Because DDAH contains a reactive cysteine residue, it was proposed that the enzyme may be regulated in vivo by S-nitrosylation [31]. Wild type *Pa* DDAH was found to be inactivated by NO donors *in vitro*, with activity being restored by the addition of dithiothreitol (DTT) [31]. Furthermore, a C249S site-directed mutant was not nitrosylated, confirming that the active site Cys is the residue being modified [31]. It was concluded that inactivation of DDAH in this manner represents an *in vivo* feedback mechanism whereby rising levels of NO lead to S-nitrosylation and subsequent inactivation of DDAH [31]. As a result of this feedback mechanism, levels of ADMA would increase and inhibit NOS, retarding the synthesis of NO. Furthermore, it has also been discovered that Zn(II) can act to inhibit mammalian and *Pa* DDAH activity, and Stone et al confirmed that the Zn(II) metal ion chelates to the Cys249 and His162 active site residues of *Pa* DDAH, inactivating the protein (Figure 1.14).

Overproduction of NO has been identified in practically every organ system as the cause of several pathophysiological changes, and reduction of NO production from iNOS is desirable to combat pathophysiological conditions such as septic shock, inflammatory pain, arthritis, and asthma [5]. Furthermore, NO production at low levels has been associated with the growth of a myriad of cancers, most likely due to the angiogenic properties of the compound [8]. As a result of these findings, compounds that inhibit NO production, by inhibiting NOS, DDAH-1, or both of these enzymes, may prove useful as anticancer drugs [27]. However, because of specific properties of the two proteins along with the tissue specific isoforms that exist for both enzymes, designing effective drugs that inhibit NO production seems to be a complex problem [27].

Although some success has been achieved with the design of compounds that selectively inhibit different isoforms of NOS, compounds that inhibit both NOS and DDAH seem to be the most attractive drug candidates since they would be consistent with a "kill two birds with one stone" approach to inhibiting NO production [27]. Leiper et al solved an enzyme●inhibitor complex of DDAH-1 and L-257, a methyl arginine analog that inhibited DDAH-1 with a sub 25μM IC_{50} [28]. Although, L-257 bound with some similarity to the L-citrulline structure some significant differences at the active site were observed (Figures 1.16 and 1.17). Consistent with the model seen with L-citrulline, the flexible loop made by residues 25-38 folds down over the active site with the carbonyl of Leu29 hydrogen bonding to the α-amino group, which is also bound by hydrogen bonds with Val267 and Asp72. Additionally, hydrophobic stacking is observed with the side chain of Phe75 and two of the nitrogens of the guanidino moiety are recognized by Asp78. However, unlike the docking model seen in the L-citrulline structure, the inhibitor is bound in a "bent" conformation and the side chain of Arg144 is rotated away from the active site and does not form an ion pair with the α-carboxylate group of L257 [28]. Furthermore, at the guanidino portion of L-257, the side chain of Glu77 does not recognize the unsubstituted NH_2 group, an interaction that was observed in the L-citrulline structure. Perhaps the most striking difference between these two structures is the position of His172, which has rotated further away from the bound inhibitor when compared to its position in the L-citrulline structure (Figure 1.17).

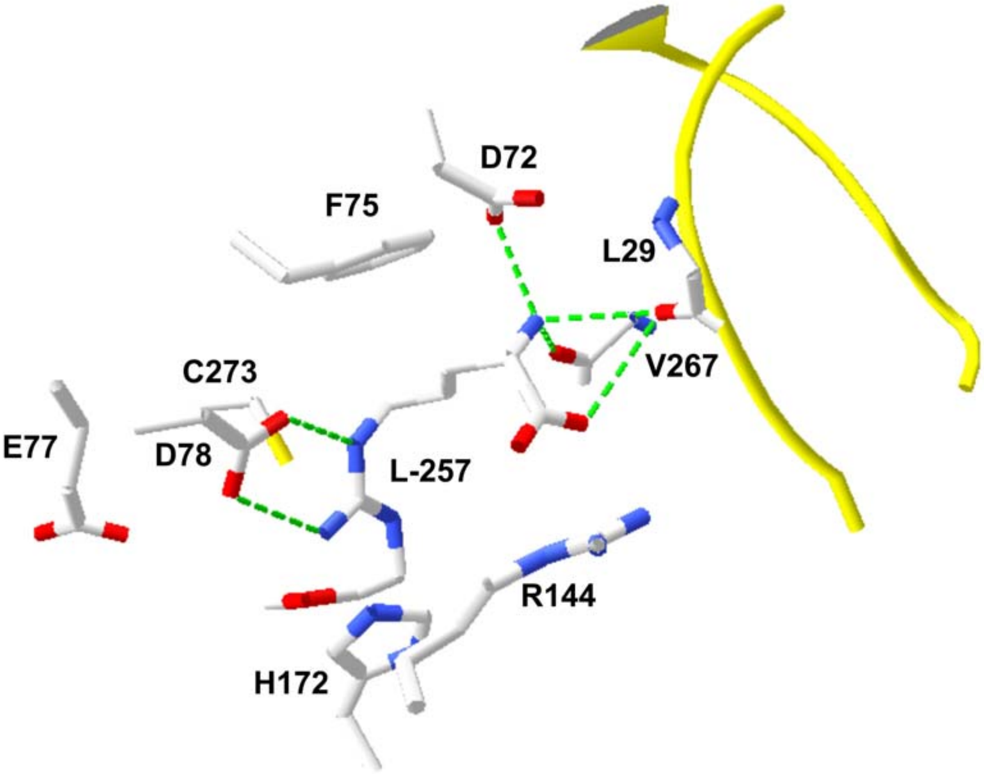

Figure 1.16: The hDDAH-1●L-257 complex. The carboxylate side chain of D72, along with the main chain carbonyls of L29 and V267 anchor the α-amino and α-carboxylate groups of L-257. D78 acts to hydrogen bond to the HNε and HNω groups of L-257's guanidine moiety. F75 stacks against the β and γ methylene carbons of the inhibitor, and the flexible loop formed by residues 25-38 (yellow) has closed down over the active site.

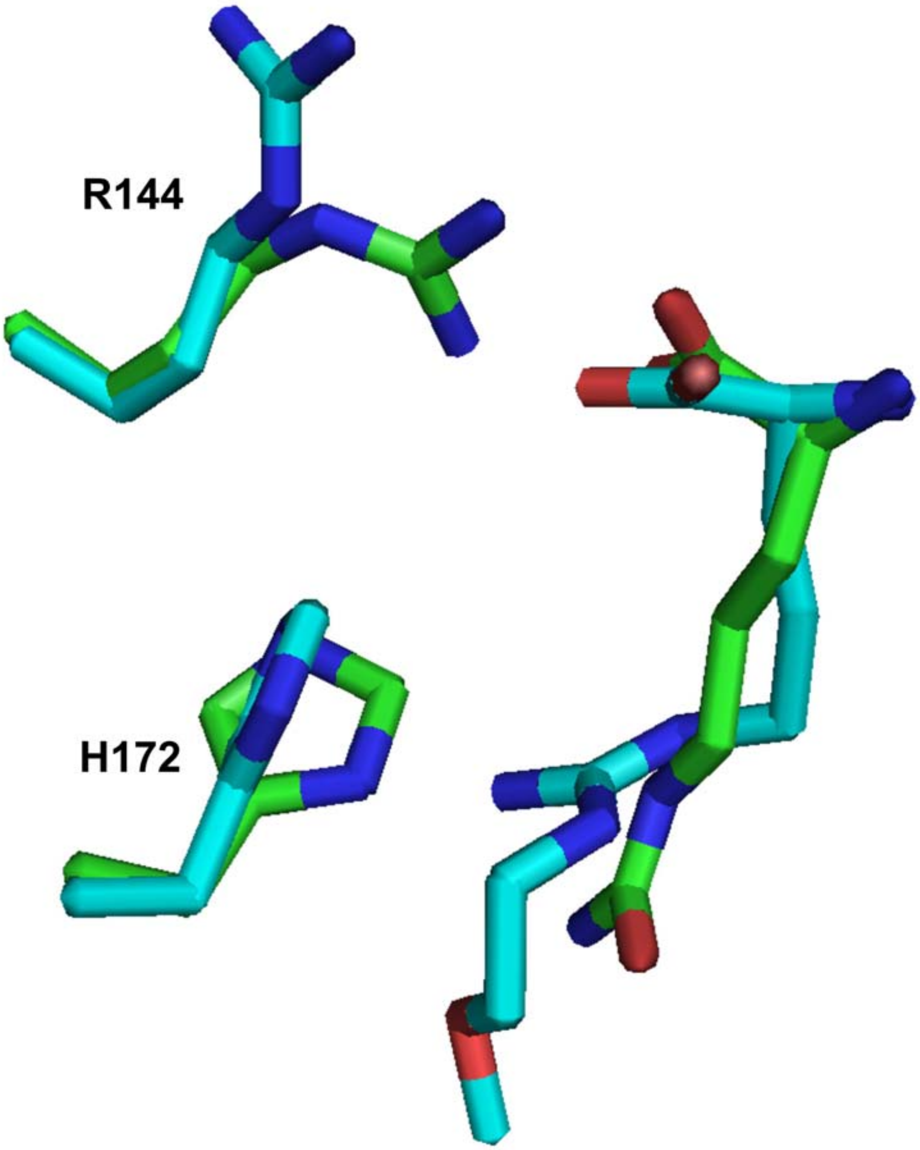

Figure 1.17: Alignment of hDDAH-1●L-citrulline and hDDAH-1●L-257 structures. A super imposition of the active sites of DDAH-1 with the ligands L-citrulline (green) and L-257 (blue) illustrating the differences in the positions of the side chains of R144 and H172. When L-257 is bound, R144, which hydrogen bonds to L-citrulline's carboxylate group, is observed to be facing away from the ligand, and H172 has tilted away from the active site cleft to free up space that the bound inhibitor will occupy.

Fast and coworkers assayed for DDAH-1 inhibition by known NOS inhibitors belonging to three different classes of compounds: S-alkyl isothioureas, aminoguanidines, and amidines. Although the S-alkyl isothioureas and the aminoguanidine compounds were not inhibitors, the amidino class of compounds did show some promise as a scaffold for a dual-targeted inhibitor since one of these compounds, N^5-(1-iminoethyl)-L-ornithine (L-NIO) inhibited DDAH-1 weakly (K_I = 990μM) [27] (Figure 1.18).

Secondary inhibition experiments using the alkyl-substituted amidines N-(1-iminopropyl)-L-ornithine (L-IPO), N-(1-iminopentyl)-L-ornithine (L-IPnO), and N-(1-iminohexyl)-L-ornithine showed that inhibition of DDAH-1 depended in some part on the length of the alkyl substituent [27]. The inhibitor L-IPO, which is one methylene group longer than L-NIO, proved to be a 20-fold stronger inhibitor of DDAH-1 than L-NIO [27]. Furthermore, L-IPnO, which is two methylenes longer than L-IPO and three methylenes longer than L-NIO, displayed 7-fold stronger inhibition over L-IPO [27]. However, further extension of the alkyl substituent does reach a tipping point as L-IPnO proved to be a more effective inhibitor than N-(1-iminohexyl)-L-ornithine [27]. Branching of the alkyl substituent did not augment inhibition as N-(1-iminoisobutyl)-L-ornithine has a K_I value on the same order as L-IPO [27]. Interestingly, whereas extension of the alkyl chain resulted in higher inhibitor potency between L-NIO, L-IPO, and L-IPnO, it had the opposite effect on NOS inhibition as extending L-IPO into N-(1-iminohexyl)-L-ornithine resulted in a greater than 1000-fold decrease in inhibition of NOS (this resulted in only a two-fold decrease in inhibition for DDAH-1) [27].

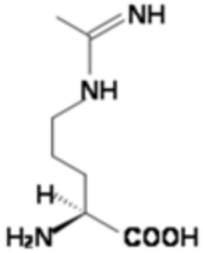

L-NIO
K_i DDAH-1 = 990μM
K_i nNOS = 1.7μM

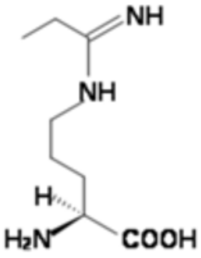

L-IPO
K_i DDAH-1 = 52μM
K_i nNOS = 3μM

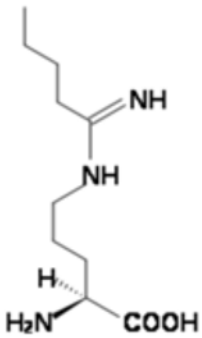

L-IPnO
K_i DDAH-1 = 7.5μM
K_i nNOS = 20μM

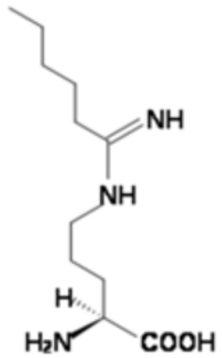

N-(1-iminohexyl)-L-ornithine
K_i DDAH-1 = 110μM
K_i nNOS = 1900μM

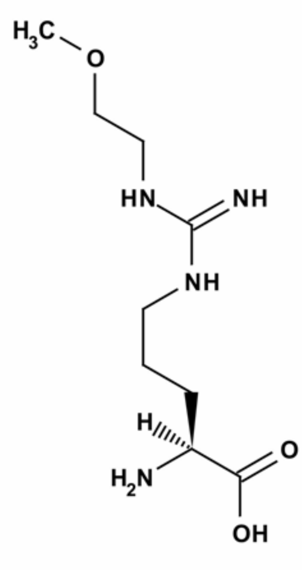

L-257
IC_{50} hDDAH-1 < 25μM

Figure 1.18: Inhibitors of hDDAH-1. L-NIO, L-IPO, L-IPnO, and N-(1-iminodexyl)-L-ornithine are inhibitors of human DDAH-1 belonging to the guanidinium class of compounds. Extending the ethyl alkyl chain of L-NIO to a pentyl alkyl chain increased inhibition 140-fold.

The Fast group studied the inhibition of hDDAH-1 by L-IPO in further detail using solution NMR and site-directed mutagenesis. In collaboration with our group, the hDDAH-1●L-IPO complex was crystallized in the space group $P2_1$ with two molecules in the asymmetric unit. This enzyme-inhibitor complex was solved to 1.9Å resolution. The first 4 residues of the N-terminus and the last 3 residues of the C-terminus are not seen in the electron density map. The Cα atoms of the hDDAH-1●L-IPO complex and the apo-hDDAH-1 are in similar positions (rms distance of 0.30Å). From the hDDAH-1●L-IPO X-ray structure it was found that L-IPO binds in essentially the same way as other DDAH-1 substrates, however, strong, continuous electron density extending from the γS of Cys274 to the C of L-IPO indicated that the enzyme●inhibitor complex crystallized as a covalent adduct (Figure 1.19 and 1.20) (Note: the numbering sequence for the hDDAH-1●L-IPO structure is advanced by 1, i.e. the active site nucleophile is Cys274 in this structure and Cys273 in the hDDAH-1●L-257 structure).

Besides the covalent bond to the enzyme, the L-IPO inhibitor makes a hydrogen bond interaction between the carboxylate side chain of Asp73 and L-IPO's α-amino group; the amino group is also recognized by the main chain carbonyls of Leu30 and Val268 (Figure 1.19). The α-carboxylate of the inhibitor ion pairs with the side chain of Arg145, whereas the aliphatic chain hydrophobicly interacts with the side chains of Leu271 and Phe76 (Figure 1.19). Consistent with the interactions participating in the docking of L-citrulline, the guanidinium group of L-IPO is recognized by Glu78 and Asp79 (Figure 1.19).

Unlike the hDDAH-1●L-257 structure, the only significant difference in the position of active site residues was that of His173, which again is observed to be further away from the bound L-IPO than it was from L-citrulline (Figure 1.21). However, the side chain of Arg145 was observed to form an ion pair to the α-carboxylate group, which was not observed in the DDAH-1●L-257 structure.

The contributions of a subset of these interactions to L-IPO docking were investigated by site-directed mutagenesis in the Fast laboratory. An E78A mutation reduced the energy of L-IPO docking by 1.9 kcal/mole [27]. Although salt bridges of this type usually contribute 3-4 kcal/mole to the stabilization energy, this lower value was expected since Glu78 also forms a salt bridge with Lys175 [27]. A L271G mutation reduced the stabilization energy of binding by 1.0 kcal/mole, completely consistent with a value expected for this hydrophobic interaction [27].

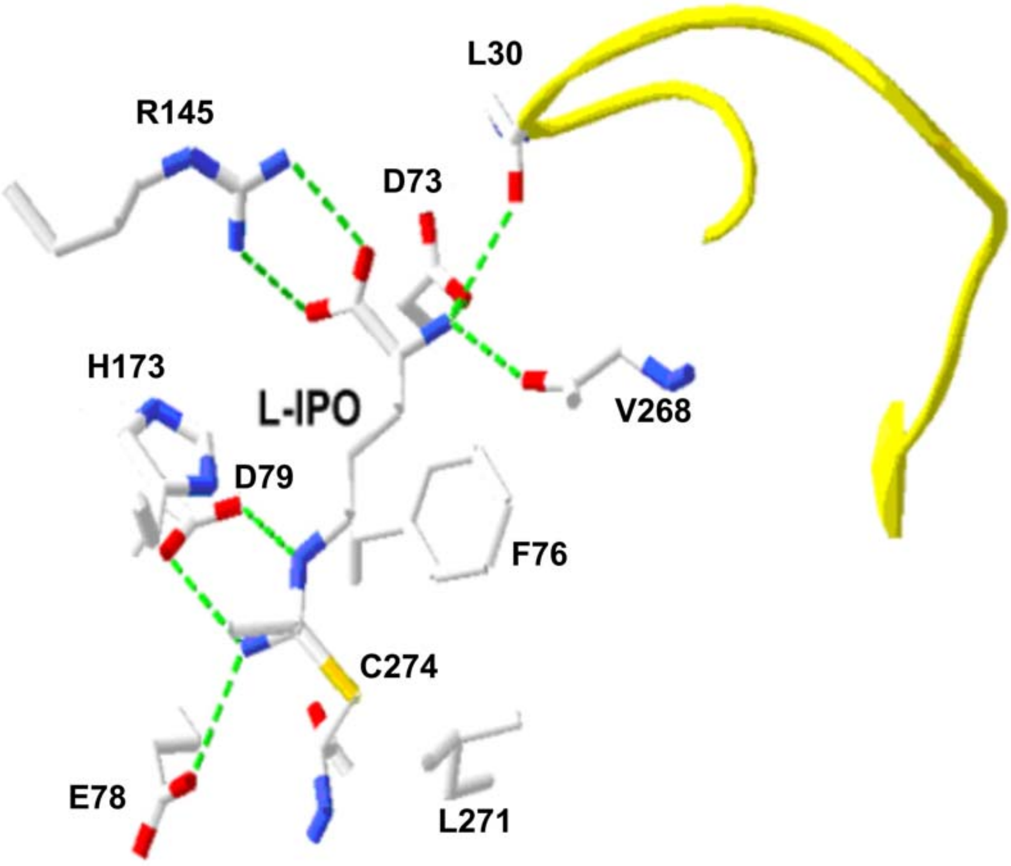

Figure 1.19: The docking of L-IPO at the active site of hDDAH-1. The amino acid moiety of L-IPO is bound by ion pairing to R145 along in addition to hydrogen bonding with the side chain of D73 and the main chain carbonyls of L30 and V268. The guanidine moiety is hydrogen bonded to the carboxylate side chains of D79 and E78 in addition to a covalent linkage between the ζC of L-IPO and the γS of C274. The loop formed by residues 25-38 is in a closed conformation over the active site (yellow).

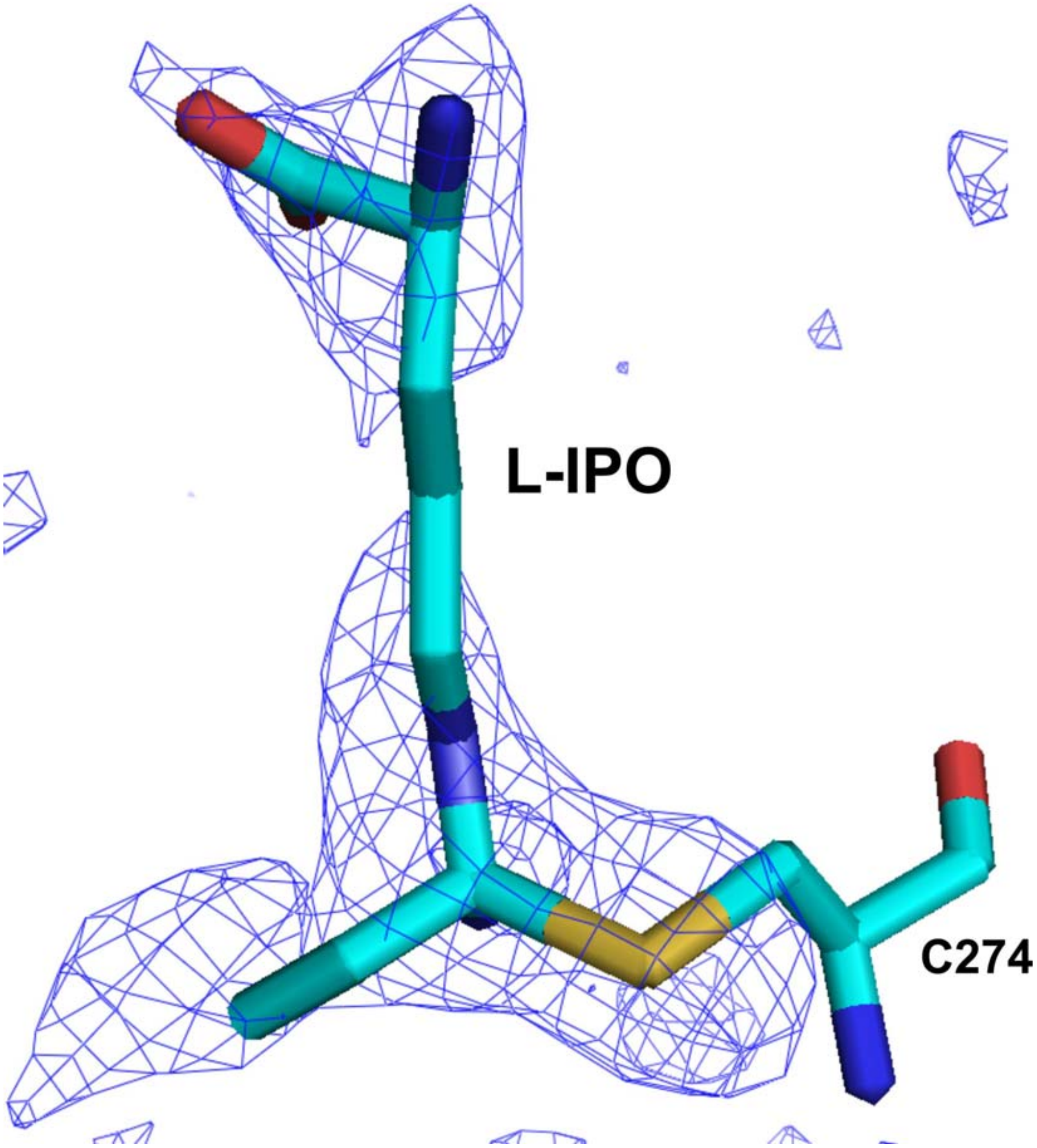

Figure 1.20: The Fo-Fc difference map for the hDDAH-1●L-IPO complex. The Fo – Fc map at a 3σ contour showing continuous, strong electron density extending between the γS atom of C274 and the ζC of L-IPO, indicative of a covalent linkage between the two atoms.

Furthermore, when the Leu30 “latch” was mutated to alanine, a reduction in L-IPO inhibition was also observed, indicating that flap closure makes some contribution to inhibitor binding, as it does with substrate binding. However, no major secondary structure rearrangements appear to occur as measure by a lack of significant changes in the circular dichroism spectrum [27].

Although the crystal structure showed that L-IPO inhibited through the formation of a covalent adduct, additional experiments showed that the mode of inhibition is not irreversible since mass spectrometry did not detect any covalent adducts and activity could be restored by diluting into inhibitor free buffer [27]. Furthermore, the possibility that L-IPO is a non-ideal substrate for DDAH-1, and by default, an inhibitor, was also dismissed since no hydrolysis of L-IPO was detected [27]. Because a covalent or noncovalent complex could not be detected by ^{13}C NMR experiments, it was concluded that L-IPO is basically a competitive inhibitor that acts to form a non-hydrolyzable tetrahedral adduct via the linkage of the γS of Cys274 (which is designated as Cys273 in the hDDAH-1●L-citrulline and hDDAH-1●L-257 structures) and the ζC of L-IPO. This bond is very weak and the reversibility of inhibition is due to the formation and cleavage of the bond being in rapid equilibrium [27]. It is important to point out that other enzymes that use Cys as a nucleophile also form reversible covalent adducts, and specifically, arginine deiminase, another member of the pentein superfamily, has been observed to form a tetrahedral enzyme-inhibitor adduct [27].

When one compares the structure of native hDDAH-1 with the L-IPO, L-citrulline, and L-257 structures some variation in the positioning of active site residues and even flexibility in the ligand conformation has been observed (Figure 1.17 and 1.21).

Between these four structures, His173 (which is designated as His172 in the hDDAH-1●L-citrulline and hDDAH-1●L-257 structures), a direct participant in the enzymatic mechanism, is in closest proximity to the ligand in the hDDAH-1●L-citrulline structure. The loop consisting of residues ^{169}ADGL^{172} is ordered in the native and L-IPO structures, it is disordered in the L-citrulline and L-257 structures [27].

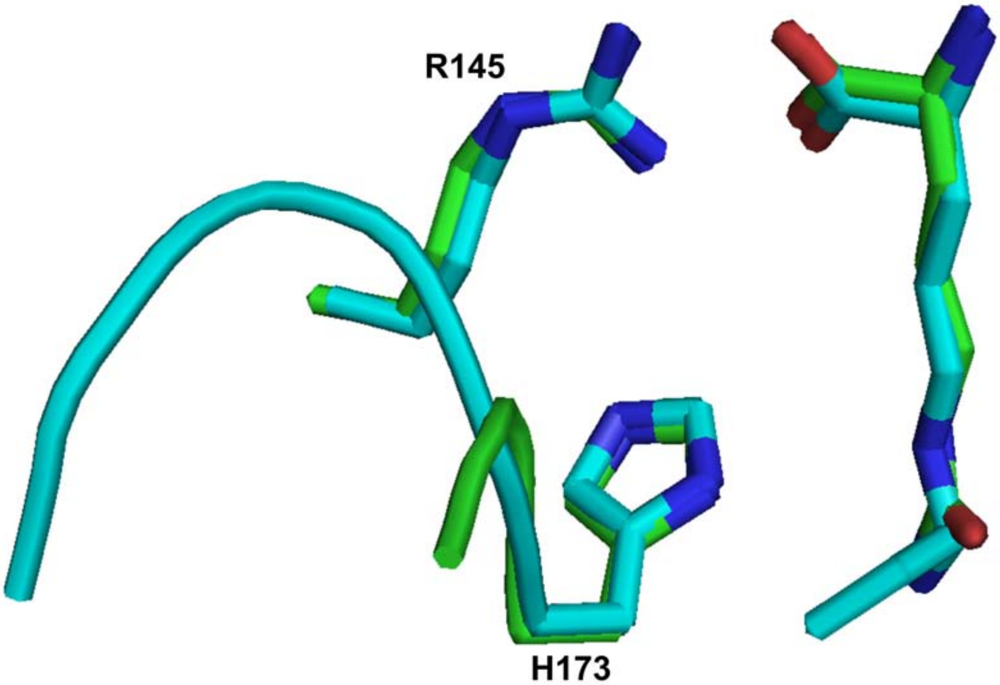

Figure 1.21: A superimposition of hDDAH-1●L-citrulline (green) and hDDAH-1●L-IPO (blue). The loop preceding H173 in the L-IPO structure, consisting of residues ^{169}ADGL^{172} is ordered in this structure and disordered when L-citrulline is bound, however, H173 is not positioned as far away from the L-IPO ligand than it was from the L-257 ligand. Note: the hDDAH-1●L-IPO sequence is advanced by one compared with other hDDAH-1 sequences i.e. the active site His is H173 for this structure.

The hDDAH-1●L-IPO structure demonstrated that alkyl substituted amidines are promising scaffolds for the design of dual target therapeutics that can control NO production, since these compounds can effectively inhibit both NOS and DDAH-1; it appears that the alkyl substituent may determine which of the two enzymes it is more specific for. Although these initial inhibition studies with alkyl substituted amidines yielded encouraging results, further structural studies of hDDAH-1-amidine complexes are warranted. In particular, we want to address why inhibition at least partially depends on alkyl chain length, for the design of more potent DDAH-1/NOS inhibitors.

In addition to the substituted amidines, the Fast laboratory has reported that ebselen, a selenium containing compound, inhibits DDAH-1 with an IC_{50} of 300nM (Figure 1.22). The inhibition seems to be irreversible since dilution into inhibitor free buffer did not restore activity, in contrast to the case with L-IPO inhibition. It is believed that ebselen's mode of inhibition is to form a covalent adduct with either Cys273 or His172. Ebselen is the most potent DDAH-1 inhibitor to date and represents a new scaffold for future design of DDAH-1 inhibitors. An X-ray structure of the DDAH-1●ebselen complex would prove extremely useful for the future design of inhibitors.

Ebselen

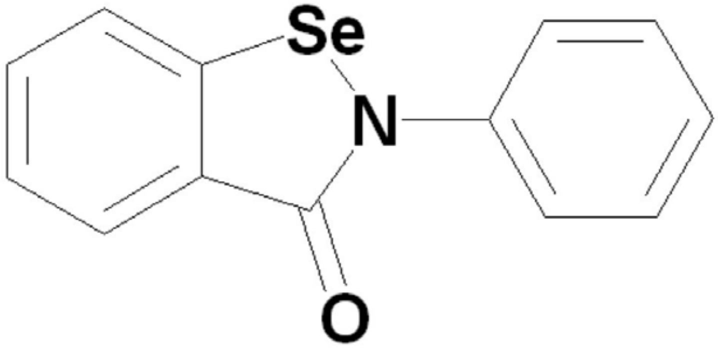

IC_{50} DDAH-1 = 300nM

Figure 1.22: The structure of ebselen.

Project Goals

Because of its role in a litany of pathophysiological states, cellular nitric oxide production, specifically, regulation of NO production through the selective inhibition of NOS and DDAH is an area of intense research. However, at the onset of this research project only three known hDDAH-1●inhbitor structures existed and represented a small pool of structural information from which to design more effective inhibitors for this enzyme. As a collaborative effort with the Fast research group (The University of Texas at Austin), the goals of this project were to crystallize and solve the structure for enzyme inhibitor complexes of hDDAH-1 with the compounds L-IPnO and ebselen. These structures presented in this study contribute important information that allows for the progress of drug design in this research field.

Chapter 2: Materials and Methods

Materials

Plasmids containing the human DDAH-1 gene cloned into pET28a (Novagen, Madison, WI) were generously provided by the Fast laboratory (University of Texas at Austin, Austin, TX). Ni-NTA His-Bind® resin was obtained from Novagen (Madison, WI). The pre-packed HiLoad 16/60 Superdex S-200 prep grade column was obtained from GE healthcare (Piscataway, NJ).

Methods

Expression and purification of recombinant hDDAH-1

The pET28a-DDAH isoform 1 (*H. sapians*) vector was transformed into *E. Coli* strain Rosetta 2 (DE3) under the dual selection of kanamycin and chloramphenicol. The 285aa ORF encodes a 6X His●Tag fused to the N-terminus. Fresh transformants were grown in Terrific Broth media (Difco) at 37 °C until reaching an optical density of 0.7. Upon reaching this OD the hDDAH-1 protein was expressed by the addition of isopropyl β-D-1-thiogalactopyranoside (IPTG) to a final concentration of 1mM. Cells were allowed to grow for another 3 hours post induction, and were harvested by centrifugation at 4000g for 10 minutes. Cells were resuspended in lysis buffer (25mM Tris-HCl pH 8, 250mM NaCl) and run through a French Pressure cell 3 times at 1000 PSI. Cell debris was removed by centrifugation at 30,000g for 1 hour and the crude cell lysate was passed though a column packed with Ni-NTA His-Bind® resin. The column was washed with 500 mL of a 25 mM Tris-HCl pH 8, 250mM NaCl, 10mM imidazole buffer and the heterocomplex was eluted with a linear gradient from 10 – 250mM imidazole. Protein containing fractions were pooled together and dialyzed against a 10 mM Tris-HCl 50 mM KCl buffer and concentrated. The recombinant hDDAH-1 was further purified by gel filtration using a HiLoad 16/60 Superdex S-200 prep grade column and an AKTA FPLC system (GE Healthcare, Piscataway, NJ). The protein was loaded onto the S-200 column that had been previously equilibrated with a 10mM Tris-HCl pH 8, 50mM KCl buffer and run through the matrix at a flow rate of 1mL/min. Protein containing fractions were pooled together, concentrated, and stored at 4 °C.

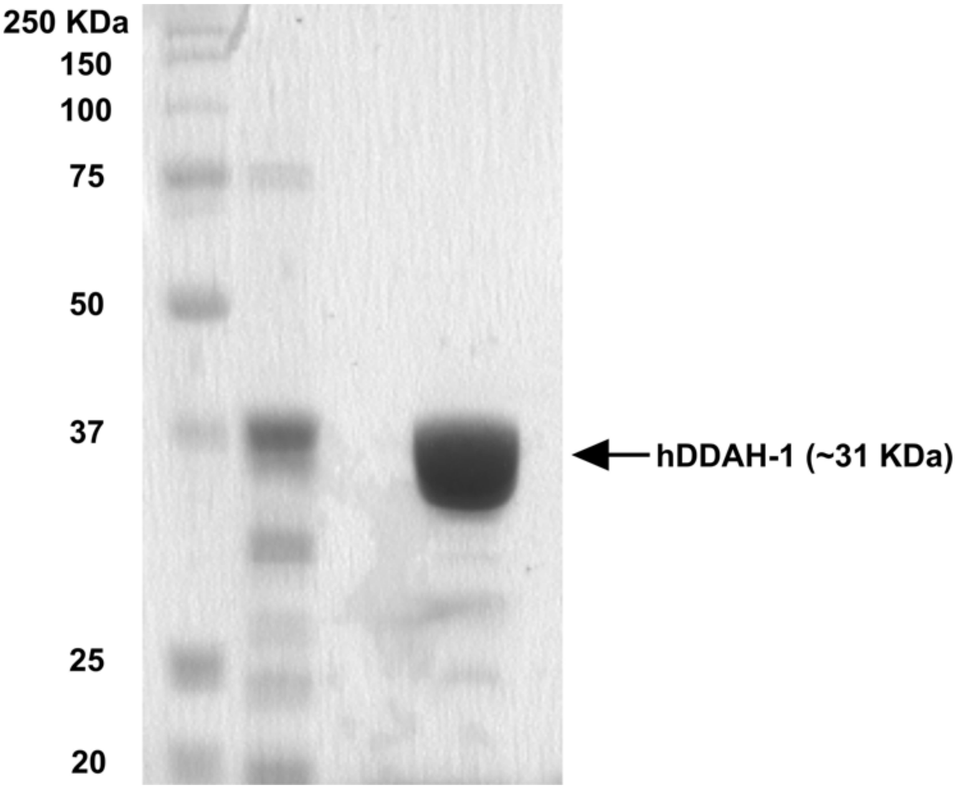

Figure 2.1: A 12% SDS PAGE gel of hDDAH-1 purified by gel filtration on a Superdex S-200 column. Lane 1: Molecular weight standards, Lane 2: Eluted A_{280} peak containing impurities, Lane 3: Eluted A_{280} peak containing purified hDDAH-1.

Crystallization of hDDAH-1●L-IPnO and hDDAD-1●ebselen complexes

The purified hDDAH-1 protein was concentrated to 15-17mg/mL, as determined by OD_{280} absorption readings and Beer's Law:

$$C = A/\varepsilon b$$

Where:

C = the protein concentration (mg/mL)
A = the absorption at 280nM
ε = the extinction coefficient of hDDAH-1; calculated as 0.30 $(mg/mL)^{-1}cm^{-1}$
b = the cuvette pathlength, 1cm

The best quality hDDAH-1 crystals were grown from a mother liquor of 0.1M Tris-HCl pH 8.2, 20% polyethylene glycol 6000 (Figure 2.2). Briefly, crystal drops were set up using the sitting drop method by combining 3 μL of the hDDAH-1 sample with 3 μL of mother liquor in a VDX crystallization plate (Hampton Research, Aliso Viejo, CA), sealed with tape, and allowing the drop to equilibrate at 4 °C. Crystals for the enzyme●inhibitor complexes of hDDAH-1●L-IPnO and hDDAH-1●ebselen were obtained by separately adding corresponding volumes of stock solutions of L-IPnO and ebselen to crystal containing drops to yield final concentrations of 150µM and 480µM respectively, and allowing re-equilibration overnight.

Cryo-cooling and Data collection of hDDAH-1●L-IPnO and hDDAH-1●ebselen crystals

The hDDAH-1●L-IPnO and hDDAH-1●ebselen crystals were removed from the sitting drop using a nylon loop, soaked in a 0.1M Tris pH 8.2, 35% polyethylene glycol 6000 solution, and flash frozen in liquid nitrogen. The crystals were then mounted for data collection.

Data processing of hDDAH-1●L-IPnO and hDDAH-1●ebselen crystals

Data collected for both enzyme●inhibitor complexes were processed using HKL2000 suite [32]. XDISPLAYF was first employed to display raw x-ray diffraction data as images and identify diffraction maxima for each of the two enzyme●inhibitor data sets. DENZO was then used to index the reflection intensities and cell refinement of each of the two data sets. SCALEPACK was used to scale and merge the data. Both enzyme inhibitor complexes belong to the primitive monoclinic space group $P2_1$. The hDDAH-1●LIPnO had the cell constants a = 47.21Å, b = 80.90Å, c = 74.09Å, $\alpha = 90$, $\beta = 90.13$, γ

= 90. The hDDAH-1●ebselen crystals had the cell constants of a = 47.501Å, b = 81.050Å, c = 74.013Å, $\alpha = 90$, $\beta = 90.11$, $\gamma = 90$.

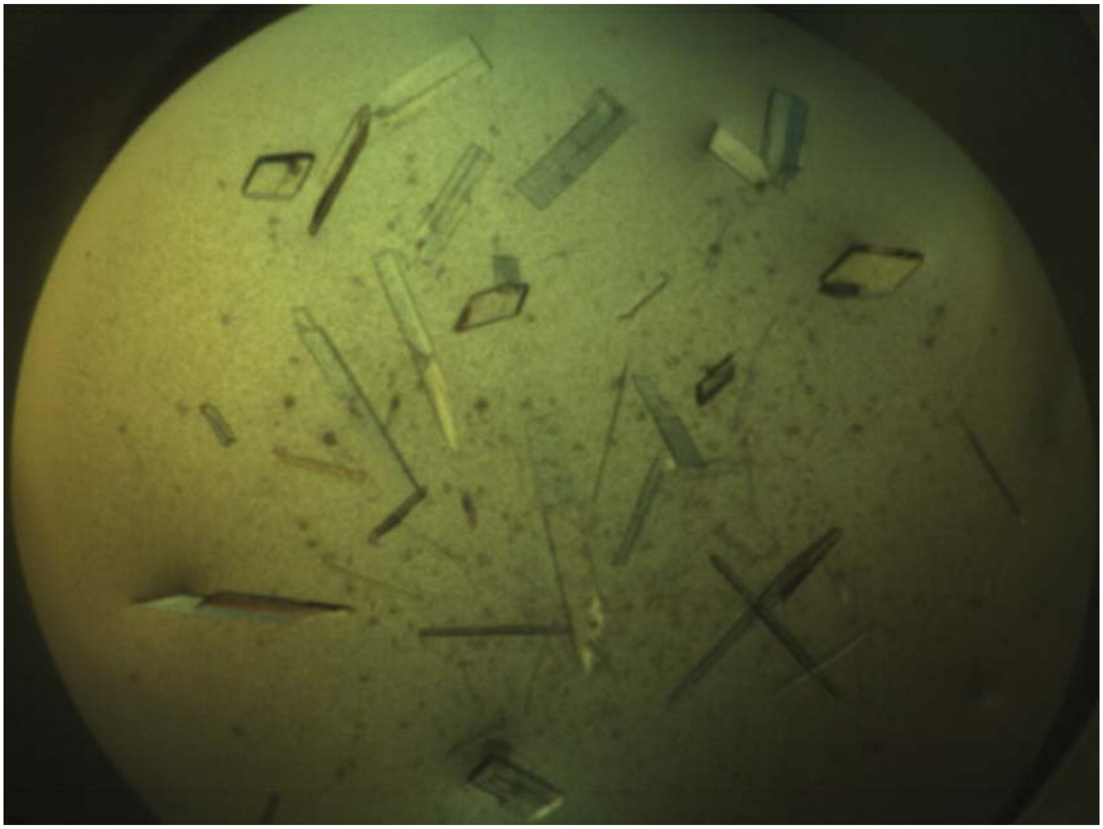

Figure 2.2: DDAH-1 crystals. The best quality crystals were grown from a mother liquor of 0.1M Tris-HCl pH 8.2, 20% polyethylene glycol 6000.

Molecular replacement

Molecular replacement solutions for the hDDAH-1●L-IPnO and hDDAH-1●ebselen data were executed using hDDAH-1 as the search model. Structure factors for both enzyme●inhibitor complexes were calculated using CCP4 [32] and input into PHASER (CCP4 suite) to produce the initial 2Fo-Fc and Fo-Fc electron density maps and preliminary hDDAH-1 coordinates.

Model Building and Refinement

The hDDAH-1 models for both enzyme●inhibitor complexes were fit to the 2Fo-Fc and Fo-Fc maps using COOT [33] at a 1σ and 3σ level contours, respectively. The apo-DDAH-1 structures were built using COOT, and the functional coordinate, parameter, and topology data for both inhibitors were made using the PRO DRUG SERVER [34]. The inhibitors were then modeled into their respective electron density maps using COOT. The hDDAH-1●L-IPnO and hDDAH-1●ebselen structures were run through several rounds of refinement using CNS and PHENIX [35]. Because PHENIX determined that the hDDAH-1●ebselen data were twinned, this data had to be further processed using PHENIX and CCP4 to detwin the data. For refinement of both enzyme●inhibitor complexes, non-crystallographic symmetry restraints were used. The positions of ordered water molecules in the hDDAH-1●ebselen structure were predicted and modeled using COOT.

Model Assessment

The phi and psi angle compatibility of the models was assessed using PROCHECK. The DDAH-1●IPnO model had 86.3% of its residues in the most favorable regions of the Ramachandran plot, with 12.7% lying in additional allowed regions and 1% lying in generously allowed regions with no residues having disallowed phi and psi conformations. The DDAH-1●ebselen model had 81.3% of its residues in the most favorable regions of the Ramachandran plot, with 15.8% lying in additional allowed regions and 2.9% lying in generously allowed regions with no residues having disallowed phi and psi conformations.

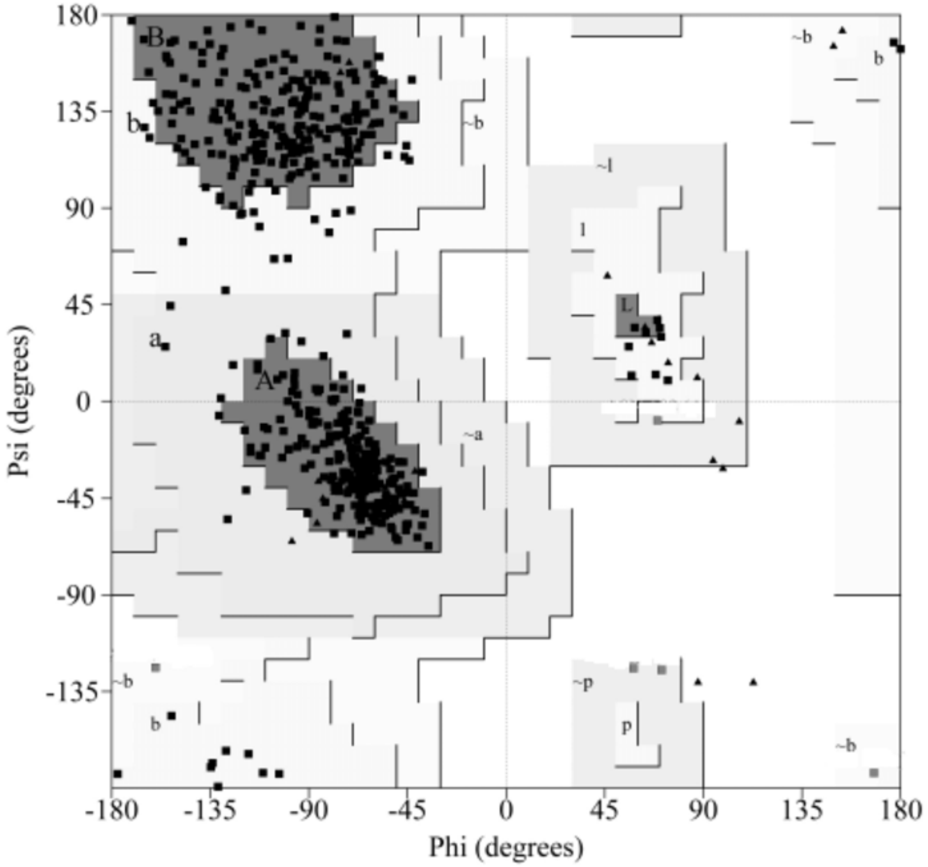

Figure 2.3: The Ramachandran plot of the hDDAH-1●L-IPnO structure.

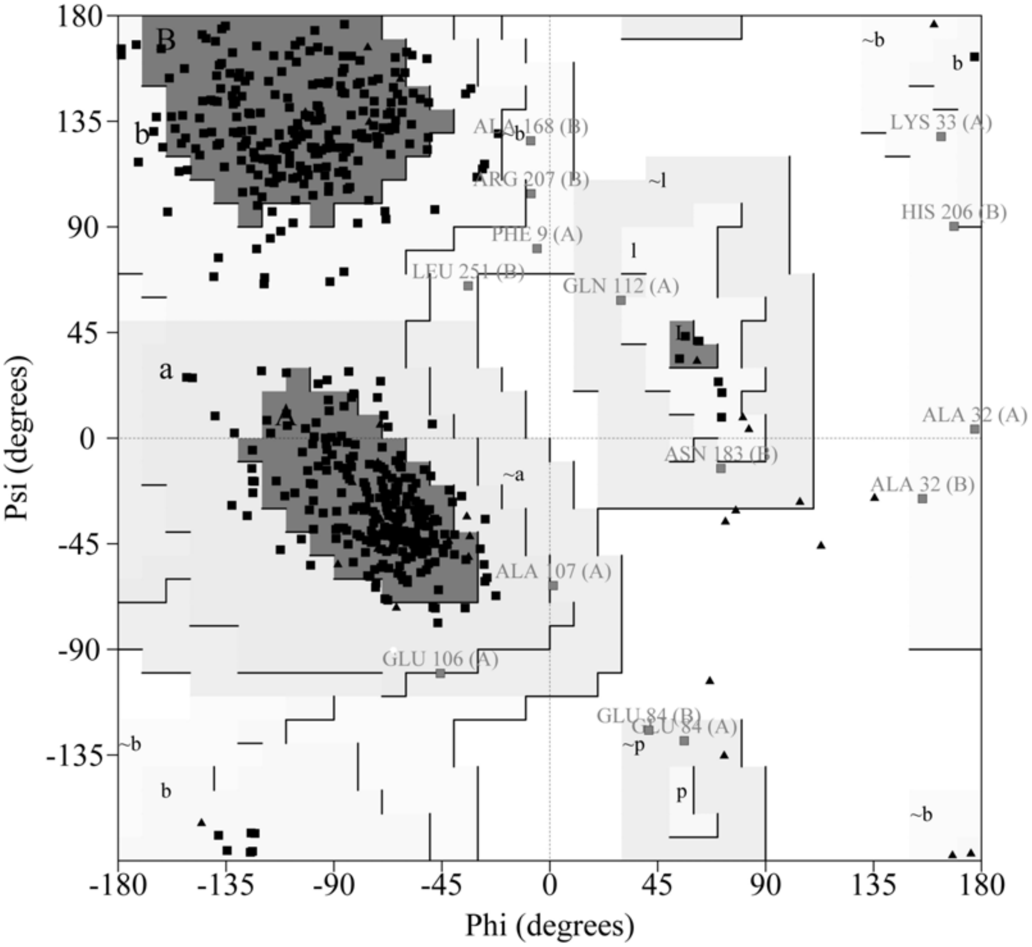

Figure 2.4: The Ramachandran plot of the hDDAH-1●ebselen structure

Chapter 3: Results and Discussion

Structure of the hDDAH-1●L-IPnO Complex

The structure of the DDAH-1●IPnO complex was solved to 2.9Å resolution. The enzyme inhibitor complex crystallized in the primitive monoclinic space group $P2_1$ with cell constants a = 47.21Å, b = 80.90Å, c = 74.09Å, α = 90, β = 90.13, γ = 90 and 2 DDAH-1 molecules in the asymmetric unit (Table 3.1). The V_m of the enzyme●inhibitor complex is 2.3$Å^3$ /Dalton. Residues 1-7 and 282-285 were not observed in the electron density maps and are believed to be flexible parts of the protein. Additionally, electron density was not observed for residues 32 and 33, which form part of the flexible loop that closes over the active site, and hence these were not built into the model.

The initial round of model building and refinement was carried out without the L-IPnO inhibitor; this minimizes phase bias while the model is still unrefined. As was the case with L-IPO inhibition, the initial difference maps revealed density extending from the γS atom of Cys273 to the ζC of the guanidinium moiety of L-IPnO (Figure 3.2). Because very strong, continuous difference density was observed between these two atoms the enzyme inhibitor complex was built as a covalent adduct.

It is important to note that covalent attack by the γS nucleophile of Cys273 generates a stereocenter at the ζC of L-IPnO. Because of the modest resolution limits of the structure, both R and S configurations of the DDAH-1●L-IPnO structure can be modeled into the electron density. However, the density for the covalent bond, and the amino acid portion of the inhibitor were clear and unambiguous (Figure 3.2). The other groups bonded to the ζC atom are the alkane group and the guanidinium group. Steric constraints and electrostatic interactions made this assignment very straightforward. In particular, the R conformation puts both of the inhibitor's guanidino NH groups in a favorable hydrogen bonding position with Asp78 (Figure 3.4). Furthermore, the homologous enzyme●inhibitor structure between DDAH and L-IPO was built in the R configuration using much higher resolution data that clearly shows the position of the $-NH_2$ and $-CH_2CH_3$ groups in addition to chemical evidence implicating this configuration (Figure 3.3).

Table 3.1: Crystallographic Data for the hDDAH-1●L-IPnO Complex

	hDDAH-1●L-IPnO
Space group	$P2_1$
Cell constants	a = 47.21Å, b = 80.9Å, c = 74.09Å, β = 90.13°
Resolution (Å) (outer shell)	20 – 2.9 (2.90-2.95)
R_{merge} (%) (outer shell)	.113 (.338)
$<I/\sigma_I>$ (outer shell)	12.2 (5.1)
Completeness (%) (outer shell)	95.4 (100.0)
Unique reflections	11935
Redundancy	3.4
# of residues	548
# of protein atoms	4184
# of ligand atoms	30
# of solvent atoms	--
$R_{working}$	0.2153
R_{free}	0.3154
Average B factor for protein atoms ($Å^2$)	36.42
Average B factor for ligand atoms ($Å^2$)	37.48
Average B factor for solvent atoms ($Å^2$)	--

rms deviation from ideality bonds (Å) angles (º)	 0.010 1.442
Ramachandran plot	
% of residues in most favored region	86.3
% of residues in additional allowed region	12.7
% of residues in generously allowed region	1.0

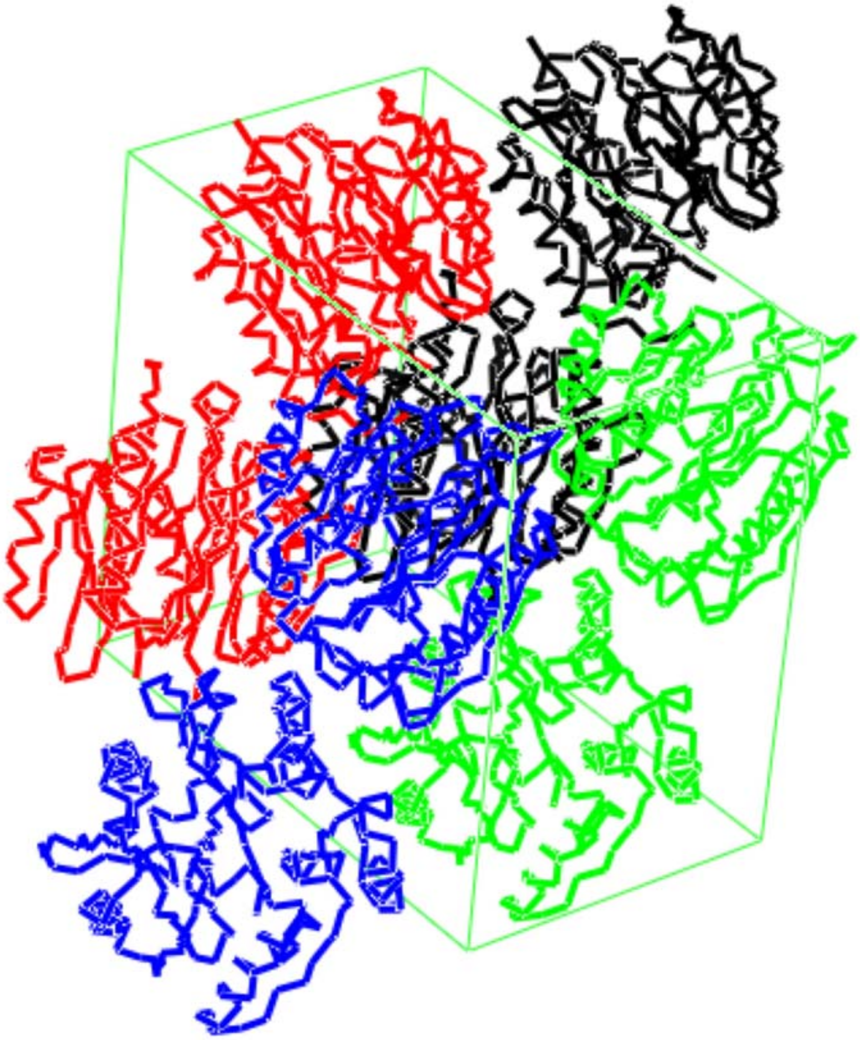

Figure 3.1: Crystal packing of the hDDAH-1●L-IPnO complex. The enzyme●inhibitor complex crystallized in the $P2_1$ space group (the green box represents the unit cell dimensions). Four hDDAH-1 dimers (red, black, blue, and green) are shown.

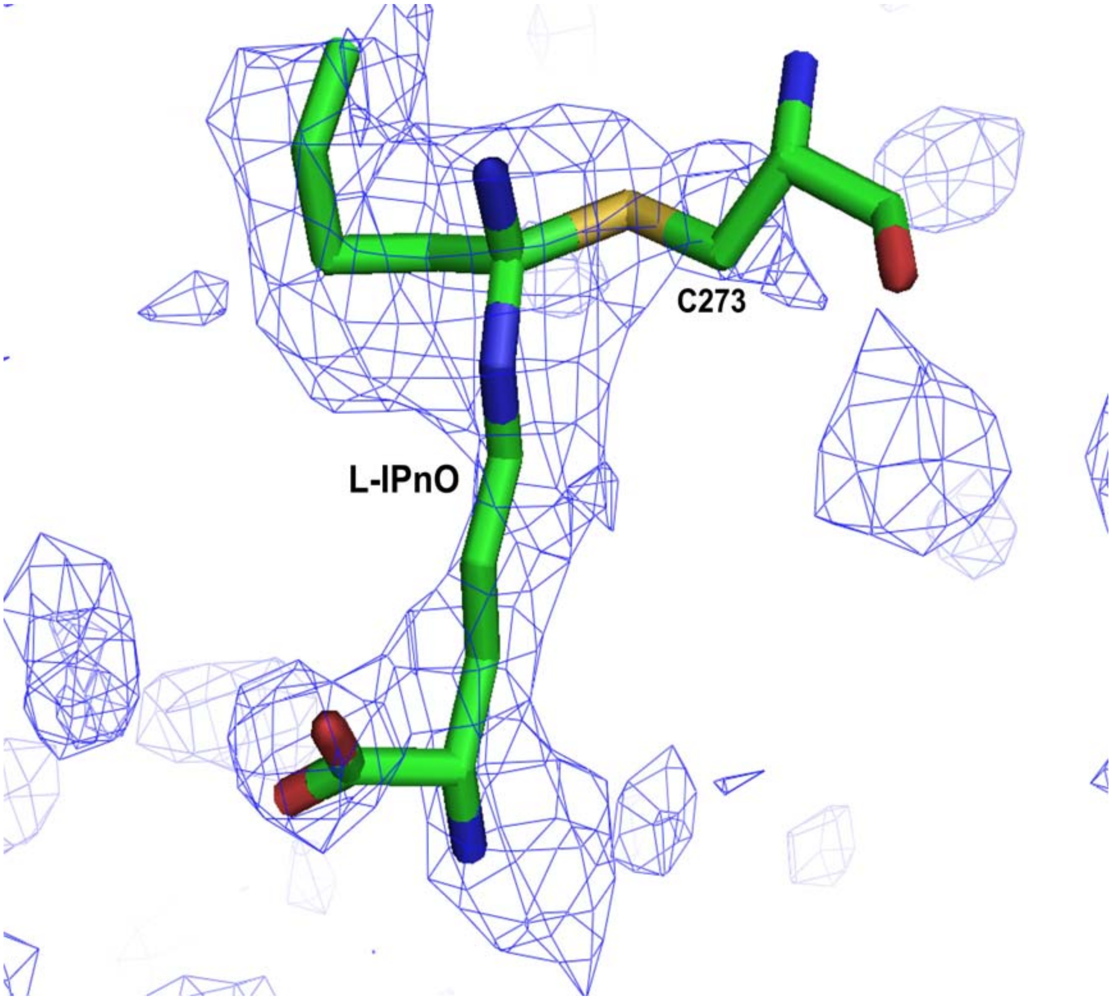

Figure 3.2: The Fo-Fc difference map at a 2σ contour level for the hDDAH-1●L-IPnO complex.

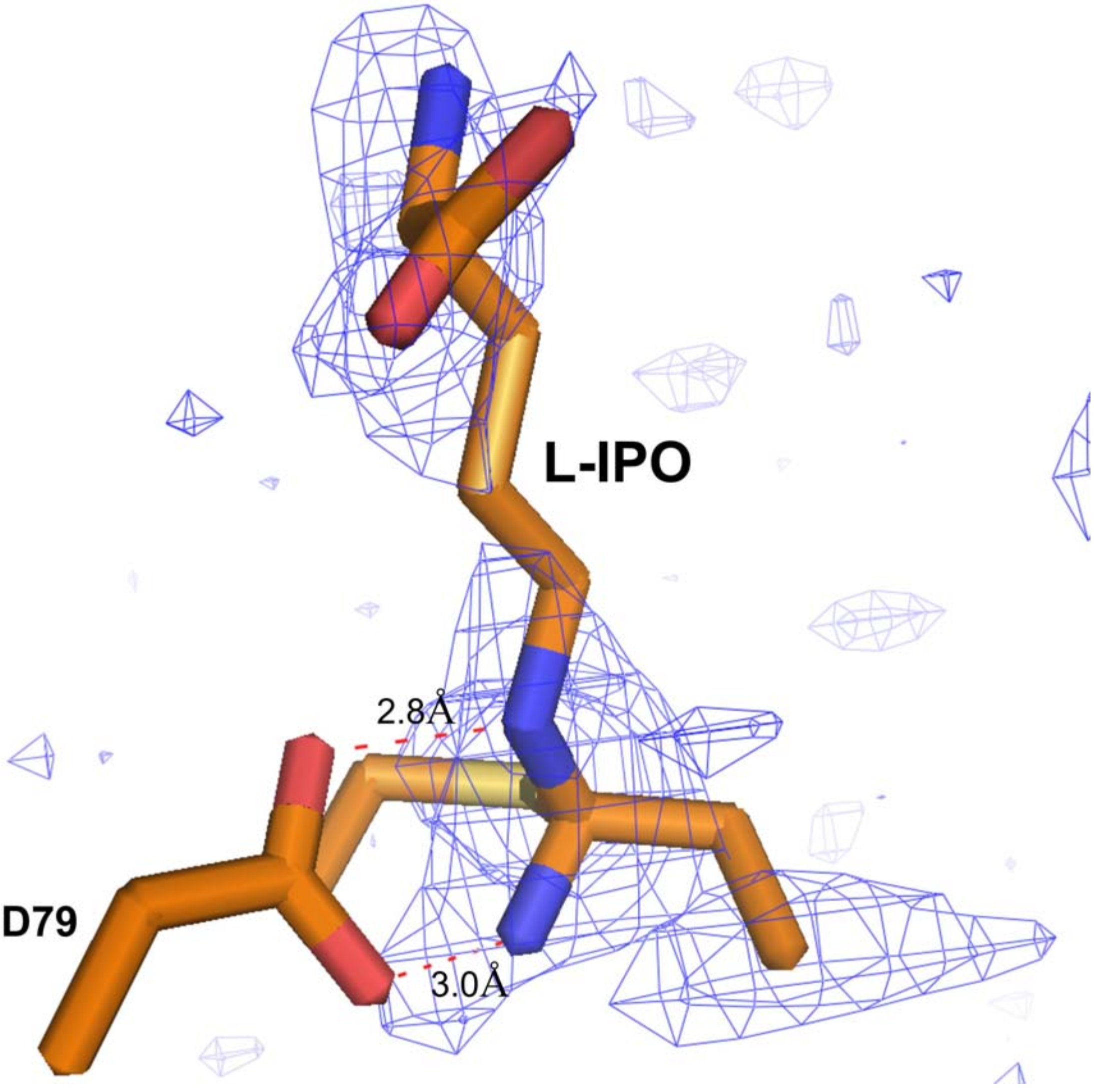

Figure 3.3: The Fo-Fc electron density map for the hDDAH-1●L-IPO complex. The electron density clearly shows the ζC atom of the inhibitor in R orientation with the ε and ω amine groups hydrogen bonded to the carboxylate side chain of D79. This figure was made at a 3σ level contour (Note: the numbering of the residues for the hDDAH-1●L-IPO complex is advanced by one, i.e. D79 in this complex is equivalent to D78 in the hDDAH-1●L-IPnO complex).

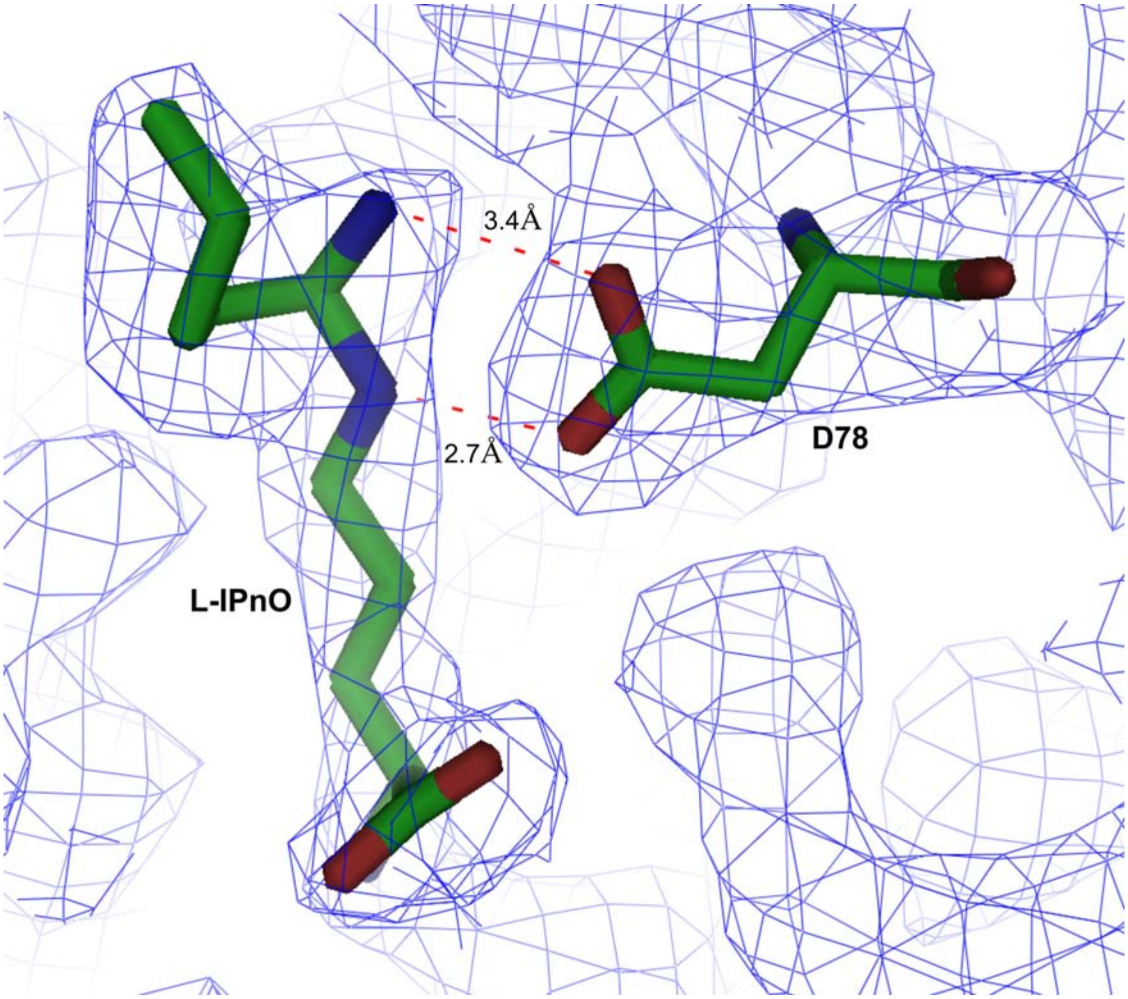

Figure 3.4: Stereochemical orientation of L-IPnO. The 2Fo – Fc map at a 1σ contour showing the carboxylate side chain of Asp78 hydrogen bonding to the HNε and HNω amine groups of L-IPnO's guanidinium moiety.

In addition to the covalent bond to Cys273 and the hydrogen bonding with Asp78, the L-IPnO inhibitor is also docked into the active site via hydrogen bond contacts with Arg144, Arg97, Glu77, Asp72, Leu29, and Val267 (Figure 3.5). Glu77 ion pairs with Lys174 to form the "bottom" of the active site, and also hydrogen bonds with L-IPnO's primary amine group. The guanidino groups of the Arg144 and Arg97 side chains make hydrogen bond contacts with the α-carboxylic acid group, whereas the side chain of Asp72 makes a salt bridge with L-IPnO's α-amino group. The main chain carbonyls of both Leu29 and Val267 make hydrogen bond contacts with L-IPnO's α-amino group. The Leu29 contact is of particular note since this residue represents the snap closure of the active site "lid" formed by amino acids 25-38, with the Leu29 side chain covering the active site channel. The β and γ methylene groups of L-IPnO are flanked on one side by the aromatic side chain of Phe75 (Figure 3.6). As expected the loop formed by amino acids 25-38 is in the closed conformation in this structure, as has been observed for DDAH-1 in complex with other ligands including L-citrulline, L-homocysteine, and S-nitroso-L-homocysteine, and the hydrogen bond contacts and other interactions used for docking L-IPnO are identical to those used for docking L-IPO and L-citrulline.

At the dimer interface, crystal packing interactions are made by hydrogen bonding between Glu36 of one molecule and Arg98 of another and Ser96 of one molecule and Asp38 of another (Figure 3.7). Furthermore, hydrophobic packing between the side chain of Leu29 and Ala40 also occurs at the crystal packing interface. As one would predict from the structural similarity, the hDDAH-1●L-IPO and hDDAH-1●L-IPnO are virtually identical with an rms distance for all atoms of 0.40 Å. In both crystal structures, the α-carboxylate group of the inhibitor is hydrogen bonded to the guanidinium side chain of Arg144 while the α-amino group is docked by the main chain carbonyls of Leu29 and Val267 along with the side chain of Asp72. Both L-IPO and L-IPnO's methylene carbons are flanked on one side by the aliphatic side chain of Phe75, and the guanidino amine groups of both inhibitors form a salt bridge with Glu77 and Asp78. The similarity of these interactions would be expected since the two inhibitors differ only in the length of their alkyl side chains. L-IPnO was shown to be a 7-fold stronger inhibitor than L-IPO, however, the only structural basis that supports this kinetic data is that L-IPnO's pentyl alkyl chain may make stronger interactions with the side chain of L270 than L-IPO's propyl alkyl chain (Figure 3.6).

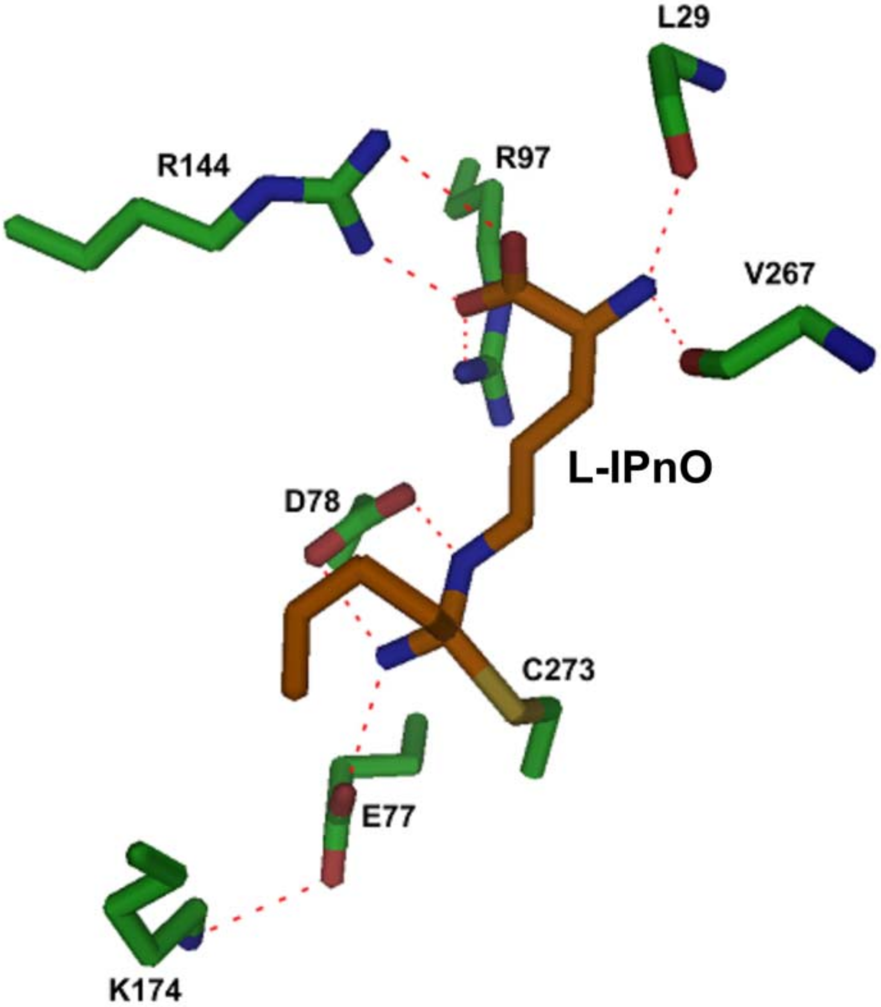

Figure 3.5: The hydrogen bonding network of the hDDAH-1●L-IPnO complex. The amino acid portion of the compound is anchored by hydrogen bonds to the side chains of R97 and R144 along with the main chain carbonyls of L29 and V267. The ζC atom of the guanidinium moiety is covalently linked to C273 and the HNε and HNω groups are hydrogen bonded to E77 and D78.

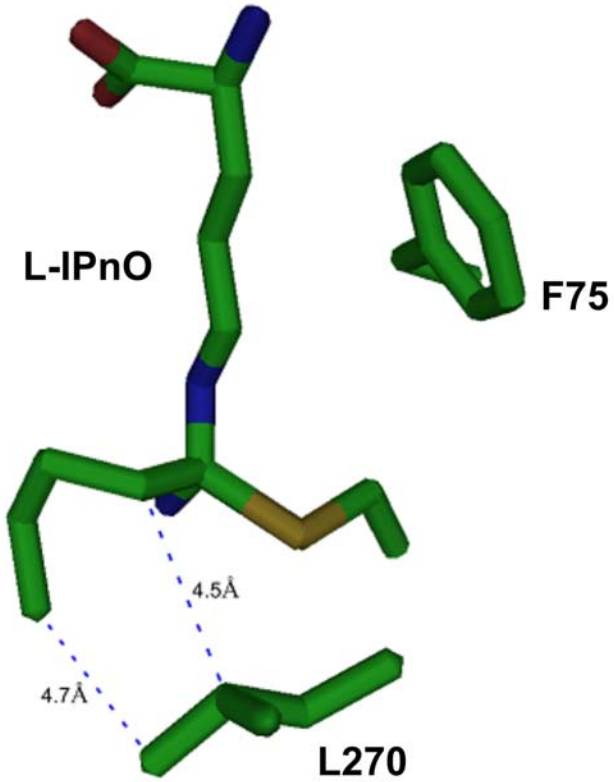

Figure 3.6: Hydrophobic interactions in the hDDAH-1●L-IPnO complex. The aromatic ring of F75 stacks onto the β and γ methylene groups of L-IPnO. The side chain of L270 interacts with IPnO's pentyl chain.

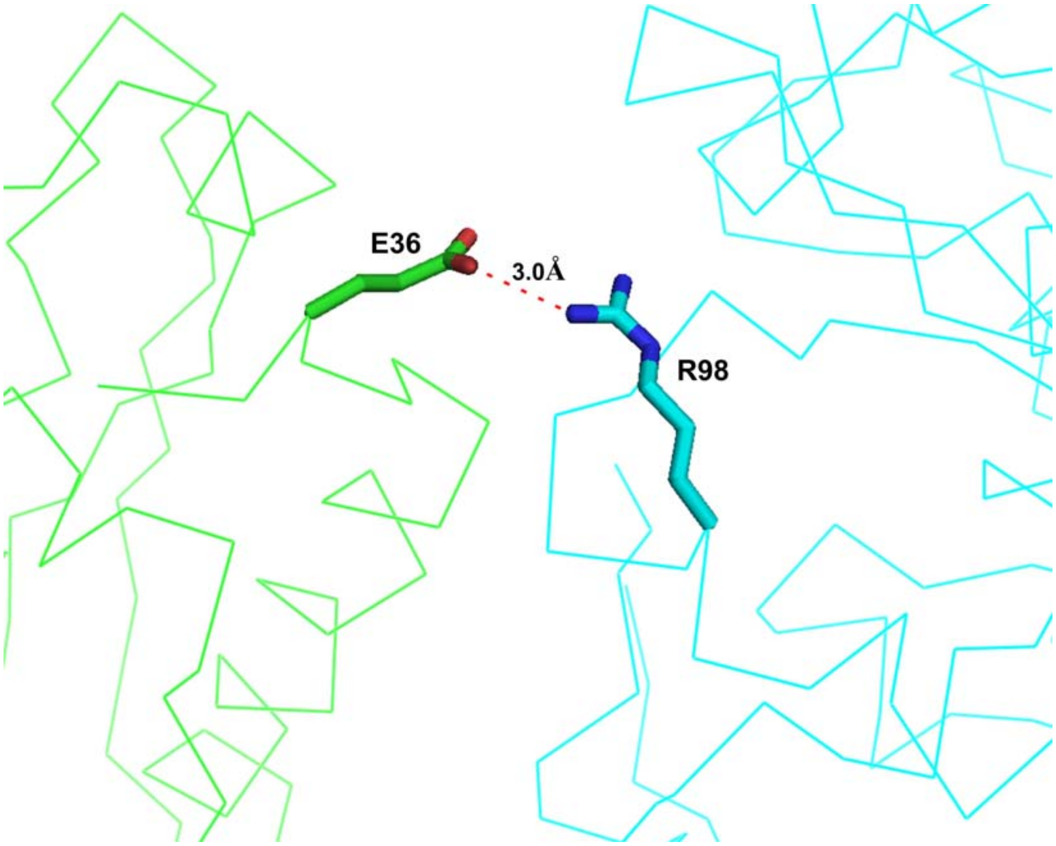

Figure 3.7: Intermonomer interactions in the hDDAH-1●L-IPnO complex. A salt bridge at the dimer interface of the hDDAH-1●L-IPnO complex between E36 of one hDDAH-1 monomer of the asymmetric unit (green) and R98 of the other (blue).

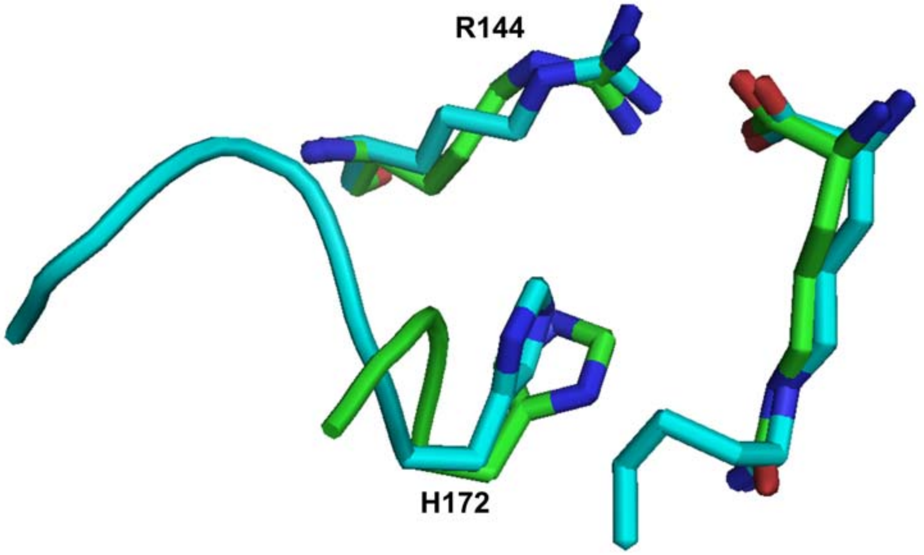

Figure 3.8: A superimposition of hDDAH-1●L-citrulline (green) and hDDAH-1●L-IPnO (blue). Similar to the L-IPO structure, the loop preceding H172 in the L-IPnO structure, consisting of residues ^{169}ADGL^{172} is ordered in its structure and disordered when L-citrulline is bound. As was the case with L-257, H172 is positioned further away from the L-IPnO ligand than the L-citrulline ligand.

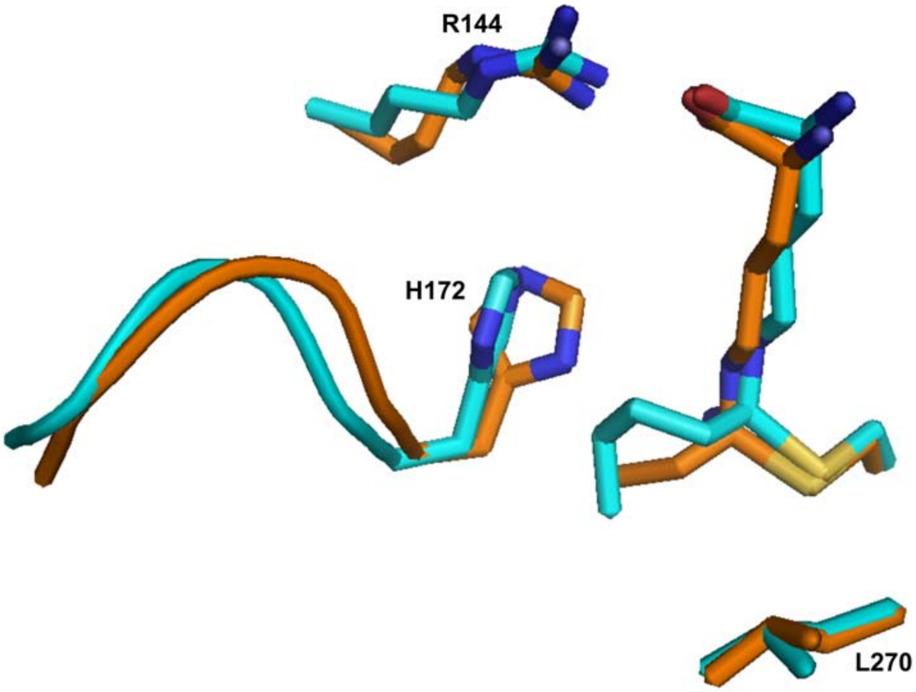

Figure 3.9: A superimposition of hDDAH-1●L-IPO (orange) and hDDAH-1●L-IPnO (blue). The main difference between the two structures is the positioning of the H172 side chain, which is in closer proximity to the ligand in the L-IPO structure than in the L-IPnO structure.

Structure of the hDDAH-1●ebselen Complex

The structure of the hDDAH-1●ebselen complex was solved to 2.0Å resolution. The hDDAH-1●ebselen complex crystallized in the primitive monoclinic space group $P2_1$ with cell constants a = 47.501Å, b = 81.05Å, c= 74.013Å, α= 90.00, β = 90.11, and γ = 90.00 (Table 3.2). The structure has 2 molecules in the asymmetric unit and a V_m = 2.3Å/dalton. The initial difference maps only showed a small, albeit dense, blob of electron density around Cys273 (Figure 3.11). This led to an analysis of the problem that ultimately revealed the crystal exhibited pseudomerohedral twinning. The program suite PHENIX is able to refine the twinning parameters, which showed a 73%- 27% ratio.

After detwinning the diffraction data and several rounds of refinement using PHENIX, the density for the inhibitor became visible (Figure 3.12). The major point is that strong density is seen running continuously from the γS of Cys 273, to the selenium atom of ebselen, suggesting that a covalent bond has been formed between these two atoms (Figure 3.12). This enzyme-inhibitor complex also has the flexible loop made up of residues 25-38 in the closed conformation (Figure 3.13). This flap closure is a particularly interesting observation since ebselen lacks an α-amino group to which L29 can hydrogen bond to and "latch" the active site shut. The isobutyl groups of Leu29 and L270 and the aromatic ring of Phe75 act to hydrophobicly stack onto both of ebselen's phenyl rings (Figure 3.14). Crystal packing interactions at the hDDAH-1●ebselen dimer interface include hydrogen bonding between Glu36 of one molecule, a water molecule, and Arg98 of another molecule (figure 3.15). Other crystal packing interactions include hydrogen bonding between Asp38 and Ser96.

Because Fast and coworkers were the first to study the inhibition of hDDAH-1 by ebselen, some important details of the inhibition were unknown. Specifically, it had not been determined whether the compound inhibited hDDAH-1 by attacking Cys273 or His172. Covalent modification of C273 has been observed with several compounds including L-IPO and L-IPnO. However, inhibition by attack of His172 was also observed with the inhibitor, 4-hydroxynonenal (4-HNE). From the hDDAH-1●ebselen electron density maps it is clear that ebselen's mode of inhibition is covalent attachment to C273 via a selenyl-sulfide bond (Figure 3.16).

Table 3.2: Crystallographic Data for the hDDAH-1●ebselen Complex

	hDDAH-1●ebselen
Space group	$P2_1$
Cell constants	a = 47.501Å, b = 81.05Å, c = 74.013Å, β = 90.11°
Resolution (Å) (outer shell)	20-2.0 (2.07-2.11)
R_{merge} (%) (outer shell)	.076 (0.418)
$\langle I/\sigma_I \rangle$ (outer shell)	10.3 (4.5)
Completeness (%) (outer shell)	96.9 (99.2)
Unique reflections	33141
Redundancy	3.6
# of residues	548
# of protein atoms	4184
# of ligand atoms	32
# of solvent atoms	230
$R_{working}$	.1804
R_{free}	.2871
Average B factor for protein atoms ($Å^2$)	37.65
Average B factor for ligand atoms ($Å^2$)	45.93
Average B factor for solvent atoms ($Å^2$)	33.34

rms deviation from ideality	
bonds (Å)	0.035
angles (º)	3.176
Ramachandran plot	
% of residues in most favored region	81.3
% of residues in additional allowed region	15.8
% of residues in generously allowed region	2.9

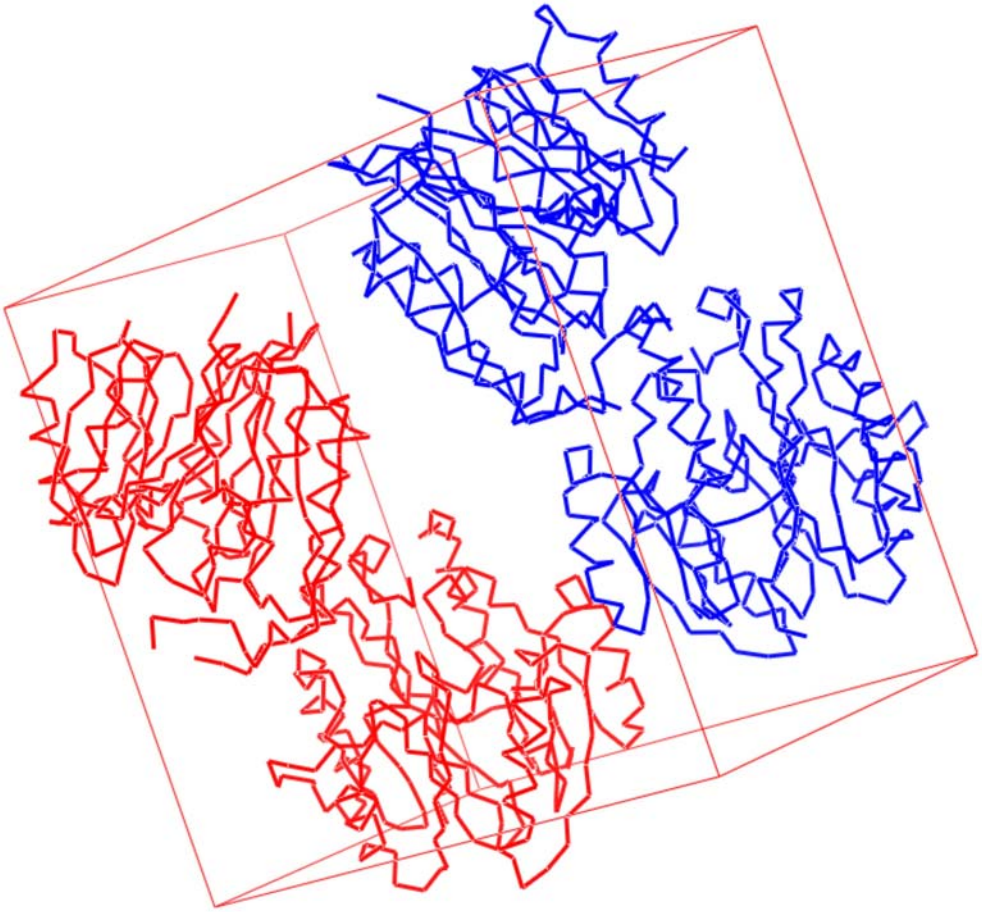

Figure 3.10: Crystal packing of the hDDAH-1●ebselen complex. The hDDAH-1●ebselen complex crystallized in the $P2_1$ space group. The unit cell dimensions are represented as a red box. Two hDDAH-1 dimers (red and blue) are shown.

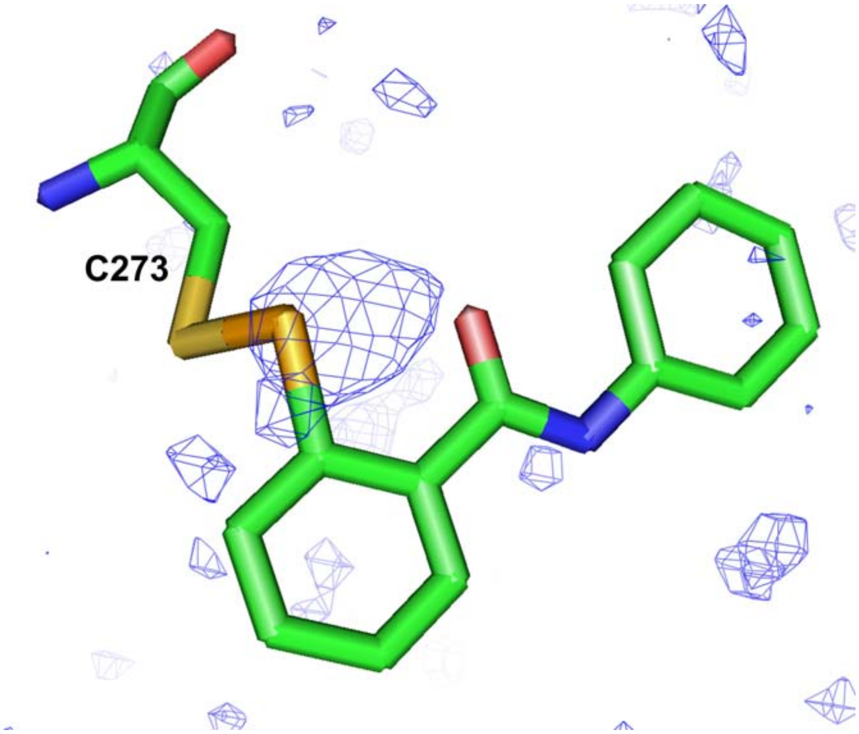

Figure 3.11: The Fo-Fc difference map for the hDDAH-1●ebselen complex. The Fo – Fc map at a 3σ contour showing strong electron density extending from the γS of C273, indicating the presence of a covalent bond with ebselen's selenium atom.

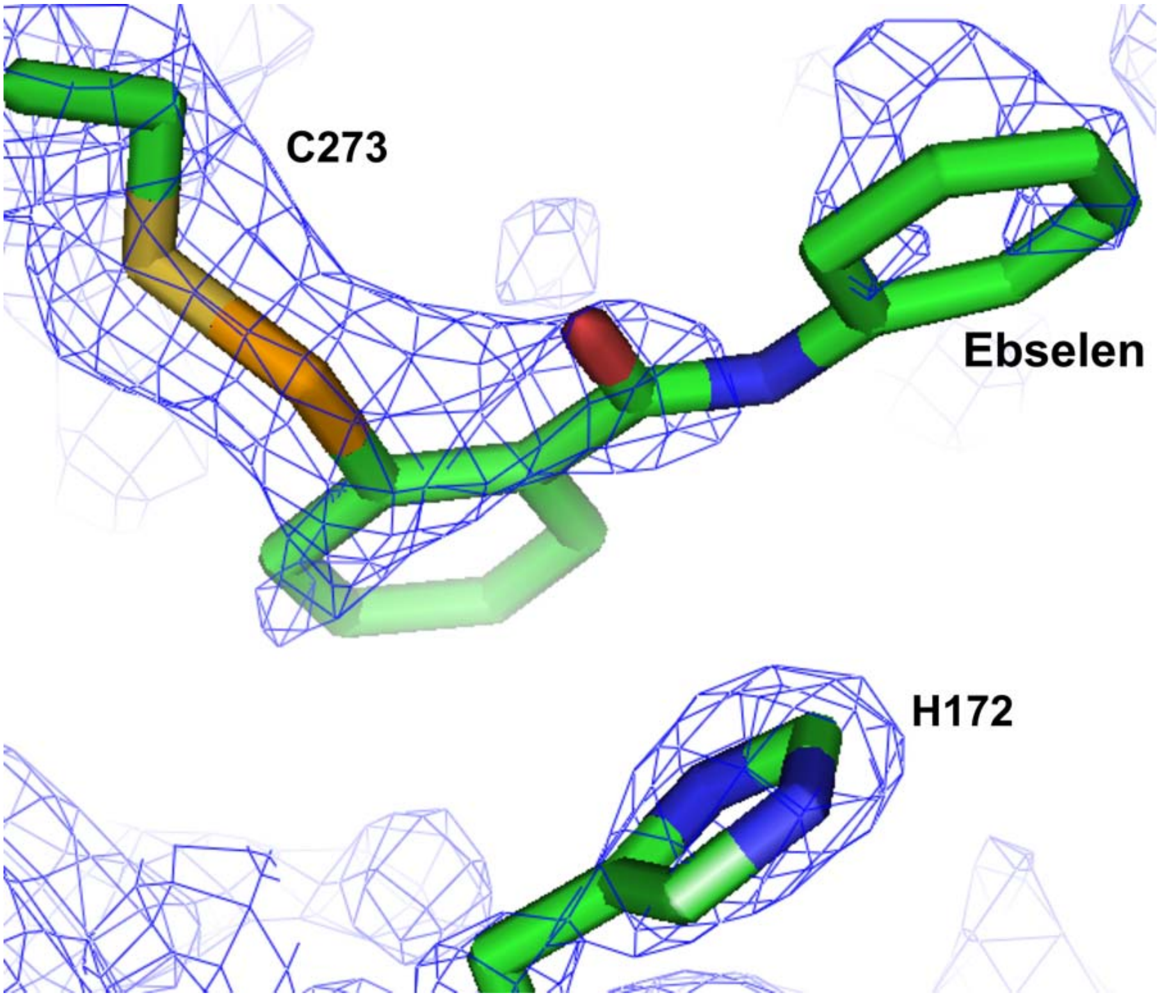

Figure 3.12: The hDDAH-1●ebselen electron density map. The 2Fo-Fc map at 1.5σ showing electron density extending from the γS atom of C273 to the selenium atom of ebselen.

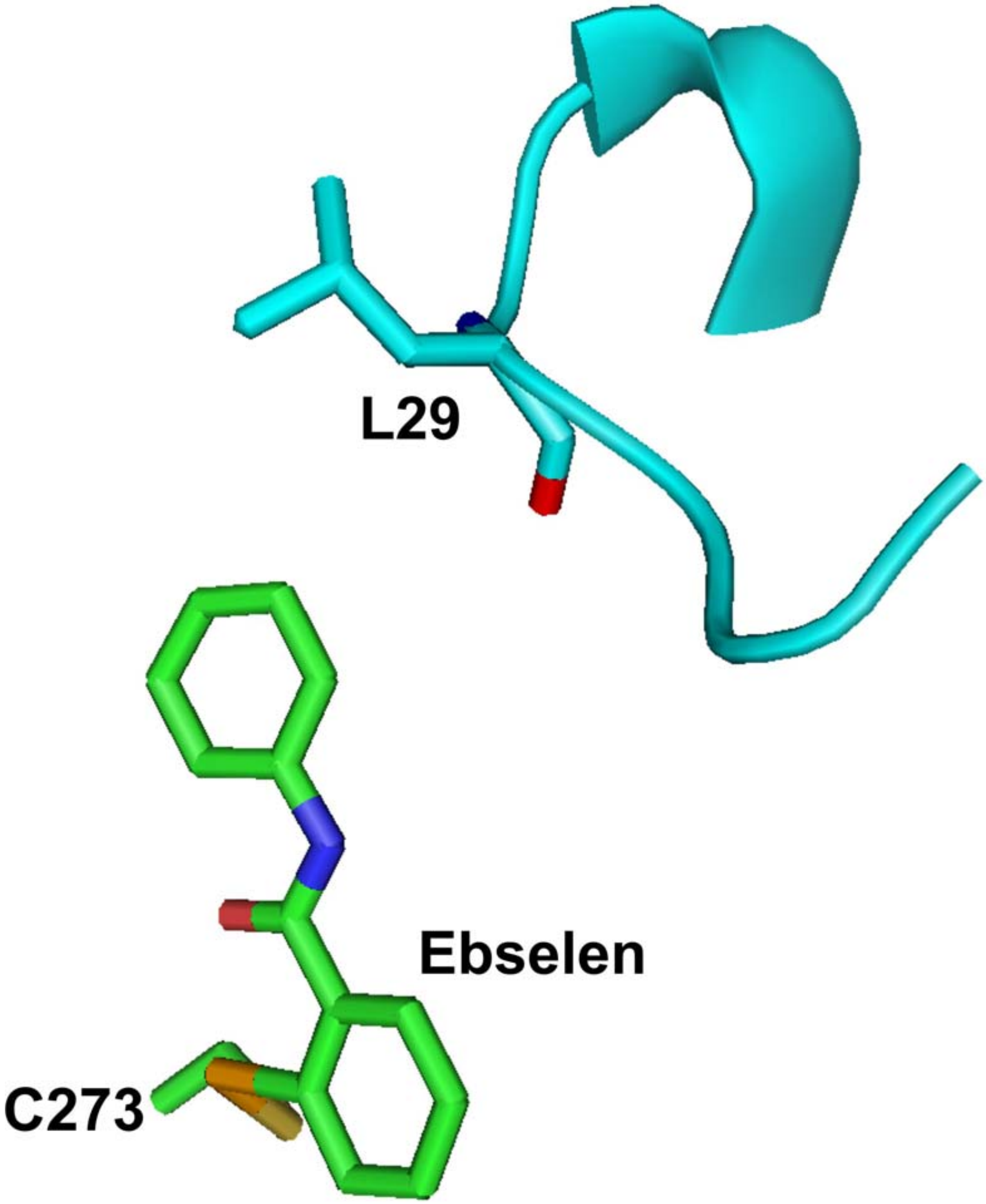

Figure 3.13: Loop closure in the hDDAH-1●ebselen complex. The flexible loop made up of residues 25-38 folds over the active site. However, the main chain carbonyl of L29 does not have a hydrogen bonding partner, as was the case with the L-arginine analog inhibitors.

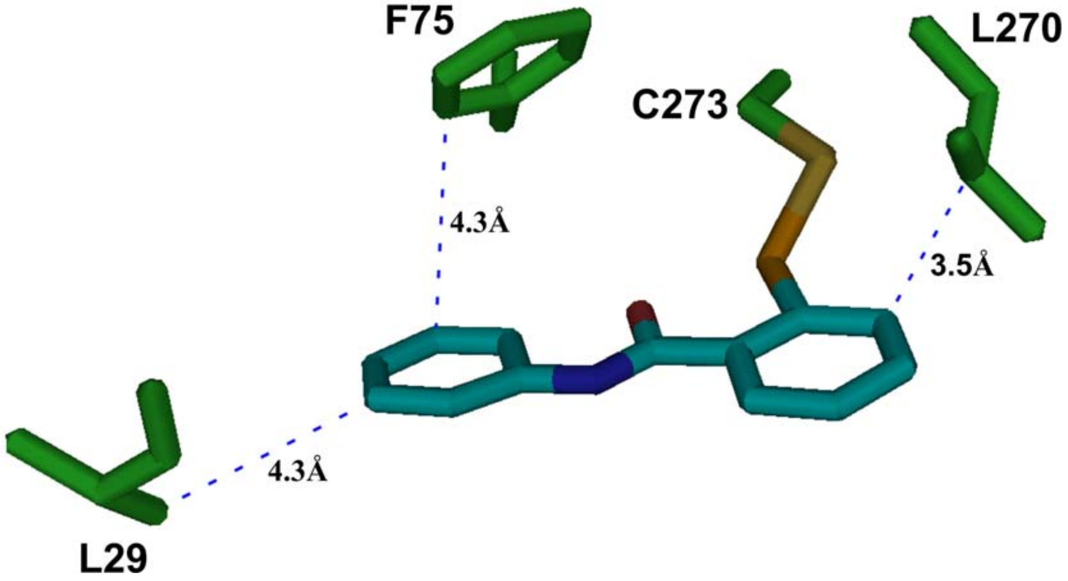

Figure 3.14: Hydrophobic interactions at the active site of the hDDAH-1●ebselen complex. The side chains of L29, F75, and L270 are involved in hydrophobic stacking interactions with both of ebselen's aromatic rings.

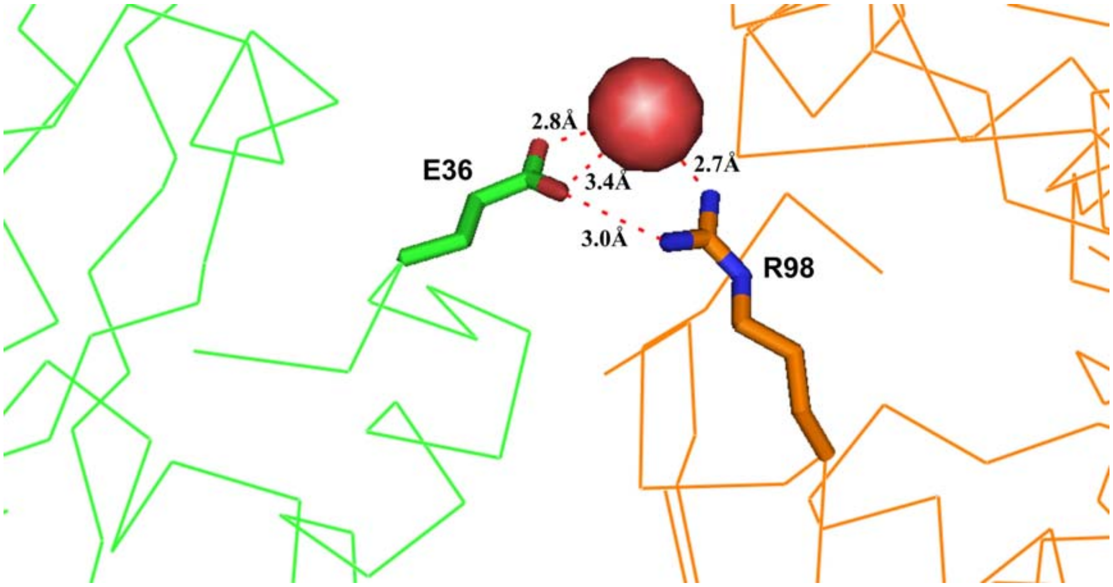

Figure 3.15: A hydrogen bonding network at the dimer interface of the hDDAH-1●ebselen structure. E36 of one chain (green) hydrogen bonds with a water molecule (red sphere) and R98 (orange) of another chain.

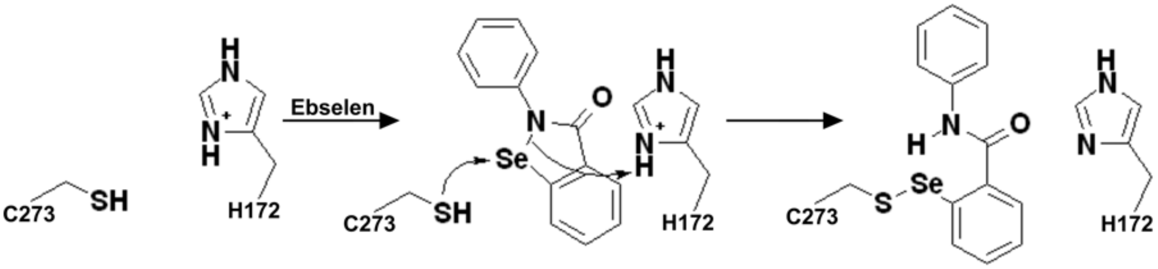

Figure 3.16: Inhibition of DDAH-1 by ebselen. Ebselen's selenium atom reacts with the γS atom of C273 of DDAH-1 to form an irreversible covalent adduct.

Ebselen has a completely different structure from the arginine analogs that have previously been crystallized with hDDAH-1. In stark contrast to these ligands, the binding of ebselen almost exclusively involves covalent attachment to the active site cysteine. However, for the most part, the positioning of the active site residues in the four hDDAH-1●ligand structures is the same, with the exception of H172, the loop preceding it, and R144. With respect to these residues, the binding of ebselen to hDDAH-1 is quite different from the L-citrulline model (Figure 3.17). R144, which ion pairs with the α-carboxylate group of L-citrulline, is facing away from the from the ebselen ligand. Additionally, the backbone atoms of the loop preceding H172, deviate significantly (rms of 1.6 Å for ^{170}GLH^{172}) between these two structures. Finally, when compared to the L-citrulline structure, the side chain of H172 has tilted away from the active site when ebselen docks. Interestingly, the side chain of R144 in the L-257 structure was also observed to be facing away from the active site and not involved in docking of the ligand (Figure 3.18). Furthermore, the loop consisting of residues ^{168}ADGLH^{172} adopts a very similar conformation between the two structures (rms of 0.5 Å).

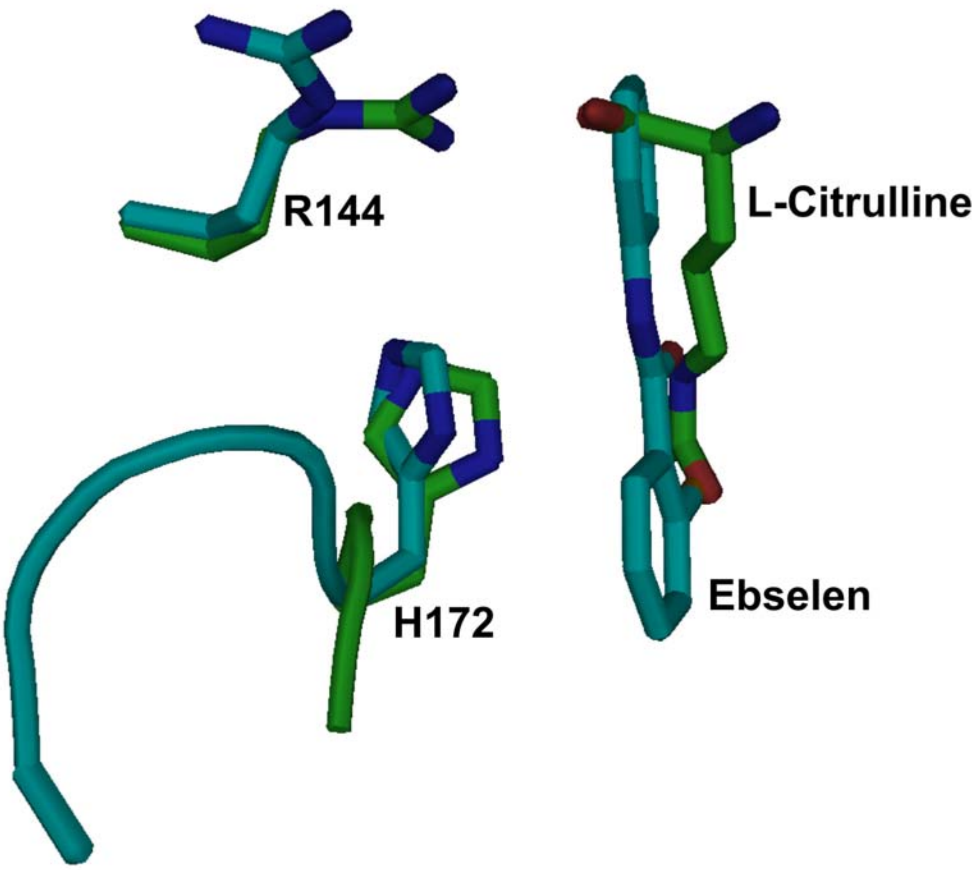

Figure 3.17: hDDAH-1●ebselen aligned with hDDAH-1●L-citrulline. A superimposition of the L-citrulline (green) and ebselen (blue) structures. In contrast to the L-citrulline structure, the side chain of R144 points away from the active site in the ebselen structure. Additionally, H172 has tilted away from the active site in the ebselen structure.

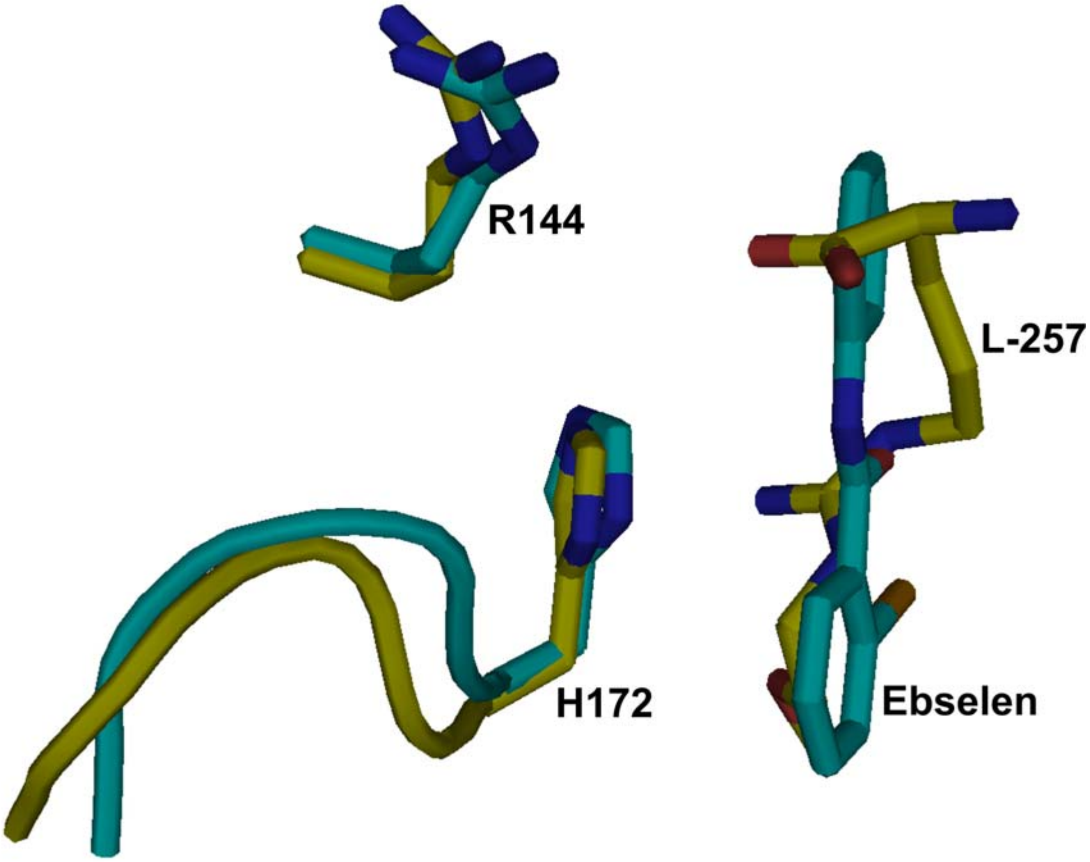

Figure 3.18: hDDAH-1●ebselen aligned with hDDAH-1●L-257. A superimposition of the L-257 (yellow) and ebselen (blue) structures. The docking of these two structures is similar. In both cases the side chain of R144 points away from the active site and H172 and the ^{168}ADLGH^{172} loop are in very similar orientations (rms = 0.5 Å).

Chapter 4: Conclusion

In this study, the crystal structures of hDDAH-1 complexed with L-IPnO and ebselen were solved to 2.9 Å and 2.0 Å resolution, respectively. The L-IPnO inhibitor was shown to dock in essentially the same manner as the inhibitors L-IPO and L-257. This mode of docking, involves the closure of the flexible loop over the active site, hydrogen bond and ion pair interactions, hydrophobic interactions, and a covalent linkage between the ζC atom of the inhibitor and the γS atom of C273. The L-IPnO structure did show some differences from these other two structures at the active site, specifically, the positioning of H172 with respect to the bound ligand. L-IPnO was shown to be a more potent inhibitor than L-IPO and from the structural data presented here it can be concluded that this is most likely due to a more favorable hydrophobic interaction between the pentyl group of L-IPnO and the side chain of L270.

The ebselen inhibitor was shown to bind to the enzyme almost exclusively by a covalent linkage between the inhibitor's selenium atom and the γS of C273, with flap closure also occurring. This crystal structure clearly showed that ebselen's mode of inhibition is attack of C273, not H172. Furthermore, although ebselen belongs to a completely different class of compounds than the L-arginine analog L-257, the binding of this compound to hDDAH-1 with respect to the conformation of R144 and the ^{168}ADLGH^{172} loop was found to be similar.

Chapter 5: Future Work

Ebselen is the first seleno compound shown to inhibit hDDAH-1. It is also the most potent inhibitor of this enzyme to date, with a reported IC_{50} of 300nM. In addition to further expansion of the amidine scaffold, future work should concentrate on seleno compounds like ebselen as a promising scaffold for the design of potential inhibitors for hDDAH-1.

Chapter 6: Introduction

Messenger RNA Trafficking in Neurons

Cellular trafficking of mRNAs and localized protein expression are mechanisms by which cells spatially and temporally control gene expression [36]. By dictating when and where protein encoding mRNAs are translated in the cell, functionally distinct cellular compartments and structures can be established. To perform this task, the cell must be able to transport localized mRNAs in a translationally dormant state and also be able to activate translation of the message once it has reached it's destination. This task is accomplished by the cell's use of RNA binding proteins that target cis-regulatory sequences in the localized mRNA. These trans-acting factors bind to their target mRNAs, forming a translationally dormant ribonucleoprotein complex that can interact with cytoskeletal motor proteins for transport to its subcellular destination (Figure 6.1) [37]. Once the mRNA cargo has been delivered, the translational repressor is inactivated and the message is released. Neuronal cells are a paradigm for mRNA localization and spatial control of protein synthesis. It has been observed that differentiated neurons stockpile mRNAs in their dendritic branches (Figure 6.2) [36]. By storing mRNAs in this manner, neurons can conduct localized translation of any subset of these mRNAs as a response to synaptic transmissions, a property that grants these cells their trademark plasticity [36].

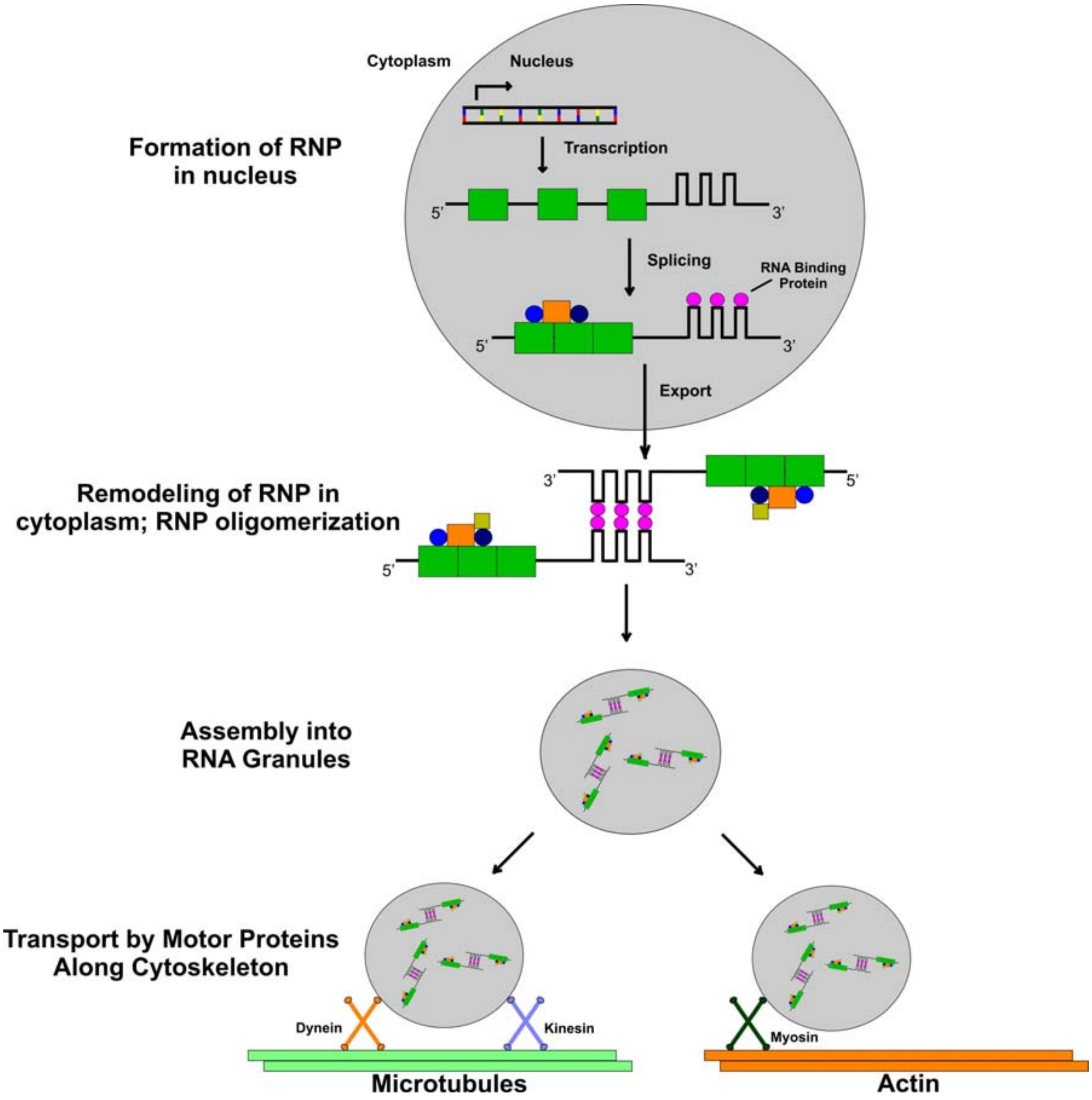

Figure 6.1: RNA trafficking in neuronal cells. In the nucleus, RNA binding proteins target localized mRNAs through recognition of cis-elements in the 3' UTR. These mRNAs are then exported to the cytosol and organized into translationally dormant ribonucleoprotein particles. These RNPs are then transported by motor proteins along the cytoskeleton until reaching their destination. This figure was adapted from [37].

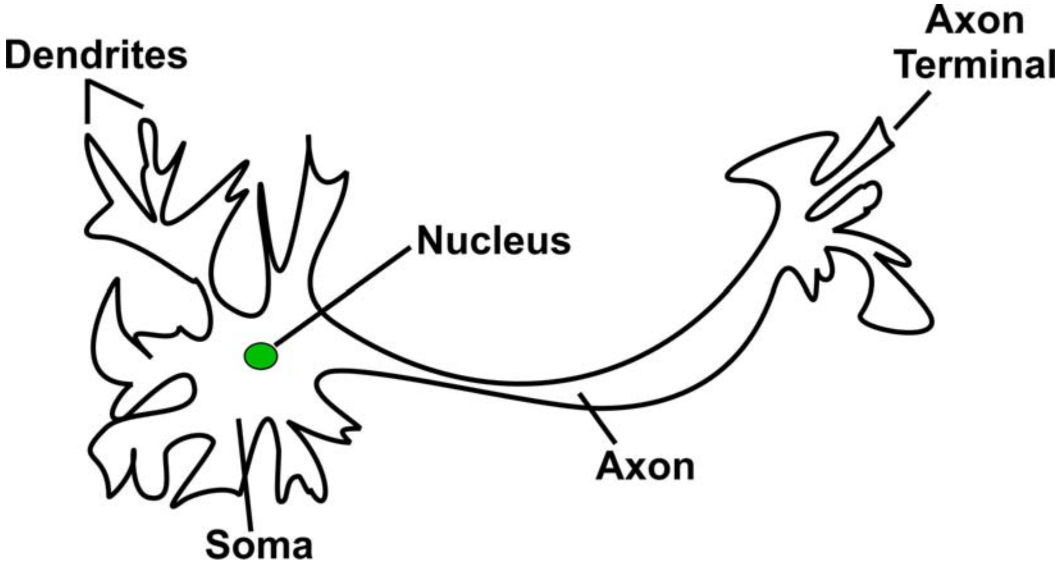

Figure 6.2: A cartoon representation of a neuronal cell. Electrochemical messages received from other neurons reach the soma, or central body, of the neuron via the synaptic junctions of the dendritic branches. The axon of the neuron acts to send electrochemical messages away from the soma and out to other neurons. It is known that neurons stockpile translationally dormant mRNAs, in the form of RNPs, in their dendritic branches. This allows for specific, localized protein as a response to neuronal stimulation [36].

mRNA Sorting During Spermatogenesis

Mammalian male germ cell differentiation is another cellular process that employs post-transcriptional control to determine when and where gene expression occurs in the cell. Spermatogenesis is the cellular process that transforms diploid testicular stem cells into mature spermatozoa [38]. In mammals, males are provided with a definitive number of testicular stem cells, estimated to be about 10,000, that provide fertility for the lifetime of the individual. The cells that comprise this stem cell population will undergo one of three fates (Figure 6.3). One subset of the population will undergo mitotic divisions to produce identical cells that replenish the cell line, whereas another subset will undergo apoptosis. A third subset of these testicular stem cells, which comprises the majority, enter a differentiative pathway to become mature spermatozoa. Spermatogenesis initiates with mitotic divisions followed by meiotic divisions to produce secondary spermatocytes [38]. These secondary spermatocytes then undergo several morphological changes during spermiogenesis to produce mature elongated spermatozoa. It is during spermiogenesis that the spermatocyte nucleus becomes transcriptionally silent due to the protein component of chromatin being exchanged twice; first histones are replaced by transition proteins and then transition proteins are replaced by testis specific proteins called protamines [38].

Because transcription terminates mid way through spermiogenesis, post-transcriptional regulation of protein expression takes on a particular prominent role during this stage of spermatogenesis [38]. Specifically, proteins needed in the final stages will have to be transcribed prior to termination of transcription and these messages will have to be stored and sequestered from the translation machinery until they are required. This mRNA sorting is accomplished by RNA binding proteins that target cis-elements in the message, binding to the mRNA and preventing translation until a certain timepoint in the process has been reached, at which point the message will be released, translated, and the protein utilized [38].

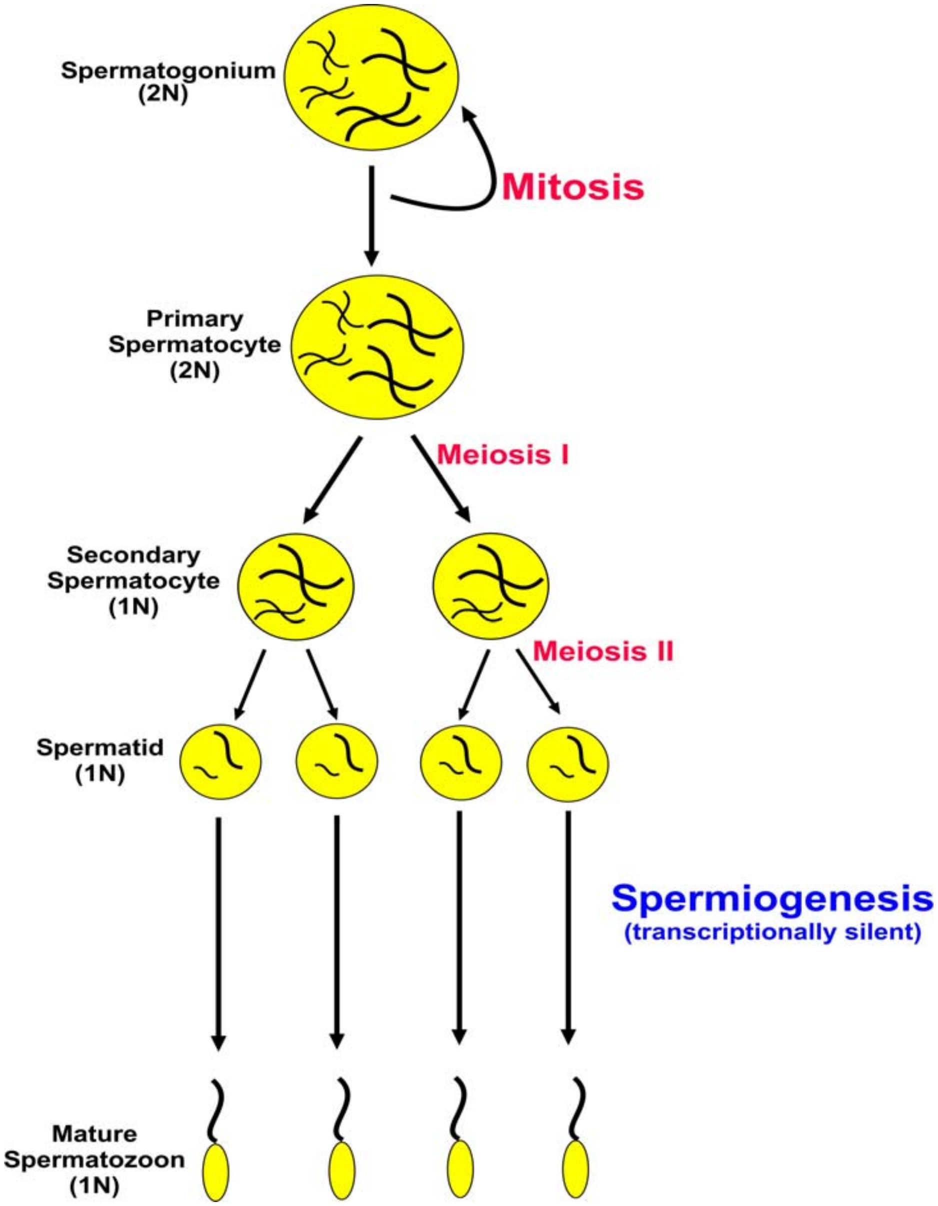

Figure 6.3: Mitotic and Meiotic divisions during spermatogenesis. Male germ cells destined to become spermatids undergo meiotic divisions to reduce ploidy and morphological transformations to complete the maturation process. The morphological changes (spermiogenesis) are carried out with a transcriptionally silent nucleus using proteins that were transcribed and stored at an earlier stage. This figure was adapted from [38].

Translin

Translin, a highly conserved mammalian protein enriched in the brain and testis, was originally discovered as a protein involved in chromosomal translocations associated with lymphoid malignancies [39]. Subsequent research by Hecht and coworkers on the spatial and temporal control of protein expression during spermatogenesis in mice identified a 26KDa trans element involved in maintaining translational dormancy on sets of testis specific mRNAs known as protamines [40]. This trans acting factor was named Testis Brain RNA Binding Protein (TB-RBP) and later proved to be the mouse ortholog of translin, differing at only 3 of the 228aa residues (99% identity) [40].

From the primary sequence, it was predicted that translin contained a nuclear export signal and a putative leucine zipper motif (Figure 6.4). Two sets of basic residues, amino acids 56-64 and 86-97, were identified as being involved in DNA and RNA recognition, and site-directed mutants in the 86-97 region were shown to abolish DNA binding activity completely. It was proposed that the physiological targets of translin are conserved sequences in the 3' UTR of protamine mRNAs designated Y and H elements (Figure 6.5) [41]. However, it has subsequently been demonstrated that Y and H elements are not requisite for RNA binding by translin, and in fact, translin has been shown to bind to several RNA and DNA sequences [42, 43]. Furthermore, since translin was subsequently shown to bind to DNA sequences not associated with translocation hotspots, its putative role in recombination has been called into question [43].

Translin has also been identified as a transporter of mRNAs in neurons and male germ cells; it therefore comes as no surprise that it requires partner proteins to accomplish this task. This is especially important in the testis where mRNA transport is required to maintain genetic equivalence between X and Y chromosome carrying sperm cells. Translin has been shown to interact with several different proteins including an ATPase, a kinesin family member, and a protein component of the cytoskeleton, and these interactions highlight its role in intra and intercellular transport of RNA cargoes [44, 45].

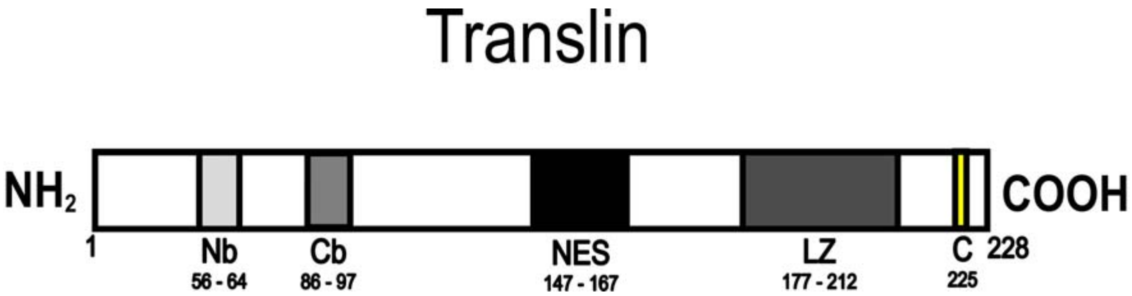

Figure 6.4: The domains of translin. Nb and Cb represent basic regions known to be involved in nucleic acid recognition with their relative positions in the sequence designated as being closer to the N-terminus or C-terminus, respectively. NES and LZ represent translin's nuclear localization signal and leucine zipper, respectively. C is Cys225, the presumed site of intramolecular disulfide bonds between translin monomers This figure was adapted from [46].

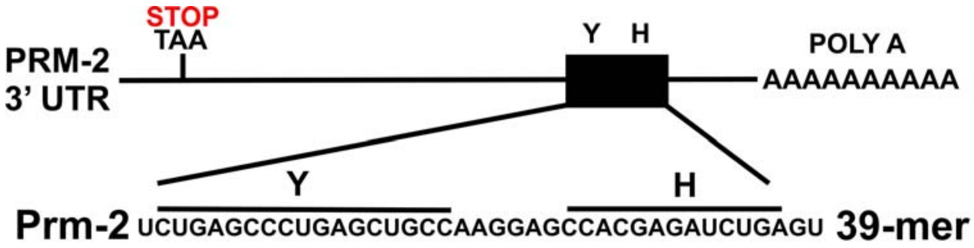

Figure 6.5: The 3'UTR of the protamine-2 (PRM-2) mRNA. This 39-mer contains sequences designated Y and H elements, which were proposed to be the *in vivo* targets of translin. This figure was adapted from [42].

Electron Microscopy Structure of Translin

The EM structure of translin showed that it exists as an octameric complex in solution with the eight monomers arranged like a pinwheel around a central cavity (Figure 6.6). The EM structure of translin existed as either a single or double octameric ring, but not higher order aggregates [47]. Each translin monomer appeared to exist in a two domain module in the octamer. The "tunnel" through the ring is tapered with a diameter of 50Å at one end and 30Å at the other. The entire octameric particle is 115Å in diameter. Addition of a 24 base DNA substrate resulted in the central channel being filled with density, implying that DNA substrates are bound at the center of the octamer (Figure 6.6)

It was observed that the DNA makes contact with four of the translin subunits, with the two subunits being next to each other in the ring. The binding of a 39-nt Y and H element containing RNA sequence was also investigated by EM with the RNA also occupying the central channel of the ring [47]. However, the specifics of the RNA recognition compared to the DNA recognition did differ. First, whereas the DNA sequence was recognized through two points of contact occurring between two sets of adjacent translin monomers, the RNA was observed to make four points of contact with alternating translin monomers. Additionally, the DNA-translin interaction was only observed to take place at the wide end of the translin ring resulting in the DNA density only being observed at one end. In contrast to this result, the RNA ligand was found to bind at both the top and bottom of the channel. In particular, this observation was consistent with mutational studies that demonstrated that both basic regions in translin, residues 56-64 and 86-97, are used for interaction with RNA but only the C-terminal basic region is used for interaction with DNA [46].

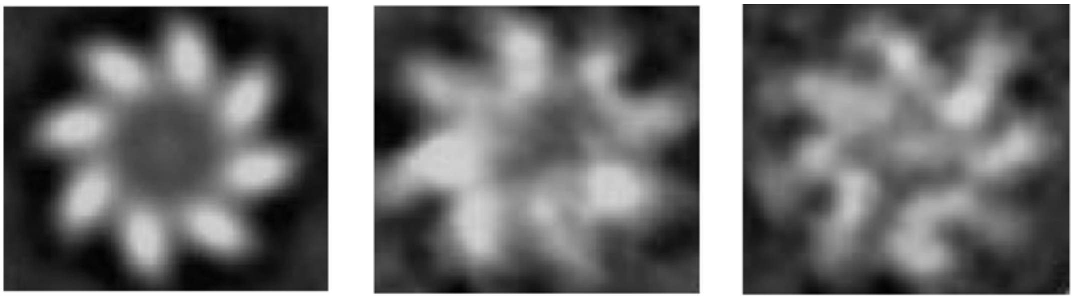

Translin Translin and DNA Translin and RNA

Figure 6.6: EM structure of the Translin complex. (Left) Translin (Middle) Translin complexed with DNA (Right) Translin complexed with RNA. Translin exists as an octameric disc, ~115 Å in diameter, with the eight subunits centered around a central hole. The binding of an RNA or DNA ligand was observed to fill the central cavity, with the DNA ligand making two points of contact and the RNA ligand making four. These images are from [47].

Crystal Structures of Mouse and Human Translin

Presently there are two crystal structures of translin from the mouse and human isoforms. The mouse translin (tb-rbp) structure was solved to 2.65Å resolution in the orthorhombic $P2_12_12$ space group with 4 translin monomers in the asymmetric unit. Each translin monomer is 80Å in length and the dimensions of the globular part of the protein are 20Å x 35Å x 50Å (Figure 6.7). The four translin monomers are arranged around a pseudo 4-fold axis that can be dimerized to form an octamer in the shape of a prolate ellipsoid (Figure 6.8) [48]. The structure is almost exclusively alpha helical with more than 70% of the protein's 228 amino acid residues found in the structure's 7 alpha helices [48].

The protein core is centered around helix 3, with helices 1 and 2 lying on one side and helices 5, 6, and 7, which form the C-terminal region, on the other [48]. The structure of the C-terminal portion of the protein was of particular interest since it contained a putative leucine zipper domain [40]. It had been demonstrated that point mutations of two leucines in this sequence abolished octamer formation and consequently nucleic acid binding [49]. However, the crystal structure revealed that the leucine zipper is nonfunctional in the traditional sense since many of these residues are involved in intramolecular contacts of the three helix bundle formed by helices 4, 5, and 6, not intermolecular oligomerization contacts between monomers. Although the C-terminus of translin was shown to not contain a leucine zipper in the traditional sense, the protein was observed to assemble in an ordered manner with the C-termini of the 4 monomers in each asymmetric unit arranged around a pseudo 4-fold axis. The C-terminal residues Val156, Val159, Thr160, Leu184, Leu212, and Ile214, along with Gln29, Arg36, and Gln43 of the first α-helix make the intermolecular contacts that allow for the C-termini to pack in this manner [48].

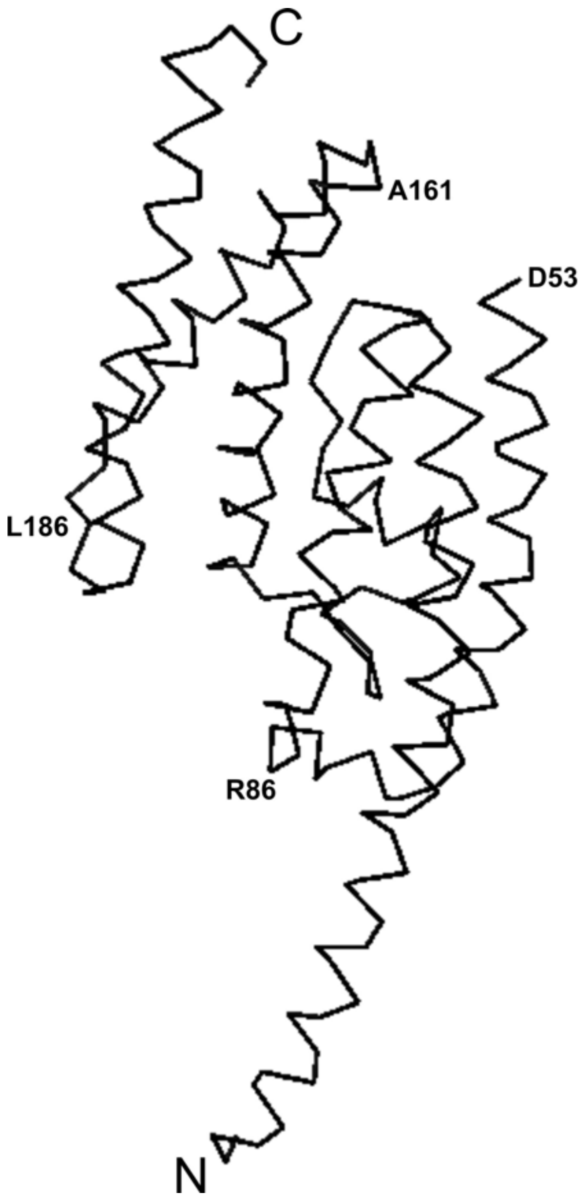

Figure 6.7: The backbone trace of a translin (mouse) monomer. Each monomer consists of 7 alpha helices comprising ~70% of the protein.

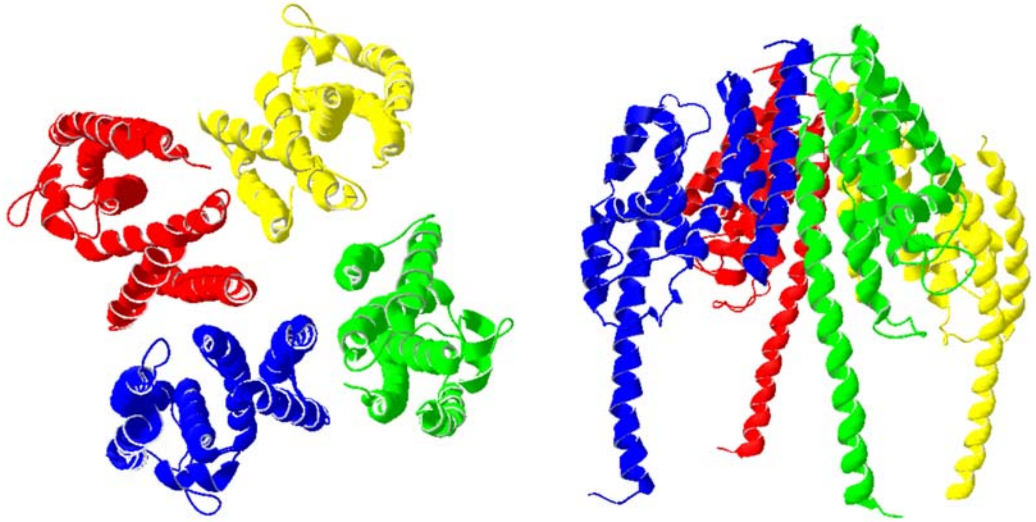

Figure 6.8: Crystal structure of mouse translin. The asymmetric unit of translin contains four monomers arranged around a pseudo four-fold axis perpendicular to the plane of the page in the left diagram and parallel to the plane of the page in the right diagram.

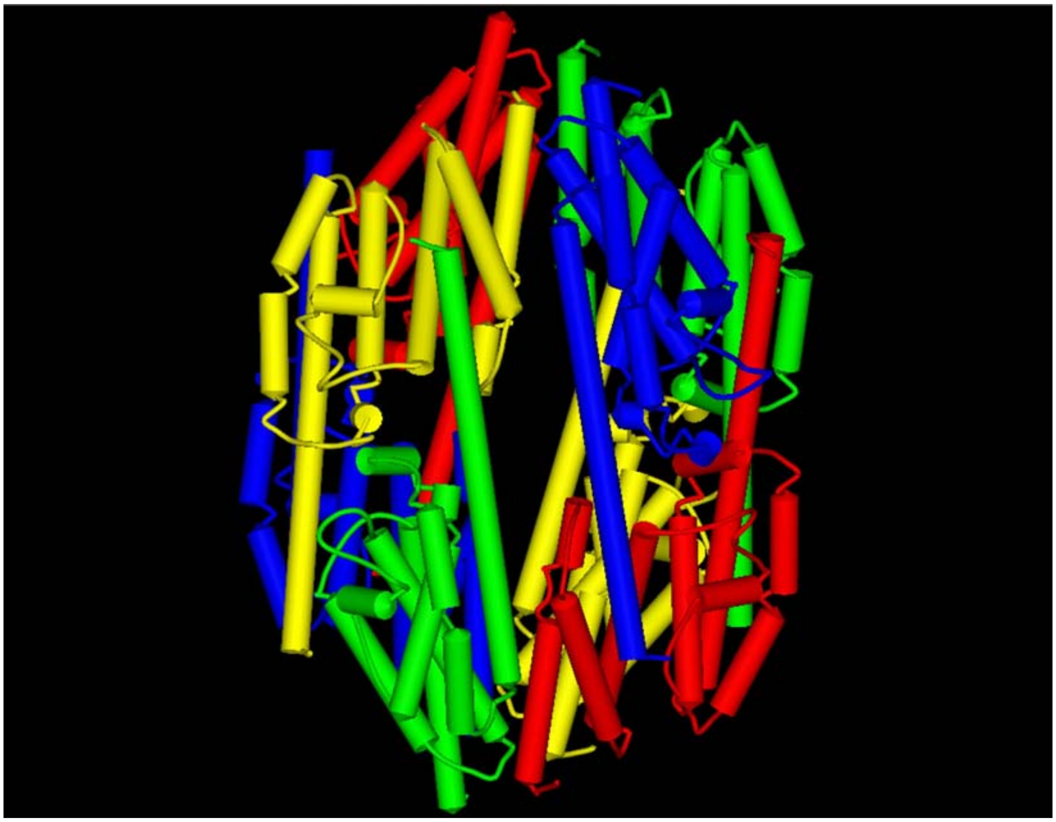

Figure 6.9: Higher order assembly of the translin complex. Performing a two-fold crystallographic operation results in an octameric translin particle in the shape of an elongated ellipsoid of dimensions 10.5nm x 8.0nm containing a central cavity ~ 20Å across. However, this ellipsoid has no open channel running through it, and without some sort of rearrangement of the subunits it would not be capable of binding extended oligonucleotides

The last 10 residues (219-228) of translin were not observed in the crystal structure [48]. This segment of the protein may be in a flexible state because of the specific crystallization conditions or it could also be the case that these residues only adopt a stable confirmation when the oligomer is bound to an RNA or DNA substrate. This part of the protein is of particular interest since it contains Cys225, the candidate residue that forms disulfide linkages between monomers, and it should be pointed out that dissolved translin crystals migrated as dimers on a non-reducing SDS gel, suggesting that although not directly observed, a disulfide linkage is present [48, 49]. However, it should be noted that this cysteine is not conserved in other translin homologues, and that the reducing environment of the cytoplasm would not favor the formation of disulfide linkages [48]. In addition to the C-termini packing around a pseudo 4-fold axis, an extensive, crystallographic 2-fold dimer interface was also observed [48]. This dimer interface is formed from packing interactions between helix 1, the three helix bundle formed by helices 5, 6, and 7, and the random coil between helices 2 and 3. Additional intermonomer interactions are also made between the main chain and side chain atoms of Tyr85 and Arg86 [48].

Execution of the 2-fold symmetry operator on a translin dimer creates a tetrameric particle with a concave surface, and the dimer interface buries greater than 1700Å^2 of surface area per monomer (Figure 1.7) [48]. Executing another 2-fold symmetry operator on the 4 monomers of the asymmetric unit, which are arranged around a pseudo 4-fold axis, results in the construction of an octameric particle in the shape of a prolate ellipsoid of approximate dimensions 10.5nm x 8.0nm containing a central cavity ~ 20Å across (Figure 6.9) [48]. Residues 86-90 of each monomer, which are known to be crucial for both DNA and RNA recognition, are positioned at the interior of the particle (Figure 6.10). The dimensions of the central cavity are such that it could accommodate a small piece of RNA, however, this octameric assembly could not bind an extended oligonucleotide since there is no “tunnel” for the oligo to enter and exit from [48]. Therefore, it was concluded that this assembly of monomers does not represent the functional form of translin and may represent an intermediate assembly of the protein complex [48].

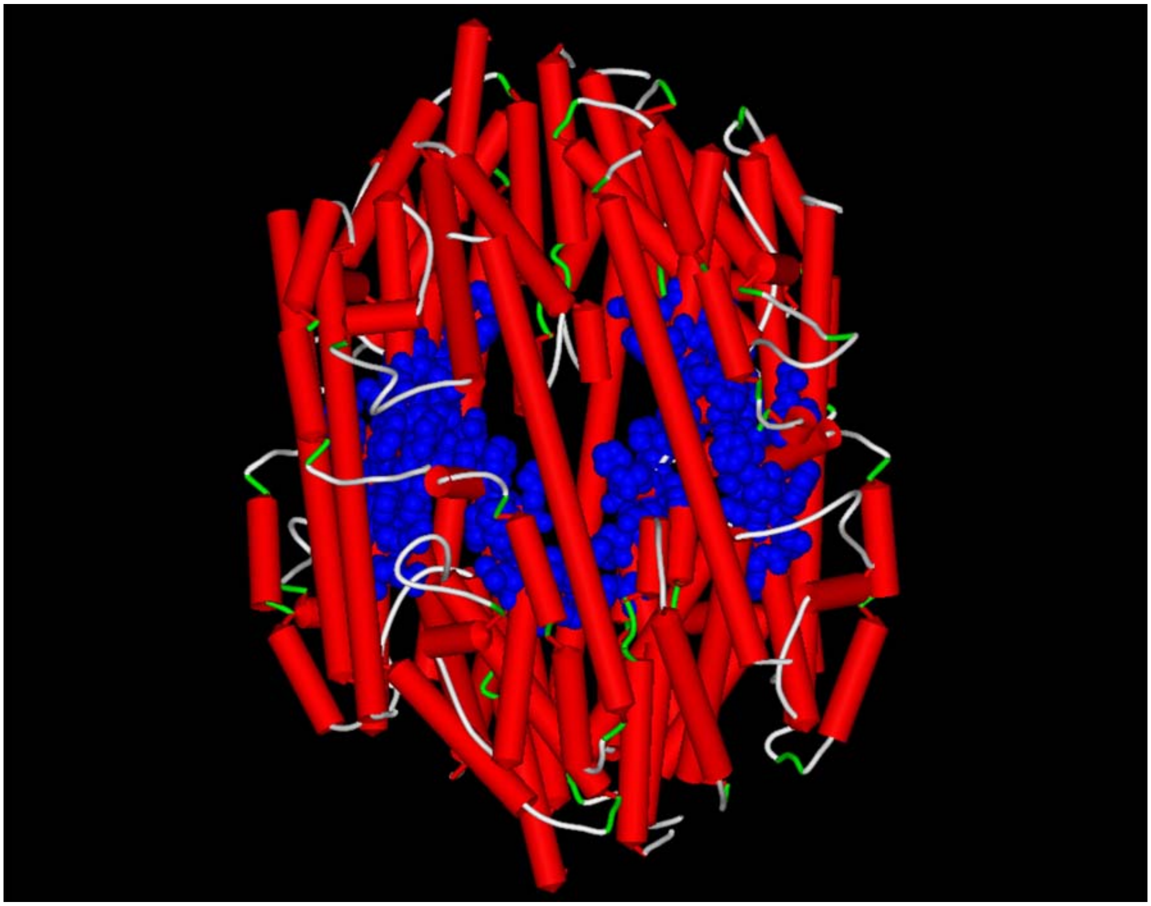

Figure 6.10: DNA/RNA binding residues in translin. The side chains of amino acids 86-90 are shown as blue spheres and are compacted on the interior of the ellipsoidal particle. Because no "tunnel" exists in this structure, this assembly of the translin octamer could not interact with extended oligonucleotides.

Human translin crystallized in the orthorhombic space group $C222_1$ with unit cell constants a = 129.424Å, b = 135.272Å, and c = 134.345Å. This structure is very similar to the mouse structure, which is expected since these two sequences share 99% identity. The human structure crystallized with four monomers in the asymmetric unit, arranged around a pseudo four-fold axis, with each one of the monomers being composed of seven α-helices (Figure 6.11). An octameric complex can be generated by executing a two-fold symmetry operator, which results in an octameric particle of dimensions 90Å x 90Å x 110Å with a central cavity ~15Å across. Furthermore, as with the mouse structure, Cys225, the candidate residue for disulphide bond formation and dimerization of two translin monomers, was not visible, and the hypothetical leucine zipper of residues 177-212 was not observed to be a functional leucine zipper in this crystal structure either. However, a comparison of the $C\alpha$ atoms of the mouse and human structures did reveal some difference in the relative positions of the tetrameric assembly, perhaps indicating that the assembly of translin multimeric complexes has a degree of flexibility.

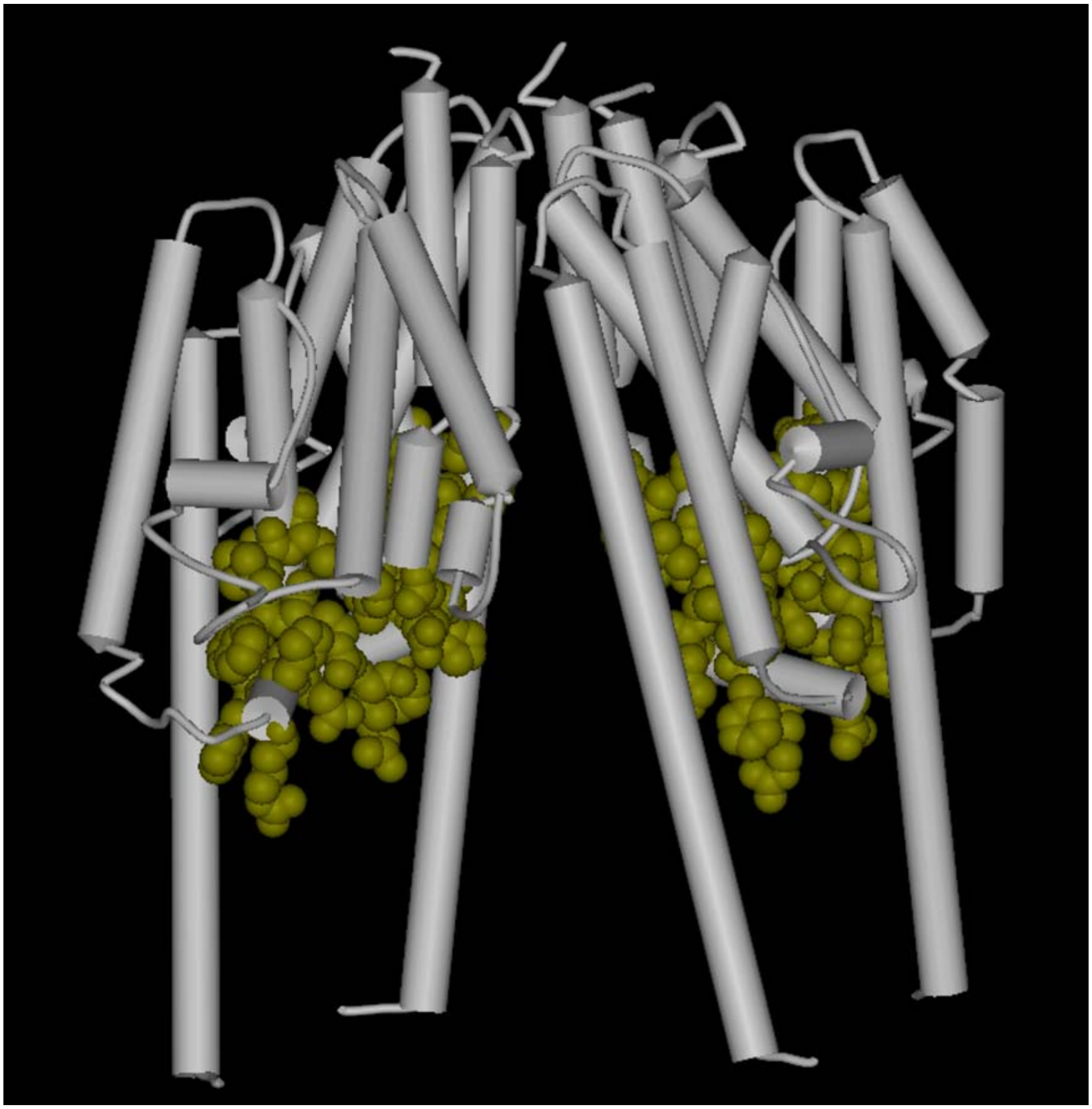

Figure 6.11: The asymmetric unit of human translin. The side chains of residues 86-90, which are known to be required for DNA binding, are packed on the interior and inaccessible to extended oligonucleotides. Both the human and mouse translin structures were observed in this assembly, which is not capable of binding extended oligonucleotides.

Translin Associated Factor X (Trax)

Yeast two hybrid experiments identified another candidate partner protein for translin named translin associated factor x (trax) [50]. Follow up immunoprecipitation experiments verified that translin and trax form a heterocomplex *in vivo* and also revealed that the translin●trax heterocomplex is the predominant cellular species [51].

Trax is a 33KDa protein that shares ~30% sequence identity with translin; it is not capable of binding nucleic acids alone [46, 52]. Trax has a functional nuclear localization signal and like translin, has a putative leucine zipper sequence (Figure 6.12) [46]. The strong link between these two proteins was reinforced when it was demonstrated through mouse knockout experiments that deletion of the translin gene led to the absence of trax protein in spite of the fact that trax mRNA levels were normal as verified by northern blot [53]. This suggests that translin has a chaperone role for trax and that trax most likely only exists *in vivo* as a member of a heteroprotein complex.

Characterizing trax has proven difficult primarily due to the fact that the pure protein is very unstable and has yet to be successfully expressed recombinantly. Biochemical studies have shown that trax possesses a functional nuclear localization signal and interacts with proteins other than translin [54, 55]. One of these partner proteins is C1D a versatile nuclear protein involved in DNA double stranded break repair and VD(J) recombination [55]. Further research is requisite to determine whether DNA or possibly both DNA and RNA are targeted by translin and what role trax plays in these activities.

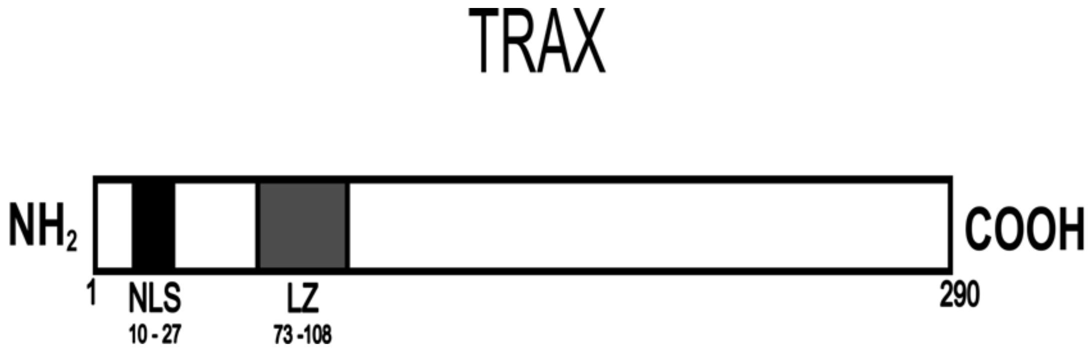

Figure 6.12: The domains of trax. NLS and LZ represent the nuclear localization signal and the putative leucine zipper, respectively. This figure was adapted from [46].

Project Goals

Translin and trax play important roles in mRNA trafficking and storage, processes crucial for development in neurons and male germ cells. At the onset of this research project, a handful of studies on translin had been published, but a consensus RNA or DNA sequence that this protein targets had still yet to be identified. The exact role of trax in these processes also had yet to be determined. Furthermore, although two crystal structures of mouse and human translin existed, neither one of them showed how a functional translin complex capable of binding extended oligonucleotides was assembled. The goals of this study were to characterize the RNA and DNA binding activities of translin and the translin●trax complex, with the intent of clarifying trax's cellular role and translin's target sequence. Another goal of this study was to crystallize translin●oligonucleotide complexes and/or translin●trax complexes, as high resolution structures of these complexes would provide specific details into how DNA and RNA recognition is occurring.

Chapter 7: Materials and Methods

Materials

Plasmids containing the mouse translin gene cloned into pGEX-4T1, (Amersham Biosciences, Piscataway, NJ), and the mouse trax gene cloned into pET28a, (Novagen, Madison, WI), were generously provided by the Hecht laboratory (University of Pennsylvania Medical Center, Philadelphia, PA). Ni-NTA His-Bind® resin obtained from Novagen (Madison, WI). Glutathione agarose resin was obtained from sigma. 5' fluorescently labeled oligonucleotides were obtained from IDT DNA (Coralville, IA). The pre-packed HiPrep 26/60 Sephacryl S-300 High Resolution and HiLoad 16/60 Superdex prep grade columns were obtained from GE healthcare (Piscataway, NJ). The pET-DUET-1 and pET-39 expression vectors were obtained from Novagen (Madison, WI).

Methods

Expression and Purification of Recombinant Translin

The pGEX-4T1-translin (*M. musculus*) vector was transformed into *E. Coli* strain BL21(DE3) under the selection of ampicillin. Fresh transformants were grown in Terrific Broth media (Difco) at 37°C until reaching an optical density of 0.7. Upon reaching this OD the translin-GST fusion protein was expressed by the addition of IPTG to a final concentration of 300μM. Cells were allowed to grow for another 6 hours post induction, and were harvested by centrifugation at 4000g for 10 minutes. Cells were resuspended in lysis buffer (25mM Tris-HCl pH 8, 250mM NaCl) and run through a French Pressure cell 3 times at 1000 PSI. Cell debris was removed by centrifugation at 30,000g for 1 hour and the crude cell lysate was passed though a column packed with a glutathione-agarose matrix (Sigma). The column was washed with 500 mL of a 25 mM Tris-HCl pH 8.0, 150 mM NaCl buffer and a 9 mL slurry resuspension of the matrix and wash buffer was transferred to a 50 mL conical tube. 50 units of thrombin (Sigma) and 1 mL of 10X thrombin cleavage buffer was added to the resuspended matrix and the cleavage reaction was incubated at 25 °C for 16 hours before the matrix was repacked in a 10 mL disposable column and the free translin was eluted with wash buffer (25 mM Tris-HCl pH 8.0, 150 mM NaCl). Protein containing fractions were pooled together and dialyzed against a 10 mM Tris-HCl pH 8.0, 50 mM KCl buffer and concentrated. The recombinant translin was further purified by gel filtration using a HiPrep^{TM} 26/60 Sephacryl S-300 High Resolution column and an AKTA FPLC system (GE Healthcare, Piscataway, NJ). The protein was loaded onto an S-300 column that had been previously equilibrated with a 10mM Tris-HCl pH 8, 50mM KCl buffer and run through the matrix at a flow rate of 1mL/min. Protein containing fractions were pooled together, concentrated, and stored at 4 °C.

Crystallization of Translin●d(GT)$_{15}$ Complex

The purified translin protein was concentrated to 15-17mg/mL, as determined by OD$_{280}$ absorption readings and Beer's Law:

$C = A/\varepsilon b$

Where:

C = the protein concentration (mg/mL)
A = the absorption at 280nM
ε = the extinction coefficient of translin; calculated as 0.67 $(\mathrm{mg/mL})^{-1}\mathrm{cm}^{-1}$
b = the cuvette pathlength, 1cm

Translin●(GT)$_{15}$ crystals were grown from a mother liquor of 0.1M Sodium Acetate pH 5.0, 0.1M $MnSO_4$, 20% polyethylene glycol 1000 (Figure 7.1). Briefly, the d(GT)$_{15}$ ligand was added to translin and allowed to equilibrate for 5 minutes at 4 °C. Crystal drops were set up using the sitting drop method by combining 3 μL of the translin●d(GT)$_{15}$ sample with 3 μL of mother liquor in a VDX crystallization plate (Hampton Research, Aliso Viejo, CA), sealed with tape, and allowing the drop to equilibrate at 4 °C.

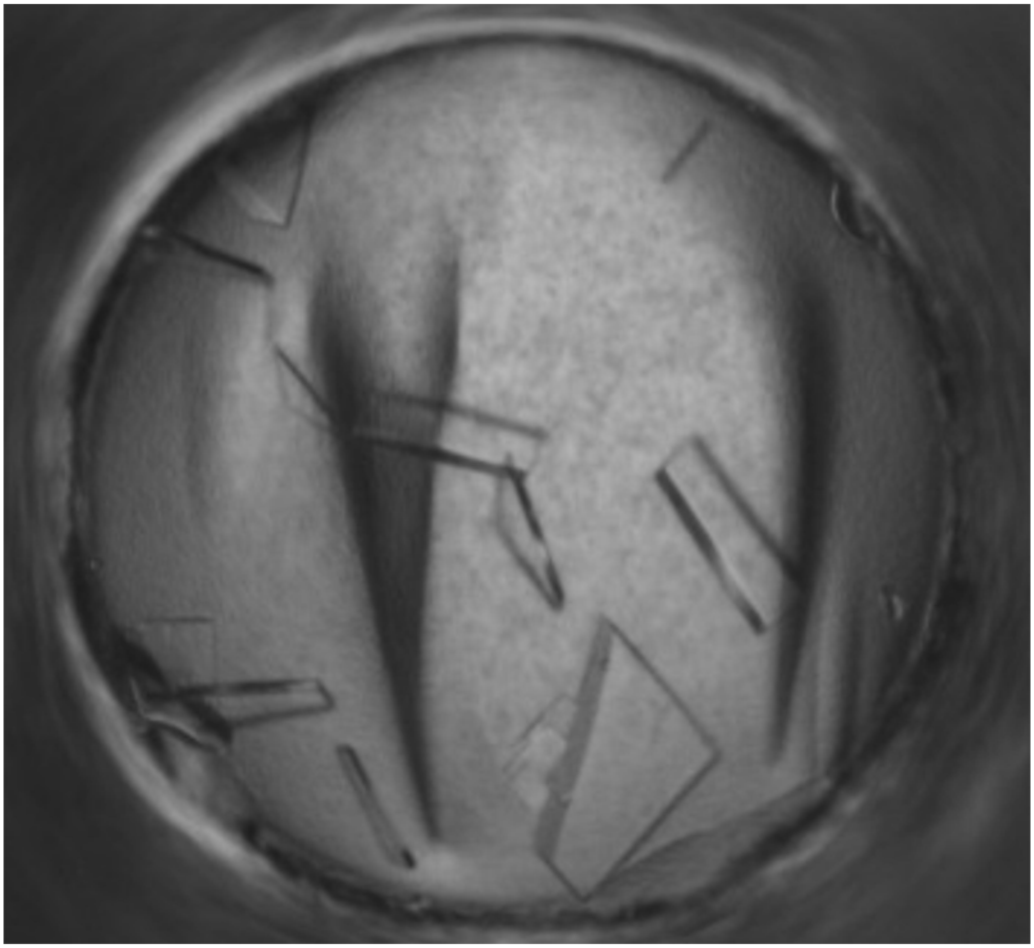

Figure 7.1: Translin●d(GT)$_{15}$ crystals. Translin●d(GT$_{15}$) crystals were grown from a mother liquor of 0.1M Sodium Acetate pH 5.0, 0.1M $MnSO_4$, 20% polyethylene glycol 1000.

Cryo-cooling and Diffraction of Translin●d(GT)$_{15}$ Crystals

The translin●d(GT)$_{15}$ crystals were removed from the sitting drop using a nylon loop, soaked in a 0.1M Sodium Acetate pH 5.0, 0.1M $MnSO_4$, 35% polyethylene glycol 1000 solution, and flash frozen in liquid nitrogen. The crystals were then mounted for data collection. The initial diffraction frames revealed that the translin●d(GT)$_{15}$ complex diffracted poorly (~ 10Å). Furthermore, several attempts at crystal optimization were unsuccessful in improving data quality, and as a result, no complete data sets of the translin●(GT)$_{15}$ crystals were collected.

Cloning, Expression, and Purification of Recombinant Translin●Trax Complex

A plasmid expressing translin and trax from independent promoters was constructed by Jennifer Schleit in our laboratory. The *M. musculus* genes for translin and trax were amplified by high-fidelity PCR and inserted into the pET-DUET1 expression vector. The *M. musculus* trax gene was amplified using the forward primer of sequence 5′-GCGC**GGATCC**ATGAACGGCAAAGAAGGACC-3′ (BamHI restriction site shown in bold and underlined) and the reverse primer 5′-GCCC**AAGCTT**TTAAGAAATGCTCTCTTCCTGATC-3′ (HindIII recognition site shown in bold and underlined). This 290aa ORF encodes a 6X HisTag fused to the N-terminus. The *M. musculus* translin gene was amplified using the forward primer of sequence 5′-GGAATTC**CATATG**TCTGTGAGCGAGATCTTCGTG-3′ (NdeI restriction site shown in bold and underlined) and the reverse primer 5′-CGC**GGTACC**CTATTTTTCACCACAAGCCGCTGC-3′ (KpnI restriction site shown in bold and underlined).

The pET-DUET1-translin●trax vector was transformed into *E. Coli* strain Rosetta 2 (DE3) under the dual selection of ampicillin and chloramphenicol. Fresh transformants were grown in Terrific Broth media (Difco) at 37°C until reaching an optical density of 0.7. Upon reaching this OD_{600} the translin●trax protein complex was expressed by the addition of IPTG to a final concentration of 1mM. Cells were allowed to grow for another 3 hours post induction, and were harvested by centrifugation at 4000g for 10 minutes. Cells were resuspended in lysis buffer (25mM Tris-HCl pH 8, 500mM NaCl, 10mM imidazole) and run through a French Pressure cell 3 times at 1000 PSI. Cell debris was removed by centrifugation at 30,000g for 1 hour and the crude cell lysate was passed though a column packed with Ni-NTA His-Bind® resin. The column was washed with 500 mL of a 25 mM Tris-HCl pH 8, 500mM NaCl, 10 mM imidazole buffer and the heterocomplex was eluted with a linear gradient from10 – 250mM imidazole. Protein containing fractions were pooled together and dialyzed against a 10 mM Tris-HCl pH 8.0, 50 mM KCl buffer and concentrated. The recombinant translin●trax was further purified by gel filtration using a HiPrep™ 26/60 Sephacryl S-300 High Resolution column and an AKTA FPLC system (GE Healthcare, Piscataway, NJ). The protein was loaded onto an S-300 column that had been previously equilibrated with a 10mM Tris-HCl pH 8, 50mM KCl buffer and run through the matrix at a flow rate of 1mL/min. Protein containing fractions were pooled together, concentrated, and stored at 4°C.

Gel filtration Analysis of the Translin●Trax Complex

Gel filtration experiments of the recombinant translin●trax complex were carried out using a HiPrep™ 26/60 Sephacryl S-300 High Resolution column and an AKTA FPLC system (GE Healthcare, Piscataway, NJ). A 1 mL sample of the translin●trax complex was concentrated to 20 mg/mL and passed through the gel filtration system in 25 mM Tris pH 7.5, 150 mM NaCl buffer at a flow rate of 1mL/min. The molecular weight of the native complex was calculated from the linear regression analysis of a calibration curve of K_{av} vs. log[molecular weight] (where K_{av} = (protein elution volume – column void volume)/(column bed volume – column void volume) that was constructed using the elution profiles of the following protein standards and their respective molecular weights: blue dextran (2000 KDa), thyroglobulin (669 KDa), ferritin (440 KDa), aldolase (158 KDa), conalbumin (75 KDa), and ovalbumin (43 KDa). The majority of the translin●trax complex eluted at a volume that correlates to an apparent molecular weight of ~ 340 KDa.

Fluorescence Polarization Assays

Fluorescence polarization (FP) is a convenient and robust technique for measuring the association of ligands with macromolecules. A fluorescent ligand tumbles more quickly than one bound to a protein. When exposed to polarized light the free ligand can tumble randomly during the fluorescent life time and the emitted light will depolarize, while a ligand bound to a large protein will retain some polarization. Here, fluorescently labeled polynucleotides were titrated with binding proteins (translin or translin•trax); as binding increases fluorescence polarization (FP) increases.

Serial dilutions of stock protein samples were prepared using storage buffer as the diluent. For each 30 μL sample, 3 μL of 10X binding buffer (250 mM Tris-HCl pH 8, 1M NaCl, 10 mM $MgCl_2$) was combined with a stock fluorescent nucleotide solution and a balancing volume of stock protein sample to give a final nucleotide concentration of 5 nM. The eight nucleic acid ligands used were designated rGA, rCA, dGA, dCA, rGAG, dGAG, PRM-2, and d(PRM-2); their sequences were $A(GA)_{12}$, $A(CA)_{12}$, $d(A(GA)_{12})$, $d(A(CA)_{12})$, $A(GAG)_8$, $d(A(GAG)_8)$, UCUGAGCCCUGAGCUGCCAAGGAGCCACGAGAUCUGAGU, and d(UCUGAGCCCUGAGCUGCCAAGGAGCCACGAGAUCUGAGU), respectively. All eight of these ligands had 5' fluorescein modifications. These ligands were chosen based on a previously published study investigating the nucleic acid binding activity of the translin●trax complex purified from brain tissue extracts [42]. The 39nt PRM-2 sequence was taken from the 3' UTR of the protamine-2 mRNA and represents an *in vivo* target of translin. Prior to addition of the nucleotide to the protein sample nucleotide solutions were heated to 70 °C and cooled at 25 °C for 3 minutes. 20 μL of each protein-nucleotide sample was added to a 384 well plate (Thermo Fisher Scientific, Rochester, NY), and fluorescence polarization was read using the Perkin Elmer Envision plate reader. Scatter plots of translin concentration and translin●trax concentration vs. polarization were constructed using Sigma Plot (Systat Scientific, San Jose, CA) and fit to a hyperbola.

Cloning, Expression, and Purification of DsbA●Trax

The *M. musculus* gene for trax was amplified by high-fidelity PCR and inserted into the pET-39 expression vector. The *M. musculus* trax gene was amplified using the forward primer of sequence 5′-ATGGCGATATC**GGATCC**GTCGCCAAAATCGGAT***CTGGTTCCGCGTGGAAGT***CCGTTCGAAAAGGGTATGAACGGCAAAGAAGGACCAGGAGGGTTC-3′ (BamHI restriction site shown in bold and underlined, thrombin recognition site shown in bold and italicized) and the reverse primer 5′-CGAGTTTCGA**GCGGCCGC**CCCGGGTCCCTGAAAGAGGACTTCAAGAGCACC

CTTTTCGAACGGACTTCCACGCGGAACCAGATCCGATTTTGGTTAAGAAATGC TCTCTTCCTGATCAATCATGTCTG-3′ (NotI recognition site shown in bold and underlined). The 873nt trax ORF encodes was inserted downstream of the 627nt ORF of DsbA, resulting in a 70KDa fusion protein with a 6X His Tag sequence in the 64aa linker region. Because the DsbA ORF contains the 19aa pelB leader sequence, the fusion protein will be exported to the periplasmic space and can be purified by osmotic shock protocols. The pET39-trax vector was transformed into *E. Coli* strain BL21(DE3) under the selection of kanamycin. Fresh transformants were grown in Terrific Broth media (Difco) until reaching an optical density of 0.7. Upon reaching this OD600 the expression of the DsbA●trax fusion protein was induced by the addition of IPTG to a final concentration of 1mM. Cells were allowed to grow for another 3 hours post induction, and were harvested by centrifugation at 4000g for 10 minutes. Cells were resuspended in 30mM Tris-HCl pH 8.0, 20% sucrose buffer at a volume of 400mL of buffer for each liter of cell culture. EDTA was added to a final concentration of 1mM along with 10mg of hen egg white lysozyme and the resuspension was allowed to mix at 4°C for 30mins. Lysozyme was added to breakdown the cell wall, allowing for the release of the contents of the periplasmic space into the buffer. $MgCl_2$ was then added to a final concentration of 5mM and the resusupension was centrifuged for 10min at 10,000g to remove the spheroplasts. The supernatant was decanted and 10X IMAC buffer (250mM Tris pH 8.0, 5M NaCl, 100mM imidazole) was added to the supernatant to give final concentrations of 25mM Tris-HCl pH 8.0, 500mM NaCl, 10mM imidazole. The supernatant was then loaded onto a column packed with Ni-NTA His-Bind® resin that had been pre-equilibrated with 1X IMAC buffer. The column was washed with 500 mL of 1X IMAC buffer and the fusion protein was eluted with a linear gradient from10 – 250mM imidazole. Protein containing fractions were pooled together and dialyzed against a 10 mM Tris-HCl pH 8.0, 50 mM KCl buffer, concentrated, and stored.

Western blot Analysis of DsbA●Trax

The DsbA●trax fusion protein was run on a 12% SDS page gel and the protein sample was transferred to a PVDF membrane (Millipore) at 100mA for 20 minutes using a blotting apparatus (Bio-Rad). The membrane was then incubated with blocking buffer (10mM Hepes pH 7.6, 150mM NaCl buffer containing 5% milk) for 2 hours at room temperature. The anti-trax antibody (rabbit) was diluted 1:1000 in blocking buffer and incubated with the PVDF membrane for 1 hour at room temperature. The membrane was then washed three separate times with blocking buffer for 5 minute incubations. The Horseradish Peroxidase conjugated secondary antibody (goat anti-rabbit) was diluted 1:6000 in blocking buffer and incubated with the PVDF membrane for 1 hour at room temperature. The membrane was then washed three separate times with blocking buffer for 5 minute incubations then an additional three times with 10mM Hepes pH 7.6, 150mM NaCl. The presence of the DsbA●trax fusion protein was detected using SuperSignal West Pico Chemiluminescent Substrate.

Chapter 8: Results

Expression, Purification, and Gel Filtration Analysis of Translin●Trax Complex

The recombinant translin●trax complex was successfully expressed in *E. coli* using a dual expression vector that contained two open reading frames (ORFs) with two separate T7 promoters. The recombinant complex was purified to homogeneity by Immobilized Metal Affinity Chromatography (IMAC) using a linear imidazole gradient followed by size exclusion chromatography. Because only the trax ORF encodes an N-terminal 6x-His tag, translin can only be purified from the Ni resin through its interaction with trax. When analyzed on a 12% SDS PAGE gel, the trax and translin bands appear to be present in a roughly 1:1 ratio (Figure 8.1).

The apparent molecular weight of the translin●trax complex was determined by gel filtration analysis on a sephacryl S-300 column, against high molecular weight, globular protein standards. The data (Figure 8.2) suggest a molecular weight for the complex of ~340 KDa, while that for pure translin was ~280 kDa.

These data would seem consistent with the notion that the complex is a heterodecamer of the form translin$_5$•trax$_5$ and that translin exists as a decamer. However, it should be noted that if the heteromeric complex, and translin, form cyclic disks, then the apparent volume of each complex in solution would be larger than a sphere of the same mass, and would run aberrantly heavy. Therefore, because translin has been observed as an octameric complex in electron microscopy and ultracentrifuge studies, it seems plausible to conclude that the true composition of the complex is most likely a heteroctamer of the form $\text{translin}_4 \bullet \text{trax}_4$.

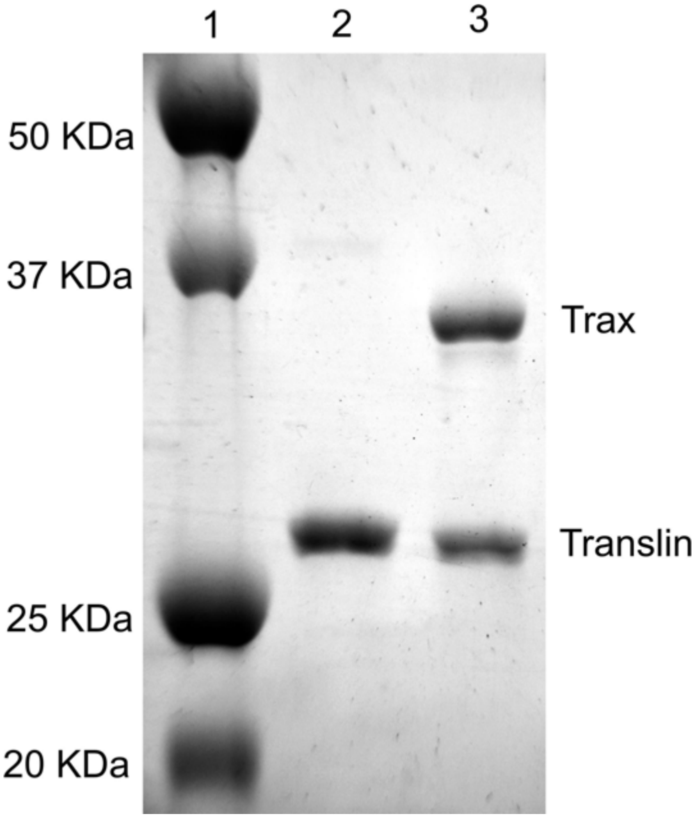

Figure 8.1: A 12% SDS gel of translin and translin●trax. Lane 1: molecular weight standards; Lane 2: recombinant mouse translin (26 KDa); Lane 3: recombinant mouse translin●trax complex (translin 26 KDa, trax 33 KDa).

.

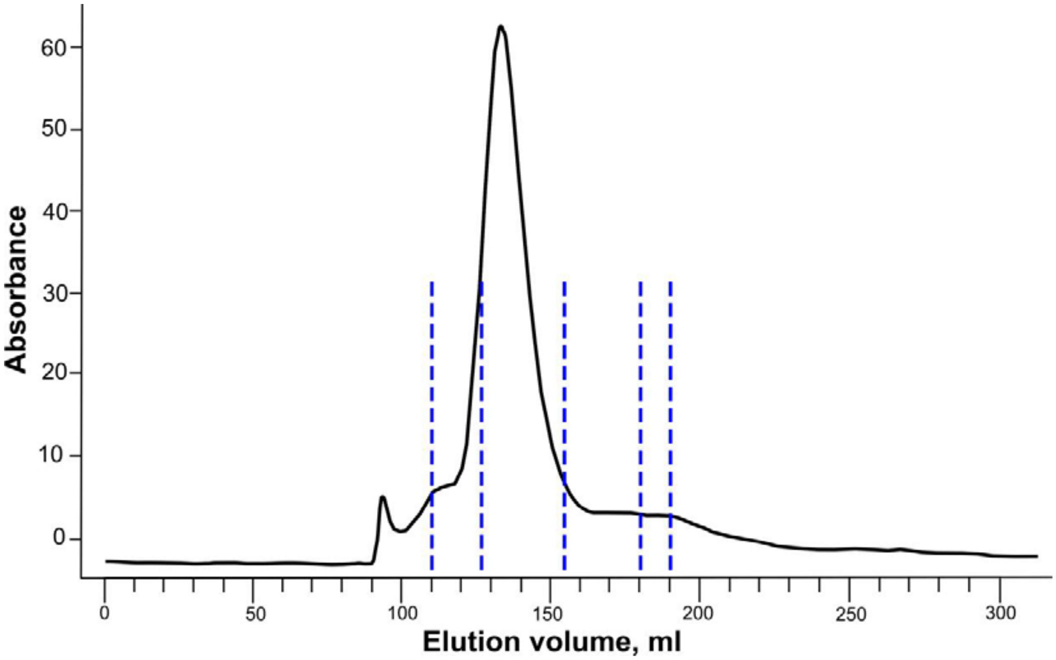

Figure 8.2: Gel filtration of the translin●trax complex. The elution profile of the recombinant translin●trax complex eluting from a sephacryl S-300 column. The elution volumes of thyroglobulin (669 KDa), ferritin (440 KDa), aldolase (158 KDa), conalbumin (75 KDa), and ovalbumin (43 KDa) are shown as dashed lines.

RNA and DNA Binding by Translin and Translin●Trax

To quantitatively investigate the binding of nucleic acids to translin, eight RNA and DNA ligands with 5’ fluorescein modifications were used: RNA ligands were PRM-2, rGA, rGAG, and rCA, and DNA ligands d(PRM-2), dGA, dGAG and dCA, (as defined in Materials and Methods). The binding of polynucleotides to recombinant translin as observed through the change in fluorescence polarization (FP) is shown in Figure 8.3 and the binding constants are summarized in Table 8.1. For these binding curves, the concentration of translin is defined as an octameric binding complex.

Translin was observed to bind the YH element containing PRM-2 mRNA, with a K_d of 200 nM. It bound the synthetic rGA with an even higher affinity, $K_d = 20$ nM. The rCA and rGAG polymers bound more weakly, with a K_d of 0.9 and 0.5 μM, respectively. In general, translin bound deoxyribonucleotides more poorly than ribonucleotides. For example, the dPRM-2 and dGA oligonucleotides each bound about 50 times worse than the corresponding RNA sequence. The oligonucleotide binding data for the translin●trax heterocomplex is shown in Figure 8.4. For these binding curves the concentrations shown represent the hetero-octamer, translin_4•trax_4, as the binding unit. In general, the translin●trax complex bound these oligonucleotides weaker than translin alone. Also, in contrast to translin the heterocomplex bound tighter to DNA sequences than RNA sequences, the opposite of the pattern displayed by translin. The physiological RNA substrate, the YH element containing PRM-2, has a K_d of 40 μM, about 100 times weaker than the binding of the same ligand to translin alone. However, consistent with the general trend, the translin●trax complex does bind d(PRM-2)10-fold tighter than it binds the equivalent RNA sequence, and 5-fold tighter than translin binds this DNA ligand. The synthetic ribonucleotides bind the complex with K_d values between about 30 and 100 μM. In marked contrast, the G-rich DNA polymers bind the complex avidly; dGA and dGAG have K_ds of 100 and 175 nM, respectively. The binding experiments suggested that, in general, translin and translin•trax prefer to bind to GA rich sequences, translin binds stronger to RNA, and the translin•trax complex binds stronger to DNA.

Table 8.1: Dissociation Constants for Translin_8 and Translin_4●Trax_4 Binding to RNA and DNA Ligands

Name	**Sequence**	**Translin_8 K_d (μM)**	**Translin_4●Trax_4 K_d (μM)**
PRM-2	5'UCU**GAG**CCCU**GAG**CUGCCAAGGAGCCAC**GAG**AUCU**GAG**U3'	0.2	40
rGA	5'AGAGAGAGAGAGAGAGAGAGAGAGA3'	0.02	28
rCA	5'ACACACACACACACACACACACACA3'	0.9	48
rGAG	5'AGAGGAGGAGGAGGAGGAGGAGGAG3'	0.5	104
dPRM-2	5'd(TCT**GAG**CCCT**GAG**CTGCCAAGGAGCCAC**GAG**ATCT**GAG**T)3'	10	4
dGA	5'd(AGAGAGAGAGAGAGAGAGAGAGAGA)3'	1	0.10
dCA	5'd(ACACACACACACACACACACACACA)3'	5	12
dGAG	5'd(AGAGGAGGAGGAGGAGGAGGAGGAG)3'	0.4	0.18

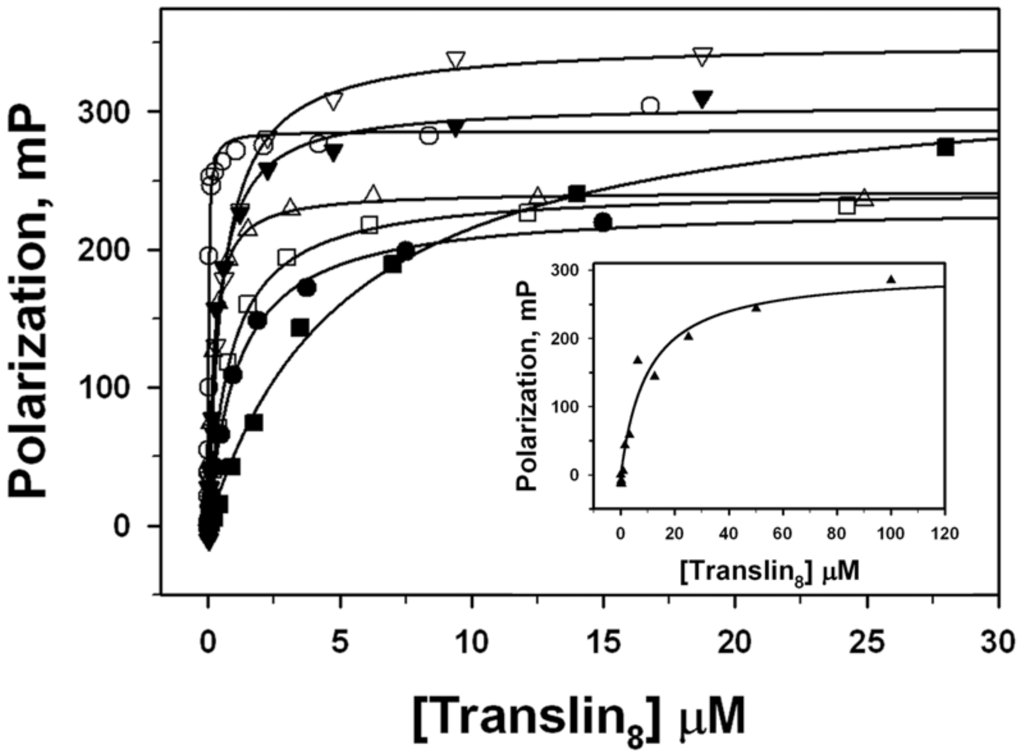

Figure 8.3: RNA and DNA binding by the translin complex. A plot of translin binding to rGA, rCA, dGA, dCA, rGAG, dGAG and PRM-2. GA sequences are represented as circles, CA sequences are represented as squares, GAG sequences are represented as inverted triangles, and PRM-2 is represented as triangles. RNA sequences are shown as open symbols and DNA sequences are shown as filled symbols. Inset: a plot of translin binding to d(PRM-2). Both plots were constructed using the translin octamer as the binding protein.

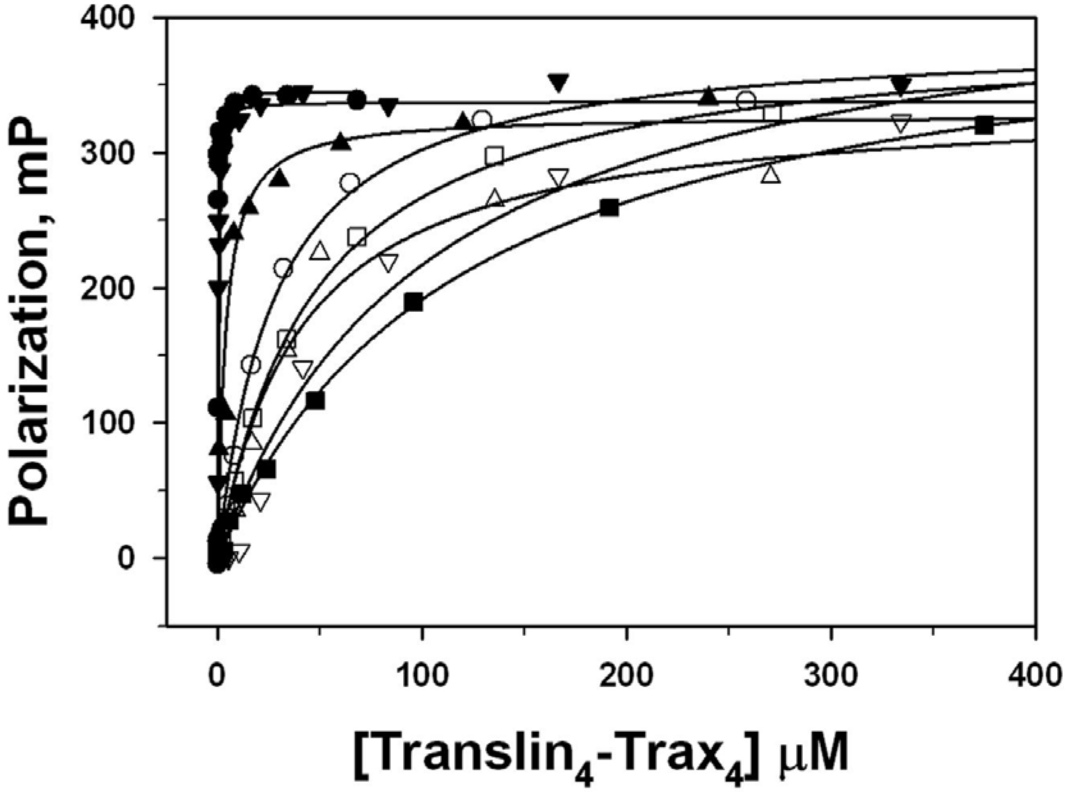

Figure 8.4: RNA and DNA binding by the translin●trax complex. A plot of translin●trax binding to rGA, rCA, dGA, dCA, rGAG, dGAG, PRM-2 and d(PRM-2). GA sequences are represented as circles, CA sequences are represented as squares, GAG sequences are represented as inverted triangles, and PRM-2 is represented as triangles. RNA sequences are shown as open symbols and DNA sequences are shown as filled symbols. This plot was constructed using the translin●trax hetero-octamer as the binding protein.

Analysis of Translin Binding PRM-2 Derivative Sequences

Because the initial binding studies showed that translin has affinity for GA rich RNA sequences, the role that GAG trimers have in the recognition of PRM-2 was explored. Two separate GAG trimers in the PRM-2 sequence were mutated to CAC, and a double mutant in which both trimers were altered was also used. These sequences, derived from PRM-2, were designated PRM-2 variants 1, 2 and 3 and are shown in Table 8.2. The bases that were mutated in the variant sequences are underlined. We also made a truncation variant in which the last 9 bases were removed from the 3' end of the oligonucleotide (labeled PRM-$2_{(1\text{-}30)}$). Table 8.2 shows the K_d values for the binding of these variant sequences to translin and the binding data is shown in Figure 8.5 and 8.6. Translin was observed to bind to PRM-2 Variant 1 with a K_d of 1 μM, a slight reduction in affinity from the wt PRM-2 sequence (K_d = 0.2 μM). It bound the other two mutant ligands, variants 2 and 3, and the truncation variant, with no significant decrease in affinity (K_d of 0.2, 0.3, and 0.2 μM, respectively).

Table 8.2: Dissociation Constants for Translin$_8$ Binding to PRM-2 and Variant PRM-2 Sequences

Name	**Sequence**	**translin$_8$ K$_d$ (μM)**
PRM-2	5’UCU**GAG**CCCU**GAG**CUGCCAAGGAGCCAC**GAG**AUCU**GAG**U3’	0.2
PRM-2 Variant 1	5’UCUGAGCCCUCACCUGCCAAGGAGCCACGAGAUCUGAGU3’	1
PRM-2 Variant 2	5’UCUGAGCCCUGAGCUGCCAAGGAGCCACCACAUCUGAGU3’	0.2
PRM-2 Variant 3	5’UCUGAGCCCUCACCUGCCAAGGAGCCACCACAUCUGAGU3’	0.3
PRM-2$_{(1-30)}$	5’UCUGAGCCCUGAGCUGCCAAGGAGCCACGA3’	0.2

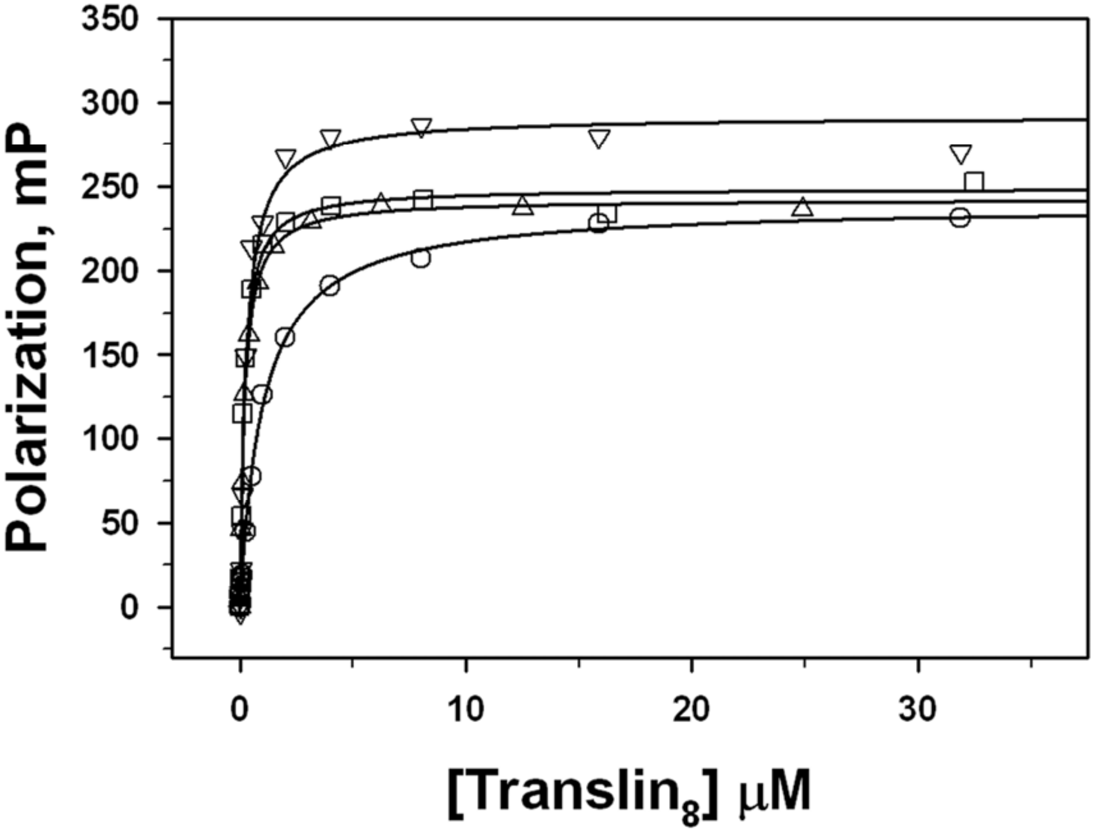

Figure 8.5: A plot of translin binding to PRM-2 and variant sequences. PRM-2 is represented as triangles, PRM-2 V1 as circles, PRM-2 V2 as squares, and PRM-2 V3 as inverted triangles.

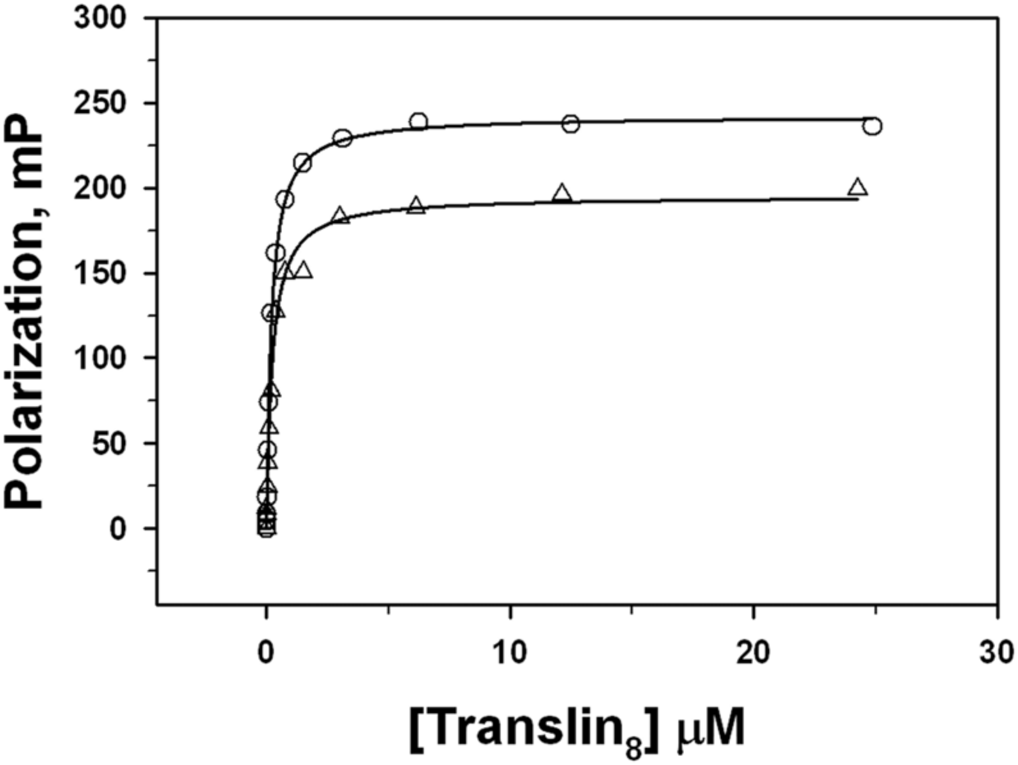

Figure 8.6: A plot of translin binding to PRM-2 and PRM-2$_{(1-30)}$. PRM-2 is represented as triangles and PRM-2(1-30) is represented as circles.

Expression and Purification of Recombinant DsbA●Trax

The DsbA●trax recombinant fusion protein was successfully expressed and purified from the periplasmic fraction (Figure 8.7). The DsbA●trax fusion protein was soluble to at least a concentration of 5mg/mL in 10mM Tris-HCl pH 8.0, 50mM KCl buffer. An attempt to isolate the recombinant trax protein by removal of the DsbA tag by thrombin cleavage resulted in the precipitation of over 90% of the trax protein. Subsequent attempts to isolate the recombinant trax protein by varying the salt concentration, pH, and temperature were also unsuccessful and resulted in precipitation of the trax protein. Several more thrombin digests of the fusion protein were attempted with varying concentrations of CHAPS detergent, however, these were also unsuccessful.

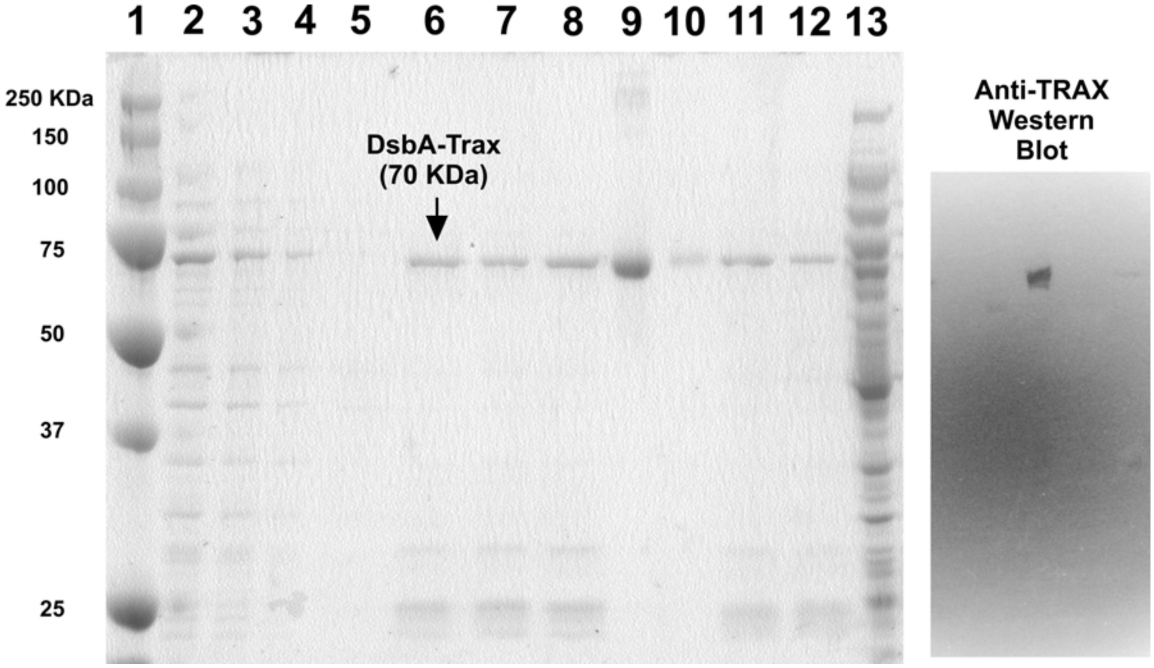

Figure 8.7: (Left) A 12% SDS gel of purified recombinant DsbA●trax. Lane 1: Molecular weight marker. Lanes 2-4: Periplasmic fraction. Lanes 6-8, 11,12: Purified recombinant DsbA●trax (70KDa). Lanes 9 and 10: BSA (69KDa). Lane 13: Fraction taken from spheroplasts lysate. (Right) An anti-trax western blot of the purified DsbA●trax fusion protein.

Chapter 9: Discussion

Translin and trax play roles in very important cellular processes, such as DNA recombination and the spatial and temporal expression of mRNA, yet the exact biochemical details of their roles remain elusive. A comparative study of the nucleic acid binding activities of translin and the translin●trax complex was requisite for defining what roles translin, trax, and the translin●trax complex have in recombination, RNA trafficking, and the post-transcriptional regulation of gene expression. It can be concluded from these experiments that translin alone prefers to bind GA-rich RNA sequences, while the translin●trax complex shifts the binding affinity to GA-rich DNA sequences as shown in Table 8.1. It was observed that translin binds poly-GA with sub-micromolar affinity, while the translin•trax complex binds poly-dGA with sub-micromolar affinity. Conversely, translin binds the corresponding dGA nearly 1000 times more poorly, while the complex binds the ribonucleotide GA about 25 times more poorly. When the ligand is the GA-rich element from the PRM-2 message, or its deoxyribonucleotide variant, we see the same pattern between translin and the complex, albeit with less dramatic differences. This pattern of RNA and DNA preference between the two protein complexes is consistent with more qualitative work by others; Hecht and coworkers used gel shift assays to show that trax decreases translin's affinity for a specific RNA sequence but increases it's affinity for specific a DNA sequence [52].

Trax being able to switch translin's binding preference between DNA and RNA may be important in understanding the physiological role of these two proteins. Perhaps the significance of these observations is most clearly seen in the binding of the natural protamine mRNA sequence, PRM-2; this sequence has been identified as crucial to the recognition of mRNA functioning in sperm development (Kwon and Hecht 1991). We see that the mRNA motif binds at least 100 times more tightly to translin than to the translin•trax complex. To reiterate, it is known that trax has a nuclear localization signal (NLS) [50], while translin has a nuclear export signal (NES) [52]. At the simplest level one might imagine the translin•trax complex being taken into the nucleus using the trax NLS. The complex would favor DNA binding in the nucleus. However, once translin is released from trax it favors RNA binding, and can recognize certain mRNAs, like PRM2, and carry them into the cytoplasm using its NES.

Due to a lack of detailed structural data, the specifics of the translin●oligonucleotide and translin●trax●oligonucleotide interactions are not known. It appears that the biologically relevant form of translin is a cyclic octamer which binds both RNA and DNA in the center [47]. The gel filtration data of the complex suggests it is also an octamer, but the organization of the different subunits is ambiguous. Therefore, we do not know if translin has active site binding pockets that may preferentially bind guanine compared to other bases. It is clear from these results that G-rich nucleotides are bound strongly by translin, but it is not known whether or not this is a result of these protein complexes assembling in such a way as to create guanine binding pockets or the result of a tertiary conformation of the G-rich nucleotide being preferentially recognized. Additionally, how the interaction of trax, which appears to lack nucleic acid binding capacities, switches translin's affinity from RNA to DNA also is not clear. DNA bases have subtly different chemical properties from their RNA counterparts, not the least of which is the lack of a 2' hydroxyl, but they also have more prominent structural differences. Presumable the switch in specificity arises from a structural change that shifts from reading A form RNA to B form DNA. Furthermore, it was observed that translin's physiological target, PRM-2, contained four GAG sequences. Assuming that translin assembles and exists as an octameric disk, one would expect the octamer to have eight binding sites, and a polymer with the correct eight fold repeat might bind very tightly. However, as shown in Table 8.1, translin bound $(GAG)_8$ more weakly than the PRM-2 sequence, and binds only 1/20th as well as $(GA)_{12}$. This suggests that the binding of RNA to translin is more complex than simply reading base sequences by eight symmetrically related active sites. As previously stated, we do not know the structure of the translin•trax complex, but the simplest model would be a hetero-octameric disc with four translin•trax pairs, and four translin active sites at 90° intervals. It is interesting to note that both the $d(GA)_{12}$ and $d(GAG)_8$ oligonucleotides have four evenly spaced GAG sequences and they both bind to the complex with sub-micromolar affinities. This result may be indicative of the complex, in contrast to translin, reading the bases directly.

To further investigate the roles of GAG trimers in ligand recognition by translin, two GAG trimers at positions 11-13 and 29-31 were separately and jointly mutated to CAC, and their binding affinities measured (Table 8.2). The mutations in the first PRM-2 variant sequence yielded a slight, but reproducible, reduction in translin's affinity for PRM-2 (K_d 1 μM and K_d 0.2 μM respectively). However, the mutations of the other two variant sequences did not perturb binding. This is somewhat difficult to rationalize since the double mutant includes the 11-13 mutation which does perturb binding. One possible explanation for this effect can be seen by examining Figure 4.1, which shows the predicted secondary structure of the PRM-2 variants [56]. The PRM-2 sequence and the tighter binding variants all exhibit a stem loop structure with two unpaired A bases in the stem. The weaker binding variant 1 is predicted to have a distinct secondary structure that lacks this feature. The experimental data combined with this secondary structure prediction suggests that translin may recognize secondary structural element in the RNA that presents the bases in the correct orientation for optimum protein-RNA interaction. To extend this study slightly, we measured the binding affinity of translin to a truncated 30-mer PRM-2 (PRM-$2_{(1-30)}$) ligand; it contains only the putative stem loop structure of the bases 1 – 30, and lacks the last nine 3' bases (Figure 9.1). Translin bound to this shortened ligand with a K_d of 0.2 μM, essentially the same as that determined for PRM-2.

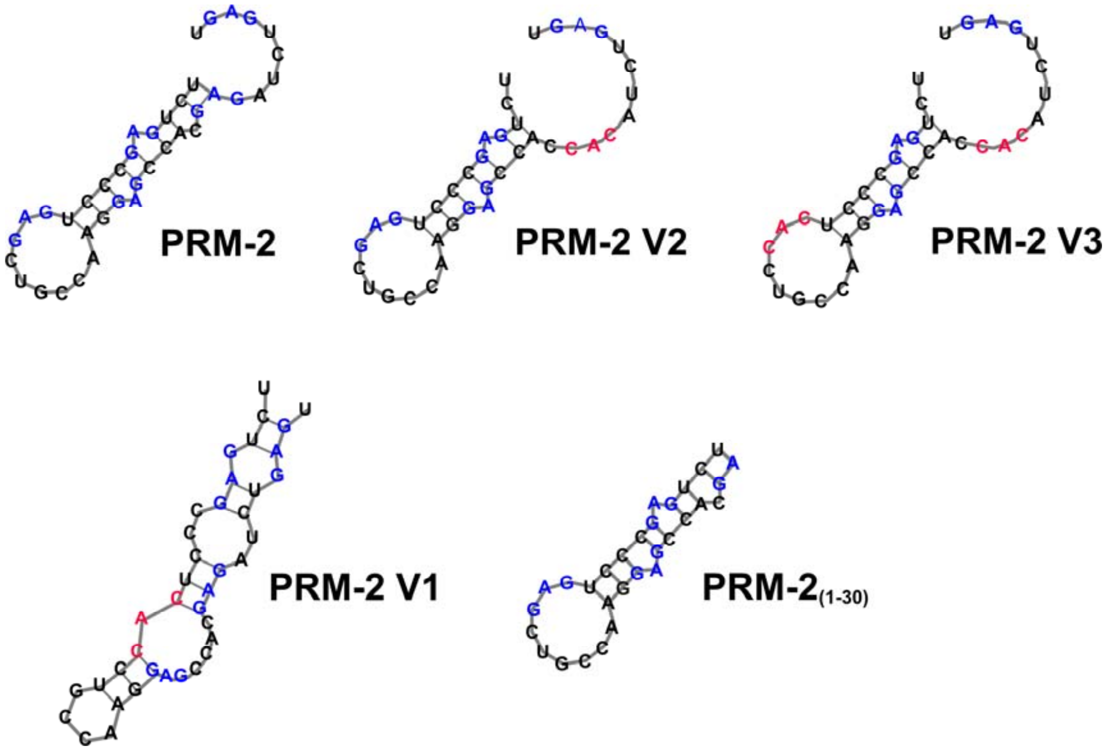

Figure 9.1: Secondary structures of RNA ligands derived from PRM-2. The predicted secondary structures for PRM-2 and the four PRM-2 variant sequences as determined using the Vienna RNA web server [56].

These results are consistent with the hypothesis that the protein's endogenous target may be a secondary structure in the 3' UTR of the mRNA. Extensive structural research shows that DNA sequences containing G-tracts as short as G_2 can fold into distinct secondary structures [57]. This fact adds to the difficulties of interpreting this binding data in a completely straightforward and consistent fashion. It may be, for example, that in its biological role, translin binds a range of Y and H element containing RNAs with a K_d in the low micromolar range (Table 8.1). Each may form a secondary structure that binds in the central cavity of the octameric disk and makes some specific contacts. The unusually tight binding of rGA may arise adventitiously because it assumes, by chance, the best fold to maximize binding interactions.

In discussing the roles for translin and the complex with trax it is important to note that trax has also been shown to interact with the versatile nuclear protein C1D [55]. C1D interacts with trax as part of a cellular DNA repair response. Furthermore, the trax●C1D and translin●trax interactions are mutually exclusive, and consequentially, the interaction between trax and C1D may regulate the formation of translin●trax complexes. For example, the trax●C1D interaction may prevent translin or translin●trax from participating in recombination events before DNA repair mechanisms are complete [55]. Trax's ability to change protein partners between translin and C1D could act i*n vivo* to switch translin from a DNA-binding protein to an RNA-binding protein. This is generally consistent with, the model proposed by Hecht and coworkers that trax can regulate translin's subcellular locale as shown in Figure 9.2 [54]. It has previously been demonstrated that both trax and translin co-localize to the nucleus in meiotic pachytene spermatocytes and co-localize to the cytoplasm in post meiotic spermatids [54]. Once in the nucleus, this complex can interact with DNA, presumably functioning in DNA crossing over which occurs at this stage. Thereafter, trax dissociates, exchanging translin for C1D, and freeing translin to interact with mRNAs marked for export from the nucleus via translin's NES [54, 55]. Once translin has re-entered the cytoplasm, it can remain bound to the mRNA until a cellular signal for release and subsequent translation of the message has been received [54]. This transport has been observed in nerve cells and in developing spermatids [41, 44-46, 58-63]. The ability to act as a shuttling protein that transitorily localizes to the nucleus is a hallmark of the RNA-binding proteins that traffic mRNAs in neuronal cells [36]. This notion is strengthened by the key observation that once localized to the nucleus translin binds an mRNA cargo, which is also characteristic of RNA trafficking in neurons [36].

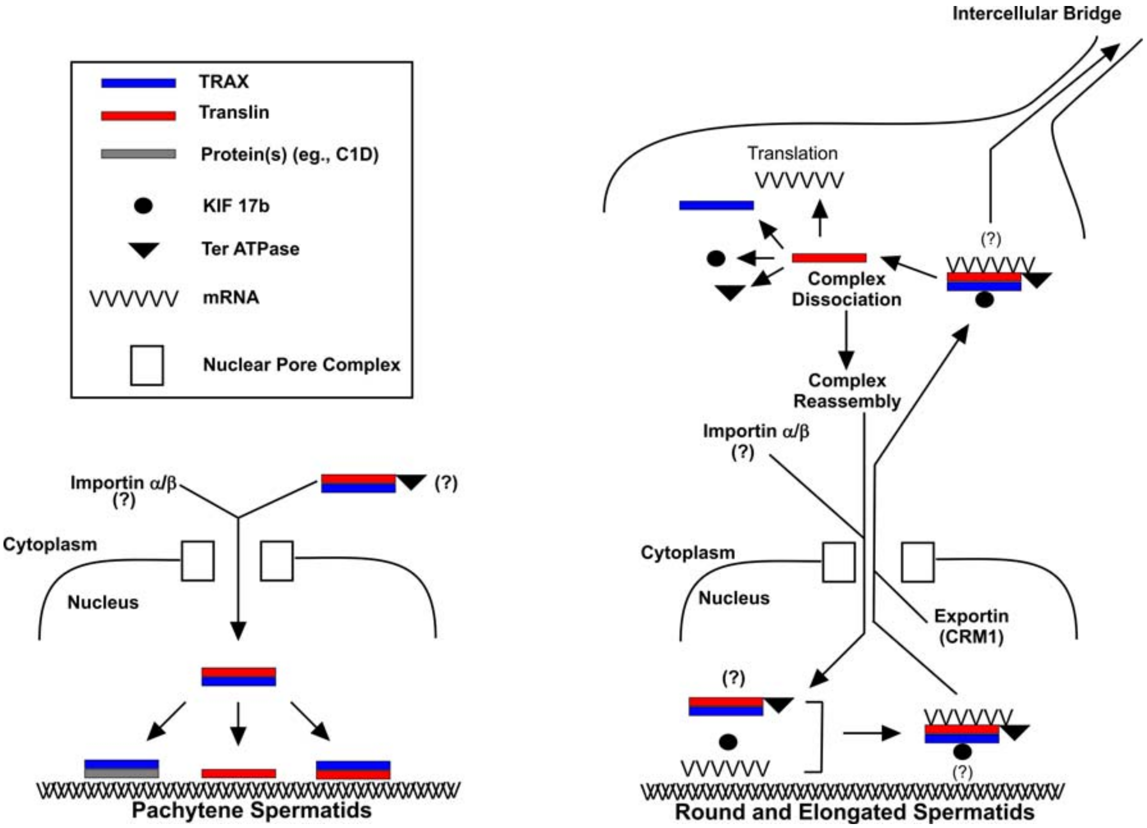

Figure 9.2: Nucleocytoplasmic shuttling by the translin●trax complex. This model was proposed by Hecht and coworkers [54]. In pachytene spermatocytes, when exchange of genetic information can occur, the trax/translin ratio is elevated allowing for trax to associate with translin, and most likely other proteins like Ter ATPase. Once this complex has formed it can gain entry into the nucleus using trax's NLS. Once in the nucleus translin alone, or complexed with trax or other partner proteins like C1D can interact with DNA or RNA. In round and elongated spermatids, translin containing complexes are predominantly found in the cytoplasm and contain the partner proteins Ter ATPase and KIF17. These complexes have been observed to shuttle mRNA through intercellular bridges.

Chapter 10: Conclusion

In this study, a comparative oligonucleotide binding experiments between translin and translin●trax were carried out. From the data collected, it can be concluded that translin functions primarily as an RNA binding protein that favors G-rich sequences and seems to target a secondary structure in the RNA as opposed to a liner sequence of bases. To the contrary, translin●trax binds almost exclusively to G-rich DNA sequences. It can be concluded that trax's interaction with translin acts to decrease translin's affinity for RNA and decrease its affinity for DNA; in other words converting translin from an RNA binding protein to a DNA binding protein. This property of trax may indicate that it functions in the cell as a regulatory factor for translin during mRNA trafficking since trax can change translin's subcellular locale in addition to its oligonucleotide binding activities.

Chapter 11: Future Work

Future work should focus on alternative approaches to structural studies of translin and trax. Specifically, since trax could not be successfully cleaved from DsbA, further attempts to crystallize this fusion protein would be worthwhile since structural data on trax in any form may provide new information into how it functions. Additionally, high throughput oligonucleotide experiments using both translin and translin●trax as targets could prove useful to further clarify what these protein complexes target.

Bibliography

1 Hanafy, K. A., Krumenacker, J. S. and Murad, F. (2001) NO, nitrotyrosine, and cyclic GMP in signal transduction. Med Sci Monit **7**, 801-819

2 Murad, F. (1998) Nitric oxide signaling: would you believe that a simple free radical could be a second messenger, autacoid, paracrine substance, neurotransmitter, and hormone? Recent Prog Horm Res **53**, 43-59; discussion 59-60

3 Voet, D. and Voet, J. (2004) Biochemistry

4 Alderton, W. K., Cooper, C. E. and Knowles, R. G. (2001) Nitric oxide synthases: structure, function and inhibition. Biochem J **357**, 593-615

5 Vallance, P. and Leiper, J. (2002) Blocking NO synthesis: how, where and why? Nat Rev Drug Discov **1**, 939-950

6 Klahr, S. (2001) The role of nitric oxide in hypertension and renal disease progression. Nephrol Dial Transplant **16 Suppl 1**, 60-62

7 Ohshima, H., Tatemichi, M. and Sawa, T. (2003) Chemical basis of inflammation-induced carcinogenesis. Arch Biochem Biophys **417**, 3-11

8 Xu, W., Liu, L. Z., Loizidou, M., Ahmed, M. and Charles, I. G. (2002) The role of nitric oxide in cancer. Cell Res **12**, 311-320

9 Wink, D. A. and Mitchell, J. B. (2003) Nitric oxide and cancer: an introduction. Free Radic Biol Med **34**, 951-954

10 Jenkins, D. C., Charles, I. G., Thomsen, L. L., Moss, D. W., Holmes, L. S., Baylis, S. A., Rhodes, P., Westmore, K., Emson, P. C. and Moncada, S. (1995) Roles of nitric oxide in tumor growth. Proc Natl Acad Sci U S A **92**, 4392-4396

11 Thomsen, L. L. and Miles, D. W. (1998) Role of nitric oxide in tumour progression: lessons from human tumours. Cancer Metastasis Rev **17**, 107-118

12 Moncada, S. and Erusalimsky, J. D. (2002) Does nitric oxide modulate mitochondrial energy generation and apoptosis? Nat Rev Mol Cell Biol **3**, 214-220

13 Huang, P. L. (2000) Mouse models of nitric oxide synthase deficiency. J Am Soc Nephrol **11 Suppl 16**, S120-123

14 Dawson, V. L. and Dawson, T. M. (1998) Nitric oxide in neurodegeneration. Prog Brain Res **118**, 215-229

15 Leiper, J. and Vallance, P. (1999) Biological significance of endogenous methylarginines that inhibit nitric oxide synthases. Cardiovasc Res **43**, 542-548

16 Boger, R. H. and Bode-Boger, S. M. (1997) [Endothelial dysfunction in peripheral arterial occlusive disease: from basic research to clinical use]. Vasa **26**, 180-184

17 Boger, R. H., Bode-Boger, S. M., Szuba, A., Tsao, P. S., Chan, J. R., Tangphao, O., Blaschke, T. F. and Cooke, J. P. (1998) Asymmetric dimethylarginine (ADMA): a novel risk factor for endothelial dysfunction: its role in hypercholesterolemia. Circulation **98**, 1842-1847

18 Palm, F., Onozato, M. L., Luo, Z. and Wilcox, C. S. (2007) Dimethylarginine dimethylaminohydrolase (DDAH): expression, regulation, and function in the

cardiovascular and renal systems. Am J Physiol Heart Circ Physiol **293**, H3227-3245

19 Wilcken, D. E., Sim, A. S., Wang, J. and Wang, X. L. (2007) Asymmetric dimethylarginine (ADMA) in vascular, renal and hepatic disease and the regulatory role of L-arginine on its metabolism. Mol Genet Metab **91**, 309-317; discussion 308

20 Tran, C. T., Leiper, J. M. and Vallance, P. (2003) The DDAH/ADMA/NOS pathway. Atheroscler Suppl **4**, 33-40

21 MacAllister, R. J., Parry, H., Kimoto, M., Ogawa, T., Russell, R. J., Hodson, H., Whitley, G. S. and Vallance, P. (1996) Regulation of nitric oxide synthesis by dimethylarginine dimethylaminohydrolase. Br J Pharmacol **119**, 1533-1540

22 Frey, D., Braun, O., Briand, C., Vasak, M. and Grutter, M. G. (2006) Structure of the mammalian NOS regulator dimethylarginine dimethylaminohydrolase: A basis for the design of specific inhibitors. Structure **14**, 901-911

23 Leiper, J. M., Santa Maria, J., Chubb, A., MacAllister, R. J., Charles, I. G., Whitley, G. S. and Vallance, P. (1999) Identification of two human dimethylarginine dimethylaminohydrolases with distinct tissue distributions and homology with microbial arginine deiminases. Biochem J **343 Pt 1**, 209-214

24 Santa Maria, J., Vallance, P., Charles, I. G. and Leiper, J. M. (1999) Identification of microbial dimethylarginine dimethylaminohydrolase enzymes. Mol Microbiol **33**, 1278-1279

25 Stone, E. M. (2006) The Catalytic Mechanism of Dimethylarginine Diemthylaminohydrolase (DDAH) from *Pseudomonas aeruginosa*.

26 Murray-Rust, J., Leiper, J., McAlister, M., Phelan, J., Tilley, S., Santa Maria, J., Vallance, P. and McDonald, N. (2001) Structural insights into the hydrolysis of cellular nitric oxide synthase inhibitors by dimethylarginine dimethylaminohydrolase. Nat Struct Biol **8**, 679-683

27 Wang, Y., Monzingo, A. F., Hu, S., Schaller, T. H., Robertus, J. D. and Fast, W. (2009) Developing dual and specific inhibitors of dimethylarginine dimethylaminohydrolase-1 and nitric oxide synthase: toward a targeted polypharmacology to control nitric oxide. Biochemistry **48**, 8624-8635

28 Leiper, J., Nandi, M., Torondel, B., Murray-Rust, J., Malaki, M., O'Hara, B., Rossiter, S., Anthony, S., Madhani, M., Selwood, D., Smith, C., Wojciak-Stothard, B., Rudiger, A., Stidwill, R., McDonald, N. Q. and Vallance, P. (2007) Disruption of methylarginine metabolism impairs vascular homeostasis. Nat Med **13**, 198-203

29 Stone, E. M., Person, M. D., Costello, N. J. and Fast, W. (2005) Characterization of a transient covalent adduct formed during dimethylarginine dimethylaminohydrolase catalysis. Biochemistry **44**, 7069-7078

30 Stone, E. M., Costello, A. L., Tierney, D. L. and Fast, W. (2006) Substrate-assisted cysteine deprotonation in the mechanism of dimethylargininase (DDAH) from Pseudomonas aeruginosa. Biochemistry **45**, 5618-5630

31 Leiper, J., Murray-Rust, J., McDonald, N. and Vallance, P. (2002) S-nitrosylation of dimethylarginine dimethylaminohydrolase regulates enzyme activity: further interactions between nitric oxide synthase and dimethylarginine dimethylaminohydrolase. Proc Natl Acad Sci U S A **99**, 13527-13532

32 Otwinowski, W. M. a. Z. (1997) Processing of X-ray Diffraction Data Collected in Oscillation Mode. Methods in Enzymology **276**, 307-326

33 Emsley, P. and Cowtan, K. (2004) Coot: model-building tools for molecular graphics. Acta Crystallogr D Biol Crystallogr **60**, 2126-2132

34 Schuttelkopf, A. W. and van Aalten, D. M. (2004) PRODRG: a tool for high-throughput crystallography of protein-ligand complexes. Acta Crystallogr D Biol Crystallogr **60**, 1355-1363

35 Adams, P. D., Grosse-Kunstleve, R. W., Hung, L. W., Ioerger, T. R., McCoy, A. J., Moriarty, N. W., Read, R. J., Sacchettini, J. C., Sauter, N. K. and Terwilliger, T. C. (2002) PHENIX: building new software for automated crystallographic structure determination. Acta Crystallogr D Biol Crystallogr **58**, 1948-1954

36 Besse, F. and Ephrussi, A. (2008) Translational control of localized mRNAs: restricting protein synthesis in space and time. Nat Rev Mol Cell Biol **9**, 971-980

37 Martin, K. C. and Ephrussi, A. (2009) mRNA localization: gene expression in the spatial dimension. Cell **136**, 719-730

38 Hecht, N. B. (1998) Molecular mechanisms of male germ cell differentiation. Bioessays **20**, 555-561

39 Aoki, K., Suzuki, K., Sugano, T., Tasaka, T., Nakahara, K., Kuge, O., Omori, A. and Kasai, M. (1995) A novel gene, Translin, encodes a recombination hotspot binding protein associated with chromosomal translocations. Nat Genet **10**, 167-174

40 Wu, X. Q., Gu, W., Meng, X. and Hecht, N. B. (1997) The RNA-binding protein, TB-RBP, is the mouse homologue of translin, a recombination protein associated with chromosomal translocations. In Proc Natl Acad Sci U S A, pp. 5640-5645

41 Han, J. R., Gu, W. and Hecht, N. B. (1995) Testis-brain RNA-binding protein, a testicular translational regulatory RNA-binding protein, is present in the brain and binds to the 3' untranslated regions of transported brain mRNAs. Biol Reprod **53**, 707-717

42 Li, Z. and Baraban, J. M. (2004) High affinity binding of the Translin/Trax complex to RNA does not require the presence of Y or H elements. Brain Res Mol Brain Res **120**, 123-129

43 Jacob, E., Pucshansky, L., Zeruya, E., Baran, N. and Manor, H. (2004) The human protein translin specifically binds single-stranded microsatellite repeats, d(GT)n, and G-strand telomeric repeats, d(TTAGGG)n: a study of the binding parameters. J Mol Biol **344**, 939-950

44 Wu, X. Q., Lefrancois, S., Morales, C. R. and Hecht, N. B. (1999) Protein-protein interactions between the testis brain RNA-binding protein and the transitional endoplasmic reticulum ATPase, a cytoskeletal gamma actin and Trax in male germ cells and the brain. Biochemistry **38**, 11261-11270

45 Chennathukuzhi, V., Morales, C. R., El-Alfy, M. and Hecht, N. B. (2003) The kinesin KIF17b and RNA-binding protein TB-RBP transport specific cAMP-responsive element modulator-regulated mRNAs in male germ cells. Proc Natl Acad Sci U S A **100**, 15566-15571

46 Li, Z., Wu, Y. and Baraban, J. M. (2008) The Translin/Trax RNA binding complex: Clues to function in the nervous system. Biochim Biophys Acta

47 VanLoock, M. S., Yu, X., Kasai, M. and Egelman, E. H. (2001) Electron microscopic studies of the translin octameric ring. J Struct Biol **135**, 58-66

48 Pascal, J. M., Hart, P. J., Hecht, N. B. and Robertus, J. D. (2002) Crystal structure of TB-RBP, a novel RNA-binding and regulating protein. J Mol Biol **319**, 1049-1057

49 Wu, X. Q., Xu, L. and Hecht, N. B. (1998) Dimerization of the testis brain RNA-binding protein (translin) is mediated through its C-terminus and is required for DNA- and RNA-binding. Nucleic Acids Res **26**, 1675-1680

50 Aoki, K., Ishida, R. and Kasai, M. (1997) Isolation and characterization of a cDNA encoding a Translin-like protein, TRAX. FEBS Lett **401**, 109-112

51 Finkenstadt, P. M., Kang, W. S., Jeon, M., Taira, E., Tang, W. and Baraban, J. M. (2000) Somatodendritic localization of Translin, a component of the Translin/Trax RNA binding complex. J Neurochem **75**, 1754-1762

52 Chennathukuzhi, V. M., Kurihara, Y., Bray, J. D. and Hecht, N. B. (2001) Trax (translin-associated factor X), a primarily cytoplasmic protein, inhibits the binding of TB-RBP (translin) to RNA. J Biol Chem **276**, 13256-13263

53 Yang, S., Cho, Y. S., Chennathukuzhi, V. M., Underkoffler, L. A., Loomes, K. and Hecht, N. B. (2004) Translin-associated factor X is post-transcriptionally regulated by its partner protein TB-RBP, and both are essential for normal cell proliferation. J Biol Chem **279**, 12605-12614

54 Cho, Y. S., Chennathukuzhi, V. M., Handel, M. A., Eppig, J. and Hecht, N. B. (2004) The relative levels of translin-associated factor X (TRAX) and testis brain RNA-binding protein determine their nucleocytoplasmic distribution in male germ cells. J Biol Chem **279**, 31514-31523

55 Erdemir, T., Bilican, B., Oncel, D., Goding, C. R. and Yavuzer, U. (2002) DNA damage-dependent interaction of the nuclear matrix protein C1D with Translin-associated factor X (TRAX). J Cell Sci **115**, 207-216

56 Gruber, A. R., Lorenz, R., Bernhart, S. H., Neubock, R. and Hofacker, I. L. (2008) The Vienna RNA websuite. Nucleic Acids Res **36**, W70-74

57 Keniry, M. A. (2001) Quadruplex Structures in Nucleic Acids. Biopolymers **56**, 123-146

58 Wu, X. Q. and Hecht, N. B. (2000) Mouse testis brain ribonucleic acid-binding protein/translin colocalizes with microtubules and is immunoprecipitated with messenger ribonucleic acids encoding myelin basic protein, alpha calmodulin kinase II, and protamines 1 and 2. Biol Reprod **62**, 720-725

59 Kobayashi, S., Takashima, A. and Anzai, K. (1998) The dendritic translocation of translin protein in the form of BC1 RNA protein particles in developing rat hippocampal neurons in primary culture. Biochem Biophys Res Commun **253**, 448-453

60 Han, J. R., Yiu, G. K. and Hecht, N. B. (1995) Testis/brain RNA-binding protein attaches translationally repressed and transported mRNAs to microtubules. Proc Natl Acad Sci U S A **92**, 9550-9554

61 Hecht, N. B. (2000) Intracellular and intercellular transport of many germ cell mRNAs is mediated by the DNA- and RNA-binding protein, testis-brain-RNA-binding protein (TB-RBP). Mol Reprod Dev **56**, 252-253

62 Morales, C. R., Lefrancois, S., Chennathukuzhi, V., El-Alfy, M., Wu, X., Yang, J., Gerton, G. L. and Hecht, N. B. (2002) A TB-RBP and Ter ATPase complex accompanies specific mRNAs from nuclei through the nuclear pores and into intercellular bridges in mouse male germ cells. Dev Biol **246**, 480-494

63 Schroer, U., Volk, G. F., Liedtke, T. and Thanos, S. (2007) Translin-associated factor-X (Trax) is a molecular switch of growth-associated protein (GAP)-43 that controls axonal regeneration. Eur J Neurosci **26**, 2169-2178

Vita

Matthew Wayne Lluis was born in Tampa, FL on July 23rd, 1981 to Robert and Sylvia Lluis. He grew up in Tampa, FL and graduated from Chamberlain High School in 1999. Matthew attended the University of South Florida from August 1999 until graduating Summa Cum Laude with his Bachelor of Sciences degree in Chemistry in May 2004. While attending USF he was the recipient of the Department of Chemistry's Analytical Chemistry Award and was recognized as the most outstanding chemistry major for the year 2004. He then attended the University of Texas at Austin for his graduate studies in Dr. Jon Robertus' lab. The work presented here is being prepared for publication.

Matthew Lluis, Warren Hoe, Jennifer Schleit, and Jon Robertus. (2009) "Analysis of Nucleic Acid Binding by a Recombinant Translin-Trax Complex" (in preparation).

Permanent address: 12010 Nicklaus Circle, Tampa, FL, 33624

This dissertation was typed by Matthew Wayne Lluis.